Fakultät für Physik des Instituts
für Theorie der Kondensierten Materie

Impurity Controlled Antiferromagnetic Quantum Criticality in Heavy Fermion Systems

Zur Erlangung des akademischen Grades eines

DOKTORS DER NATURWISSENSCHAFTEN

genehmigte

DISSERTATION

von

M.Sc. Meng-Chieh Ling
aus Taiwan

Tag der mündlichen Prüfung: 21. Oktober 2016
Referent: Prof. Dr. Jörg Schmalian
Korreferent: Prof. Dr. Alexander Shnirman

to Li-Ru Hong, Miruku, and Nori

Acknowledgments

First, I would to thank Professor Jörg Schmalian for initiating this research project and his great patience for supervising this PhD thesis. Without his attention to detail, extensive knowledge, and insight in the world of condensed matter this thesis cannot achieve this level of completeness. I also would like to express my appreciation that Professor Alexander Schnirman agrees to be my second instructor.

When it comes to the key part of my numerical simulation NRG, I am grateful that Theo Costi from Forschungszentrum Jülich taught me everything about numerical renormalization group such that I could have a deep understanding in its details. I also want to express my gratitude to Rok Žitko from the University of Ljubljana f for providing the well programmed Ljubljana NRG and his patience in guiding me how to use it properly. Also thanks Christian Seiler and Andreas Poenicke for helping me solve all the computer related issues such that the numerical simulation can be carried out smoothly.

I also want to show my appreciation to my colleages who proof read this thesis: Bhilahari Jeevanesan, Mareike Hoyer, Mathias Bard, Mathias Scheurer, Nikolaos Kainaris, and Patrik Hlobil.

As a foreigner who come to a country full of bureaucracy and with fierce competition for the rental market, it is impossible survive without the help from my colleagues Paul Baireuther, Peter Orth, and institute secretary Rose Schrempp. Also thanks the current institute secretary Fabienne Flatter for providing all kinds of assistance.

I have to thank my wife Li-Ru Hong for her patience, tolerance, and perseverance. Also thanks her for betting her the best part of her life on me and staying with me when the progress did not go well. I may not be able to survive without her.

Contents

List of Figures

Chapter 1

Introduction

Quantum criticality in metallic system is a major open problem in condensed matter physics due to the interplay between critical excitations and the Landau Fermi liquid. In the vicinity of the quantum critical point, strong low energy excitations such as magnons may modifiy the Landau Fermi liquid behavior and lead to non-Fermi liquid phenomena. In addition, the phase diagrams of high temperature superconductors such as cuprates suggest the existence of a quantum critical point in the superconductiviting dome and that superconductivity is associated with the non-Fermi liquid and critical fluctuations of the Fermi surface [19, 20]. Therefore, a better understanding of quantum criticality helps the understanding of strongly correlated itinerant systems. Futhermore, spatial fluctuations and temporal fluctuations are coupled together close to a quantum critical point leading to a temporal dimension with dimensionality z. The values of this dynamical scaling exponent z are well understood in the spin density wave picture in which the quantum critical points reside within the Fermi energy scales [21–23]. However, many experimental systems seem to display values of z significantly different from this "standard model" of metallic quantum criticality.

Among all metallic systems with quantum criticality, metallic heavy fermion magnets serve as typical playgrounds for investigating quantum phase transitions. Because of the small Fermi energy scales, magnetism can arise at small energy scales. This gives the heavy fermion systems an advantage in studying quantum criticality: a quantum phase transition can be achieved by tuning a magnetic field, applying pressure, or replacing chemical elements to suppress the magnetic phase transition temperatures. Conventionally, quantum criticality under the Landau framework is determined by the symmetry and dimensionality of order parameter fluctuations. However, in heavy fermion systems, both the Fermi energy scale and the phase transition temperature can vanish at the quantum critical points. This can be interpreted as heavy fermion quasiparticles dissociating due to the critical magnetic fluctuations. In this case, it is suggested that $z = 4$ in the heavy fermion antiferromagnetic system YRh_2Si_2 by applying scaling analysis and the phenomenological critical antiferromagnetic spin susceptibility [24]. This value is twice the size of its counterpart in spin density wave scenario. Other theoretical and experimental works [18, 25–27] also suggest that the universality classes of the quantum critical points with and without Kondo destruction are different. Therefore, the Landau framework can be extended by taking critical fluctuations close to the quantum critical points into consideration. Another interesting question is about the duality of $f-$electrons. In the heavy fermion systems f-electrons can show either itinerant wave-like or localized particle-like characters. The deep lying f-electrons may melt into the conduction band via Kondo coupling and enlarge the size of the Fermi surface. In experiment

this crossover can be detected by measuring the size of the Fermi surface via the de Haas - van Alphan (dHvA) effect, but understanding the mechanism behind the crossover of the f-electrons from the localized state to the itinerant state remains challenging [28, 29]. Although in the heavy fermion lattices the heaviness of fermionic quasiparticle is interpreted as a result of the coherent spin-flip process, explicit evidence cannot be found.

In a recent experiemental investigation on the metallic heavy fermion antiferromagnetic system $CeCu_2Ge_2$ [1], it was shown that quantum phase transition can be achieved by substituting magnetic Ce^{3+} with non-magnetic La^{3+}. From Fig.(1.1), it can be seen that both magnetism and lattice coherence in this heavy fermion system are robust against impurity concentration. Moreover, despite various efforts having been put into the investigations of the antiferromagnetic heavy fermion quantum critical point, systematically studying of metallic heavy fermion antiferromagnet with respect to impurity concentration from the side of theory is still lacking. This interesting behavior combined with our ambition to fill the gap triggered our systematic study of metallic heavy fermion antiferromagnets with non-magnetic impurity doping.

In this thesis, we numerically investigate a model system that captures the major aspects of the diluted system $Ce_{1-x}La_xCu_2Ge_2$ such as the robust lattice coherence and long range magnetic ordering. The crossovers between the lattice coherent - incoherent states and the f-electron itinerant - localized states are also studied in detail as functions of temperature and impurity concentration. We also show that the coupling between the f-electrons and the c-electrons are responsible for *both* the heavy fermion Kondo physics and the antiferromagnetism. In addition, we thoroughly analyze the quantum critical point by the scaling law to obtain critical exponents which uniquely determine the class of the quantum phase transition. Susceptibilities subjected to a uniform magnetic field and staggered magnetic field are also calculated as a function of temperature in the vicinity of quantum critical point. The obtained critical exponents are in good agreement with those obtained theoretically or experimentially from the local quantum critical point systems.

This thesis is organized as following: In chapter 1 we give brief reviews on Kondo physics, quantum criticality, the Anderson lattice model, dynamical mean field theory, the coherent potential approximation, and how to experimentally arrive quantum critical point.

In chapter 2 we discuss why the Anderson lattice model is chosen to investigate the heavy fermion system $Ce_{1-x}La_xCu_2Ge_2$. Green's functions of the periodic Anderson model and the dilute limit will also be given. We will also show how to extend the paramagnetic state Green's function to commensurate antiferromagnetic state Green's function on a bipartite lattice.

In chapter 3 details of dynamical mean field theory and numerical renormalization group will be discussed and we will show how to use them to construct a self-consistent algorithm. It can be shown that dynamical mean field theory in dilute systems recovers both cases of periodic Anderson lattice and dilute limit.

In chapter 4 we will show that from temperature and impurity concentration dependent resistivity and magnetization, a phase diagram whose behavior is similar to that of $Ce_{1-x}La_xCu_2Ge_2$ can be obtained from the Anderson lattice model and dynamical mean field theory. It can be seen that the onset of lattice coherence does not change by including antiferromagnetism. However, low temperature resistivity may decrease by two order of magnitude due to suppressed spin disorder scattering.

In chapter 5 we systematically investigate the imaginary part of the averaged self-energy, it can be seen that besides electron-electron scattering, impurity-electron scattering is also reduced in the antiferromagnetic state. The crossover between lattice coherent - incoherent states can be observed by investigating the f-electron dispersion relation in detail. By analyzing both f-electron and c-electron spectral functions, we suggests that in the antiferromagnetic state, the f-electron local state and

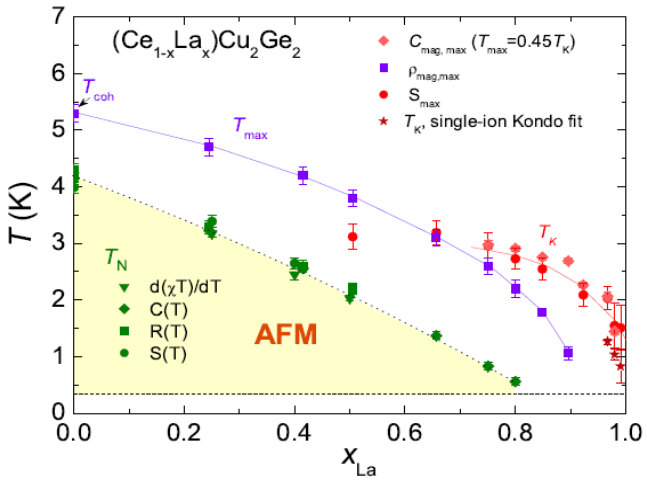

Figure 1.1: *Phase diagram of $Ce_{1-x}La_xCu_2Ge_2$ as a function of temperature and La impurity concentration x [1]. Substituting Ce by La removes f-electrons which play the role of local magnetic moment. An AFM phase exists up to $x = 0.8$ and lattice coherence persists up to $x = 0.9$. The robustness of long range magnetic ordering and lattice coherence against impurity concentration triggered this numerical study.*

the c-electron conduction band state are coupled ferromagnetically. We will show that by using the modified Drude model and optical conductivity measurements, it is possible to identify the f-electron itinerant-localization crossover. However, dynamical Kondo coupling between f-electron local state and c-electron conduction band state gives rise to strong mass renormalizations. The heaviness of fermion as a result of temporal coherent spin-flip process will also be shown explicitly.

In chapter 6 we calculate magnetization as a function of impurity concentration at zero temperature to obtain the critical concentration x_c and the corresponding critical exponent β. By calculating susceptibility as a function of magnetic field we will show critical exponent δ. Then universal functions of both staggered susceptibility and uniform susceptibility at critical concentration will be identified by data collapse. Under uniform magnetic field, susceptibility at high temperature shows T/B scaling. The obtained critical exponents δ, β, and $z\nu$ as well as T/B scaling suggest that the obtained quantum critical point is a local quantum critical point.

1.1 Kondo Physics

Since this thesis is inspired by the experimental result of antiferromagnetic (AFM) heavy fermion compound $Ce_{1-x}La_xCu_2Ge_2$ [1], we discuss in this section what a heavy fermion system is and its importance to understad strongly correlated systems. Before introducing heavy fermion systems, we should introduce the basic concept of single ion Kondo physics.

1.1.1 Single ion Kondo Physics

Kondo physics was discovered in 1934 when anomalous behavior was observed in the resistivity measurement of high purity gold: by decreasing the temperature, the resistivity developed a local minimum and increased again upon approaching the characteristic Kondo temperature T_K [30]. This observation was in contrast to the low temperature resistivity model at that time:

$$R = R_0 + AT^2 + BT^5, \tag{1.1}$$

where R_0 is the residue resistivity due to impurity, the second term due to electron-electron scattering, and the last term ascribed to the electron-phonon interaction. Later, Kondo successfully explained the minimum in resistivity by proposing a model in which conduction electrons exchange spins with magnetic impurities [31]:

$$H = \sum_{k,\sigma} \epsilon_k n_{k,\sigma} - \sum_{k,k'} J_{kk'} \left(\Psi_k^\dagger \boldsymbol{\sigma} \Psi_k \right) \cdot \mathbf{S}, \tag{1.2}$$

with annihilation and creation spinor operator defined as

$$\Psi_k = \begin{pmatrix} c_{k,\uparrow} \\ c_{k,\downarrow} \end{pmatrix} \tag{1.3}$$

$$\Psi_k^\dagger = \left(c_{k,\uparrow}^\dagger, c_{k,\downarrow}^\dagger \right). \tag{1.4}$$

Here, $\mathbf{S}$ is the impurity spin and $J_{kk'} > 0$ the exchange coupling. However, in this perturbative calculation, low temperature resistivity diverges due to a $\log T$ dependence. It was pointed out that this problem can be treated perturbatively only above a temperature T_K [32], which is called Kondo temperature or Kondo energy scale. Subsequently, Anderson used poor man scaling to show that Kondo coupling $J_{kk'}$ increases when reducing the energy scale D [33]:

$$\frac{dJ}{d\left(\ln D\right)} = -2\rho_0 J^2. \tag{1.5}$$

This differential equation indicates that no matter how small J is in the beginning, when the energy scale $\ln D$ is sufficiently small, J will be arbitrary large. Therefore, J is not a well-controlled parameter in perturbation theory. Meanwhile, experimentally measured susceptibility due to impurity can be fitted by [34]

$$\chi_{imp}(T) = \chi_{imp}(0) \left(1 - \left(\frac{T}{\theta_\chi} \right)^2 - \left(\frac{T}{\theta_\chi} \right)^4 \right) \tag{1.6}$$

at low temperature with $\theta_\chi = 7.5$ K, which suggests a spin single ground state. Although poor man's scaling and experimental results shown in Eq.(1.6) might lead us to the conclusion that conduction band screens impurity spin via antiferromagnetic coupling, the results from the side of theory are not decisive. Therefore, another theory or method was necessary to solve this strongly correlated problem. In the mean time, Schrieffer and Wolff also showed that via a canonical transformation [35] Anderson impurity model can be mapped onto Kondo model under proper conditions. This will be shown in the next chapter. In 1980, this problem was eventually solved by applying numerical renormalization group

(NRG) theory on single impurity Anderson model [36, 37]. NRG calculation shows that both entropy and susceptibility contributions due to impurity drop to zero, the spin singlet state is the ground state and that resistivity increases due to the presence of an impurity when decreasing the temperature.

1.1.2 Heavy Fermion Systems

Kondo physics not only exist in magnetically dilute systems, but also in lattice systems which are characterized as heavy fermion system. Heavy fermion systems get their name, because specific heat measurements indicate a huge mass for the electronic quasiparticles. Fermi liquid, an adiabatic continuation of Fermi gas by taking electron-electron interaction into account, predicts the specific heat to be proportional to temperature for temperature much smaller than renormalized Fermi energy:

$$C_e = \gamma T. \tag{1.7}$$

For ordinary metals Au and Cu, γ is of the order $1\text{mJ/mole}\cdot\text{K}^2$. While the experimentally measured specific heat constants γ for heavy fermion systems can be as large as $1\text{J/mole}\cdot\text{K}^2$. Since $\gamma \propto m$, it seems as if these fermions have masses a thousand times that of bare the electron mass. Similar to the case of single ion Kondo system, this heavy fermion nature originates from a strong antiferromagnetic coupling ρJ between conduction band carriers and f-shell local spins. At low temperature ρJ might be strong enough, such that the local spins are shielded by conduction band carriers and they together form quasiparticles. Suppose a lattice coherence is developed and momentum is a good quantum number, then this hybridization brings the local nature of spins into conduction band carriers such that their dependence on momentum decreases, therefore when the effective mass m_{ij} is calculated via

$$m_{ij}^{-1} = \frac{1}{\hbar^2}\frac{\partial^2 \epsilon_{\mathbf{k}}}{\partial k_i \partial k_j}, \tag{1.8}$$

a large m_{ij} is obtained. This will be explicitly shown in chapter 4.

As a result of the heavy mass, Fermi energy E_F and associated energy scales are also strongly suppressed. Having small energy Fermi scale has two advantages: 1. it emphasizes the importance of the interaction which is independent of this small energy scale; 2. small energy scales can be easily suppressed by tuning magnetic field, pressure, and chemical composition. These three control parameters will be discussed in the section 1.1.3. By changing the relative strength of different energy scales, phase transition might take place at zero temperature and systems undergo quantum phase transition. If this quantum phase transition is of second order, it is called as quantum critical phase transition at which there is no typical length and time scales.

1.2 Quantum Criticality

Quantum Criticality refers to the behavior in the vicinity of a second order phase transition at zero temperature. The phase transition is referred to a quantum critical point. We will discuss a specific example of how this is achieved in the next section. For now we will give a general physical picture and explain why quantum criticality is an interesting and fundamental phenomenon in condensed matter physics.

A natural question to ask is what specific *quantum* effects are of relevance near a quantum critical point. Finite temperature phase transitions are often characterized by an order parameter that can only be rationalized using quantum mechanics. Examples are superconductivity, superfluidity and magnetism. However, the critical behavior near the transition is entirely classical in nature. The simplest answer is that at zero temperature there are no thermal fluctuations, the only possible source of fluctuation arise from quantum effects, governed by Heisenberg's uncertainty principle:

$$\Delta E \cdot \Delta t \geq \frac{\hbar}{2}. \tag{1.9}$$

The second quantization formalism shows that the ground state at zero temperature can virtually jump to an excited state and jump back. Dynamical processes shape the distribution functions of order parameters. In the ordered state and far away from the quantum critical point, we may consider the distribution function of the order parameter is well behaved and has a finite variance or fluctuation. However, close to the critical point, the fluctuations diverge and this implies a fat tail is developed in the distribution function. The extensive distribution enables the system to find other energetically equally favorable states such that the system developes a quantum disordered state. Quantum disordered states, unlike classical disordered states in which order parameters are destroyed, are superpositions of ordered states but the expectation values of the order parameters are zero.

Near second order phase transitions, the correlation length ξ diverges. In case of a finite temperature transition the typical length scale ξ will therefore be large compared to the thermal de Broglie wave length $\lambda_T \propto T^{-1/z}$, with appropriate dynamical exponent that depends on the system under consideration. A system behaves classically for $\xi \gg \lambda_T$. Then one can ignore quantum fluctuations of the order parameter, even if the microscopic origin of the ordered state requires a quantum mechanical analysis. At a quantum critical point $T_c \to 0$. Now, both ξ and λ_T diverge and one can no longer neglect quantum fluctuations of the order parameter.

Besides making quantum fluctuation important, zero temperature creates a temporal dimension with dimensionality z which is the above mentioned dynamical exponent. To see how this happens, let us remind ourselves what we learned in a solid state physics introductory course. Assuming that we have a one dimensional system whose length is L, then we know that each mode can be labelled by a wave number

$$k_n = \frac{n\pi}{L}. \tag{1.10}$$

In order to have a phase transition we must consider a system in the thermodynamic limit, i.e. take the limit $L \to \infty$. In case of a divergence of the correlation length ξ:

$$\xi \sim \left|T - T_c\right|^{-\nu}, \tag{1.11}$$

the relevant modes are the ones with small k_n. When we take quantum effect into account, we use the partition function in the form of path integral in which temperature gives us a dynamical mode called Matsubara frequency

$$\omega_n = \begin{cases} (2n+1)\pi T & \text{for fermions} \\ 2n\pi T & \text{for bosons} \end{cases}. \tag{1.12}$$

By decreasing T to zero, the interval $\Delta\omega = \left|\omega_{n+1} - \omega_n\right|$ goes to zero. If we follow the thought of classical phase transition in the reverse direction, we may guess that there is a temporal dimension which extend to infinity, such that correlation time may diverge close to quantum critical point. Intersting physics

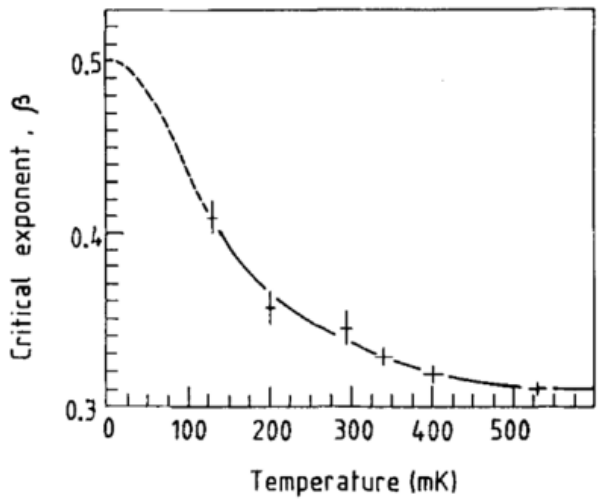

Figure 1.2: *Critical exponent β as a function of temperature of 3D Ising antiferromagnet $MnCl_2 \cdot 4H_2O$. By decreasing temperature, β shifts from 0.3 to 0.5 gradually which indicates a mapping from 3D Ising antiferromagnet to a mean field antiferromagnet [2].*

happens with this extra dimension. For a 1-D transverse field Ising model, it can be mapped onto a 2-D classical ferromagnetic Ising model. The transverse field now plays the role of temperature of the classical problem [38]. Experimentally, the 3D Ising antiferromagnet $MnCl_2 \cdot 4H_2O$ is mapped onto a mean field antiferromagnet at quantum critical point by observing that β shifts from 0.3 to 0.41 (extrapolation to 0.5) shown in Fig.(1.2) [2].

Given the above argumentation one obtains an effective problem with one additional dimension i.e. $d \to d + z$ with $z = 1$. However, as shown in the pioneering works of Hertz, Millis, and Moriya [21–23] on itinerant magnetic system, it turn out that fluctuations in time and space are not symmetric and in general $z \neq 1$. For example, one obtains $z = 2$ for 2D and 3D itinerant antiferromagnets and $z = 3$ for 2D and 3D itinerant ferromagnets. More interestingly, a recent work on itinerat ferromagnet $Sr_{1-x}Ca_xRuO_3$ gives $z = 1.76$ [39] indicating that z does not even have to be an integer.

Since strictly zero temperature is forbidden by the third law of thermodynamics, an interesting question is how quantum criticality can be experimentally observed? Similar to classical phase transition whose critical point controls its vicinity, quantum critical points also control their nearby regions that extends to finite temperature. This behavior is shown in Fig.(1.3), where we show the quantum critical region in which quantum fluctuations are stronger than thermal fluctuations is:

$$\hbar\omega_q > k_B T. \tag{1.13}$$

Here ω_q is a typical excitation frequency of the system.

The competition between various energy scales brings us a rich spectrum of physical phenomena [1, 39–45], such as non-Fermi liquid behavior, unconventional superconductivity, and magnetism. Therefore, studying quantum criticality is one of the few avenues that allow for a quantitative understanding of the world of strongly correlated system. Among such correlated electron systems, i.e. system where the interaction between its fermionic constituents is comparable or larger than their kinetic energy, heavy fermion systems have attracted a lot of attention.

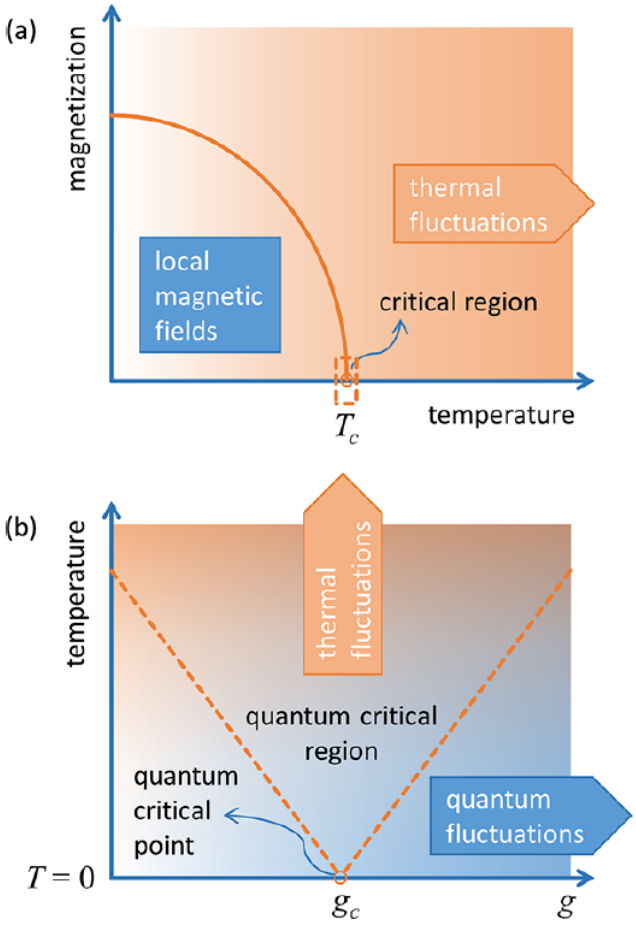

Figure 1.3: *(a) In a classical phase transition, long range magnetic ordering takes place at critical temperature T_c. In the Landau paradigm, fluctuations of order parameter dominate the vicinity of critical temperature and this region is called critical region. (b) Similar idea can be applied on quantum phase transition in which non-thermal control parameter g plays the role of temperature in classical phase transition. Close to the quantum critical point g_c there is also a critical region dominated by fluctuations of order parameter. Since temperature is regarded as an extra dimension in quantum phase transition, quantum critical fluctuations can be observed at finite temperature. Taken from Ref.[3].*

1.3 Disorder induced Quantum Critical Point

In the last section, we mentioned that a quantum critical point occurs at zero temperature and that the fluctuations originating from it are rooted in the quantum dynamics of the involved degrees of freedom. Experimentally, there are three popular control parameters to induced quantum criticality: an external magnetic field, external pressure, and the chemical composition. These three methods induce quantum fluctuations in the following way: disturbing the existing ordering, changing lattice constants, modifying electron kinetic energies or interaction strengths, and doping electron/hole carriers.

1.3.1 Transverse Magnetic Field

Quantum mechanically, the effect of a transverse magnetic field $\mathbf{B} = B\mathbf{e}_x$ is to flip the direction of magnetic moments perpendicular to the field. Let us consider the transverse field Ising model [38]:

$$H_I = -J \sum_{\langle i,j \rangle} s_i^z s_j^z - Jg \sum_i s_i^x, \tag{1.14}$$

with $J > 0$. Without the second term, the system is for $T = 0$ in the ferromagnetic state in which all the spins point in the same direction, i.e. the ground state is either $\prod_i |\uparrow, i\rangle$ or $\prod_i |\downarrow, i\rangle$. The transverse magnetic field flips spins. For $g \to \infty$ all spins are aligned in the x-direction, i.e. the ground state is $\prod_i \frac{1}{\sqrt{2}} \Big(|\uparrow, i\rangle + |\downarrow, i\rangle \Big)$. It can easily be shown that there exists a critical value $g = g_c$ where long range magnetic ordering disappears and the system becomes a quantum paramagnetic. A recent experimental realization [4] is $CoNb_2O_6$ whose $Co - O - Co$ chain along c-axis forms a 1D transverse field Ising chain. This experiment, using nuclear magnetic resonance (NMR) to investigate quantum spin fluctuations in $CoNb_2O_6$, provides results consistent with that of theoretical calculation. The phase diagram is shown in Fig.(1.4).

1.3.2 External Pressure

It is widely known that by applying external pressure a system may undergo a transitions into a new phase. To have a qualitative physical picture, we consider the Hubbard model:

$$H_{Hubbard} = -t \sum_{\langle i,j \rangle, \sigma} c_{i,\sigma}^\dagger c_{j,\sigma} + U \sum_i n_{i,\uparrow}^c n_{i,\downarrow}^c. \tag{1.15}$$

where t is the nearest neighbor hopping strength, U is the Hubbard potential, $c_i(c_i^\dagger)$ is the annihilation (creation) operator of fermion, and $n_{i,\sigma}^c$ is the number operator of fermion on site i with spin σ. It is known that by controlling the ratio between t and U, there is a insulator-metal transition at $t = t_c$ for fixed U. Applying pressure, which decreases the distance between sites, is equivalent to increasing t. Therefore, by an external pressure a Hubbard insulator can become a metal. Similar ideas apply to other materials. Here, an example [5] of a Mott insulator - superconductor phase transition in a spin-frustrated organic conductor $\kappa - (ET)_2Cu_2(CN)_3$ by applying pressure is shown in Fig.(1.5).

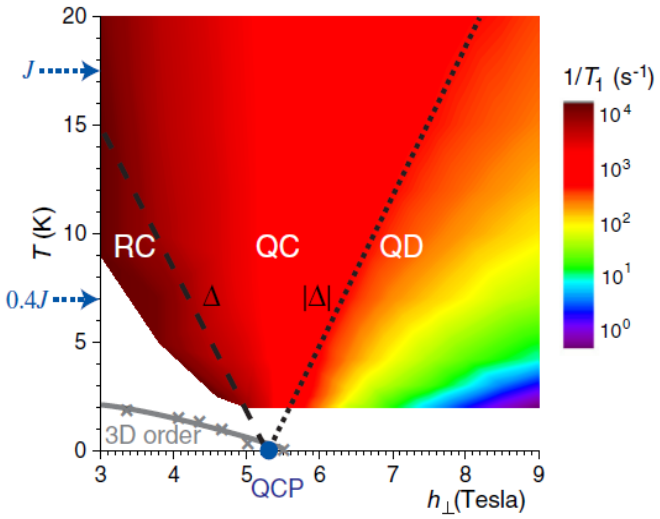

Figure 1.4: *The phase diagram of $CoNb_2O_6$ as a function of temperature and transverse magnetic field $h_\perp$ [4]. $Co-O-Co$ chain along c-axis forms a 1D transverse field Ising chain. By applying a transverse magnetic field, long range magnetic ordering is disturbed and eventually destroyed at a critical field $h_\perp = h_\perp^c = 5.25\ T$ and the system becomes a quantum paramagnet..*

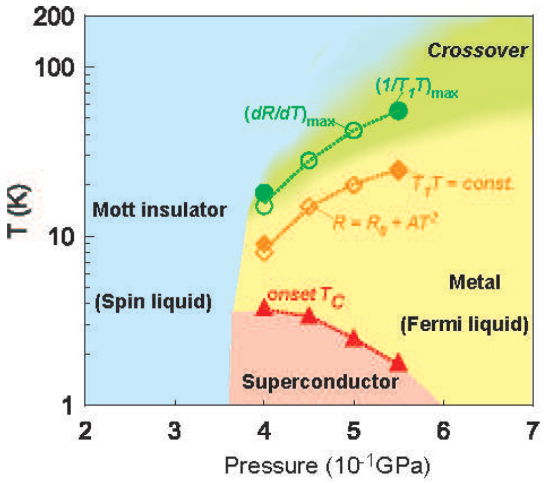

Figure 1.5: *Phase diagram of a quasi-two-dimensional organic charge transfer salt as a function of temperature and pressure [5]. A Mott-insulating spin liquid phase is seperated from matallic state that becomes superconducting at low temperature. A quantum phase transition as a function of pressure takes place at $P = 0.36\ GPa$. This is interpreted that for sufficiently large pressure, hopping between sites becomes strong enough to overcome the onsite Coulomb potential.*

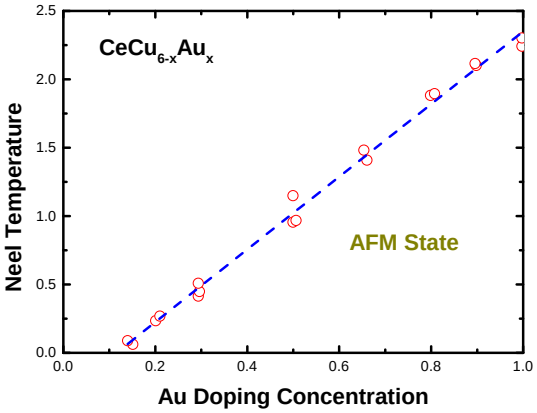

Figure 1.6: *Phase diagram of $CeCu_{6-x}Au_x$ as a function of temperature and Au doping concentration [6]. A heavy fermion PM phase is seperated from the AFM phase. A quantum phase transition as a function of Au impurity concentration x takes place at $x_c = 0.1$. The interpretation is that as doped Au increases interatomic spacing and weakens Kondo screening such that RKKY dominates and magnetic ordering emerges [7].*

1.3.3 Chemical Composition

Changing the chemical composition is another widely used technique to tune the materials properties between distinct states of matter. It can change physical properties of the host by changing lattice constants, carrier concentration, magnetic structure, and electronic configuration. A well known example of quantum criticality [6] is observed in $CeCu_{6-x}Au_x$ shown in Fig.(1.6). In this case, doped Au increases interatomic spacing and weakens Kondo screening such that Ruderman-Kittel-Kasuya-Yosida (RKKY) interaction, which describes the interaction between non-overlapped f-electrons via their couplings to conduction band [46], dominates and magnetic ordering emerges [7].

A recent experimental study on itinerant antiferromagnet $Ce_{1-x}La_xCu_2Ge_2$ shows astonishingly robust long range magnetic ordering against non-magnetic impurity doping [1] : antiferromagnetism exists up to $x = 0.8$ and $x = 0.9$, respectively. The phase diagram is shown in Fig.(1.1). Comparing with Fig.(1.6) in which the phase diagram shows sensitivities with regards to doping, the robustness of antiferromagnetism against La doping in the latter system is interesting and triggered this numerical study on impurity controlled quantum criticality. To study the effect of non-magnetic impurity doping on heavy fermion antiferromagnetic system, we choose the Anderson lattice model which captures the underlying physics: the interplay between heavy fermion physics and antiferromagnetism, with the hope to gain insight into the disorder driven quantum criticality.

1.4 Anderson Lattice Model

To study heavy fermion systems, the Anderson lattice model is used to capture the essential aspects

of intermetallic rare-earth compounds: strong coupling between local states and conduction band and strong electron-electron interaction on the rare earth 4f-sites. The full Hamiltonian can be written as

$$\begin{aligned} H &= \sum_{\langle i,j\rangle,\sigma} \left(t_{ij} - \mu\delta_{ij}\right) c^{\dagger}_{i,\sigma} c_{j,\sigma} + \sum_{i,\sigma} \epsilon_0 f^{\dagger}_{i,\sigma} f_{i,\sigma} \\ &\quad + U \sum_{i} f^{\dagger}_{i,\uparrow} f_{i,\uparrow} f^{\dagger}_{i,\downarrow} f_{i,\downarrow} + \sum_{i,j,\sigma} \left(V_{i,j} f^{\dagger}_{i,\sigma} c_{j,\sigma} + V^{*}_{i,j} c^{\dagger}_{j,\sigma} f_{i,\sigma}\right). \end{aligned} \tag{1.16}$$

Here the operators $c^{\dagger}_{i,\sigma}(c_{i,\sigma})$ represents conduction electron creation (annihilation) operator with spin σ on site i and $f^{\dagger}_{i,\sigma}(f_{i,\sigma})$ represents f-shell electron creation (annihilation) operator with spin σ on site i. The first term describes the dispersion of the non-interacting conduction band, the second and third terms represent four different local energy states, while the last term contributes to the hybridization between local sites and conduction band. Using a canonical transformation with the assumptions that $|\epsilon_0|, |\epsilon_0 + U| \gg |V_{i,j}|$ such that only local singly occupied states $|\uparrow\rangle$ and $|\downarrow\rangle$ are possible, the Anderson lattice model can be mapped onto the Kondo lattice model:

$$H_{Kondo} = \sum_{i,j,\sigma} \left(t_{ij} - \mu\delta_{ij}\right) c^{\dagger}_{i,\sigma} c_{j,\sigma} + \sum_{i,j,\sigma} J^{(K)}_{ij} \left(\mathbf{S}_i \cdot \mathbf{s}_j - \frac{\langle n_c \rangle}{4}\right), \tag{1.17}$$

where $J^{(K)}_{ij} \sim \frac{2|V_{ij}|^2 U}{U+\epsilon_0} > 0$. This suggests that similar to the single ion Kondo effect in an organized lattice of spins, Kondo behavior is to be expected also for this system. Therefore, an AFM state is expected.

The RKKY interaction [46] mediates an interaction among f-shell electrons by a weak coupling between local spin and conduction electrons: a local spin spatially modulates the conduction electrons such that nearby local spins are subjected to the magnetic field produced by spin polarized electrons. This may induce long range magnetic ordering. One the other hand, if the hybridization is sufficiently strong, then Kondo physics dominates: conduction electrons and local spin form a spin singlet as if the local spin never existed [33]. An important consequence of this strong coupling is that conduction electrons acquire significant mass hundred times more heavier than the bare electron mass and the energy scales of related physics phenomena decrease significantly. This competition between RKKY and Kondo is captured by Doniach's diagram shown in Fig.(1.7).

Close to the critical coupling $J = J_c$ (that can be reached for example by applying pressure), both energy scales T_K and T_{RKKY} are comparable. As these scales tend to cancel each other, new sub-leading channels may emerge, therefore interesting physics such as non-Fermi liquid behavior, unconventional superconductivity, and the coexistence of magnetism and superconductivity can emerge close to this critical point.

Instead of using Kondo lattice model, which is proven to be successful in describing heavy fermion antiferromagnetic and superconducting phases [47, 48], in this thesis we choose Anderson lattice model as the Hamiltonian because we want to substitute non-magnetic impurities into the system without changing the conduction band carrier concentration. This method will be described in chapter 3.

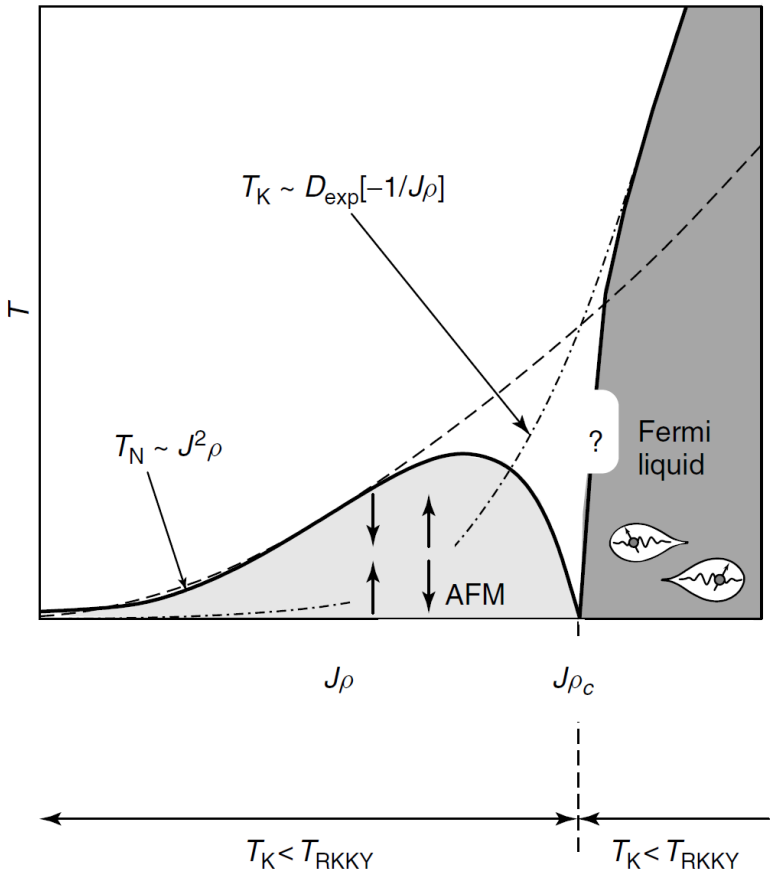

Figure 1.7: *Doniach phase diagram as a function of temperature and cf-hybridization $J\rho$ [8, 9]. It captures the consequence of competition between RKKY interaction and Kondo exchange interaction. An AFM state is seperated from fermi liquid state at low T. A quantum phase transition as a function of $J\rho$ takes place at $J\rho_c$. For sufficiently small $J\rho$, RKKY interaction dominates and AFM arises. In the other limit, local spin moments are screened by conduction band electrons due to strong Kondo exchange and the system becomes a heavy fermion liquid state.*

1.5 Dynamical Mean Field Theory and Coherent Potential Approximation

In this section we will give introductions to dynamical mean field theory (DMFT) and coherent potential approximation (CPA), including their developments, advantages, restrictions, and applications. Although these two different techniques were developed to solve very different problems: DMFT for strongly correlated lattice system and CPA for alloys in the framework of conventional band theory, it turns out that the underlying ideas are very similar.

In DMFT, which assumes a local self-energy, a lattice problem is mapped onto a single impurity problem that can be solved by impurity solvers and the resulting impurity Green's function $G_{imp}(\omega)$ and self-energy $\Sigma_{imp}(\omega)$ should be the same as the corresponding lattice Green's function $G_{latt}(\omega)$ and lattice self-energy $\Sigma_{latt}(\omega)$, because they are describing the identical system. While in CPA, a lattice problem with various constitutes is characterized by the atomic energy ϵ_i and the concentration x_i, is mapped onto a single impurity problem. The resulting Green's function of the system $G_{eff}(\omega)$ is the weighted sum of the local Green's function $G_i(\omega)$:

$$G_{eff}(\omega) = \sum_i x_i G_i(\omega). \tag{1.18}$$

In the CPA framework, a Hubbard potential can be incoporated such that each site i is not only characterized by the atomic energy ϵ_i, but also by the potential U_i. As a result, CPA can be seen as the disorder version of DMFT.

1.5.1 Coherent Potential Approximation

In the mid of the twentieth century, the understanding of macroscopic properties, such as single particle excitation, of disordered systems had made a great progress from the theoretical side, thanks to more and more available experimental data [49]. The following one-particle Hamiltonian is used for an independent particle approximation in which the distribution of atoms is statistically independent and homogeneous in space

$$H_{alloy}^{general} = -\sum_{i\neq j}\sum_{\mu,\nu,\sigma} t_{ij}^{\mu\nu}\left(c_{i,\sigma}^{\mu}\right)^{\dagger}\left(c_{j,\sigma}^{\nu}\right) + \sum_{i,\mu}\epsilon_i^{\mu}\left(c_{i,\sigma}^{\mu}\right)^{\dagger}\left(c_{i,\sigma}^{\mu}\right). \tag{1.19}$$

The first term describes the hopping between site i and site j, as well as between orbital μ and ν with strength $t_{ij}^{\mu\nu}$, and the second term describes on-site energy ϵ_i^{μ} on site i and orbital μ. CPA [50], which was proposed to study binary alloys $A_{1-x}B_x$, focuses on a special case of Eq.(1.19):

$$H_{CPA} = -\sum_{k,\sigma} t_{ij} c_{i,\sigma}^{\dagger} c_{j,\sigma} + \sum_{i,\sigma}\epsilon_i c_{i,\sigma}^{\dagger} c_{i,\sigma}, \tag{1.20}$$

with t_{ij} following translational invariance and ϵ_i is a random variable having two possible outcomes ϵ_A and ϵ_B with probability $P(\epsilon_i = \epsilon_A) = 1 - x$ and $P(\epsilon_i = \epsilon_B) = x$, respectively. The requirement that t_{ij} is translational invariant gives an assumption: doping B should not change the non-interacting density of states ρ_0 of the host A or equivalently A and B contribute the same orbital for binding.

Within CPA the difference in energy ϵ_A and ϵ_B is smeared out and they are replaced by an effective medium represented by a local self energy $\Sigma_{CPA}(\omega)$, such that Eq.(1.20) is equivalent to

$$H_{eff} = \sum_{i,\sigma} \Sigma_{CPA}(\omega)\, c^{\dagger}_{i,\sigma} c_{i,\sigma} + \sum_{k} \epsilon_k c^{\dagger}_{k,\sigma} c_{k,\sigma}. \tag{1.21}$$

The resulting local Green's function, which is equivalent to the Weiss field in a mean field theory, is

$$G_{eff}(\omega) = \sum_{\mathbf{k}} \frac{1}{\omega - \epsilon_{\mathbf{k}} - \Sigma_{CPA}(\omega)}. \tag{1.22}$$

On the other hand, Eq.(1.20) can also be disintegrated into two parts:

$$H_{imp} = \sum_{i,\sigma} \left(\epsilon_i - \Sigma_{CPA}(\omega)\right) c^{\dagger}_{i,\sigma} c_{i,\sigma} + \sum_{k} \left(\epsilon_k + \Sigma_{CPA}(\omega)\right) c^{\dagger}_{k,\sigma} c_{k,\sigma}. \tag{1.23}$$

In CPA formalism, we consider the Weiss field scatters with a certain site multiple times and a corresponding $t-$matrix T_i is obtained depending on the type of the site. The self-consistent condition is that the average of scattering due to on-site energy fluctuation is zero:

$$\langle T_i \rangle = (1-x)\, T_A + x T_B = 0, \tag{1.24}$$

which is equivalent to the statement that the averaged single particle Green's function on sites A and B is equal to the Weiss field:

$$\langle G_i \rangle = (1-x)\, G_A(\omega) + x G_B(\omega) = G_{eff}(\omega), \tag{1.25}$$

with

$$G_i(\omega) = \frac{1}{G^{-1}_{eff}(\omega) - \left(\epsilon_i - \Sigma_{CPA}(\omega)\right)}. \tag{1.26}$$

Although CPA is developed for binary alloys with random on-site energy, it can be extend to alloys with N components as long as they give the same non-interacting density of states. While the type of on-site energy ϵ_i is not restricted to eletronic states. It is possible to choose ϵ_i as phonons [51, 52], excitons [53, 54], ferromagnetic interactions in dilute magnetic semiconductors [55, 56], and Hubbard interactions [57]. In the case of noble alloys such as AgAu, a two-bands description is required because their band structures indicate that a narrow d band hybridizes with a broad $s-p$ band. Eq.(1.20) can be extended to [58]

$$H_{Nobel} = \sum_{k,\sigma} \epsilon_k s^{\dagger}_{k,\sigma} s_{k,\sigma} + \sum_{i,\sigma} \epsilon_i d^{\dagger}_{i,\sigma} d_{i,\sigma} + \sum_{k,\sigma} \gamma \left[s^{\dagger}_{k,\sigma} d_{k,\sigma} + d^{\dagger}_{k,\sigma} s_{k,\sigma} \right] \tag{1.27}$$

which is similar to the Anderson lattice model without local Coulomb interaction.

Although CPA is an ideal tool to study single particle excitations, it should be used carefully to study real world materials. For example, constitute compositions should give the same non-interacting density of states ρ_0 and there should be no structural disorder or cluster effects.

1.5.2 Dynamical Mean Field Theory

DMFT has its root deep in the development of in the theory of strongly correlated systems. Conventional band theory, which treats electrons as non-interacting particles subjected to an external periodic potential, has successfully explained various electronic properties in metallic compounds. For example, if the number of electrons N_e in the unit cell is odd, then the material is a conductor. However, Verwey and de Boer pointed out that transition-metal oxides NiO, CoO, MnO, Fe_2O_3, Mn_3O_4, and Co_3O_4 were insulators instead of conductors [59]. It was a surprise from the point of view of conventional band theory, because all these transitional metal elements have partially filled d-shell.

The importance of interaction between electrons was then noticed [60] and this became the Mott insulator problem. Later, a model as shown in Eq.(1.15), was proposed to illustrate the competition between conducting and insulating phases by taking local electron-electron interaction into account [61–63]. To see the phase transition, let us consider two limits at zero temperature at half-filling seperately: 1. $t \gg U$; 2. $t \ll U$. In the first case, kinetic energy dominates and the ground state should be that of a free electron gas:

$$\big|FS\big\rangle = \prod_{|\mathbf{k}|<k_F} \big|\uparrow\downarrow, \mathbf{k}\big\rangle\,. \tag{1.28}$$

In the second case, intra-atomic interaction dominates and the ground state is that each site is occupied by one electron. Due to strong Coulomb repulsion, electrons cannot hop onto other sites, such that this is an insulating phase. Hence, somewhere between these two limits there should be a phase transition. However, this phase transition is expected to take place at $t \sim U$ such that perturbation theory breaks down because neither t/U nor U/t are well-controlled parameters. Therefore a non-perturbative method (at least not in t/U nor U/t) is needed.

Despite its simple form, the Hamiltonian in Eq.(1.15) is extremely difficult to be solved. So far, only its 1-D case is solved exactly [64]. On the other hand, great progresses has been made in solving the quantum impurity problems numerically:

$$\begin{aligned} H_{SIAM} &= \sum_{\sigma} \epsilon_0 f_\sigma^\dagger f_\sigma + U n_\uparrow^f n_\downarrow^f + \sum_{k,\sigma} \epsilon_k c_{k,\sigma}^\dagger c_{k,\sigma} \\ &\quad + \sum_{k,\sigma} \Big[V_k f_\sigma^\dagger c_{k,\sigma} + V_k^* c_{k,\sigma}^\dagger f_\sigma \Big] \end{aligned} \tag{1.29}$$

or

$$H_{Kondo} = -J\mathbf{S}\cdot\mathbf{s} + \sum_{k,\sigma} \epsilon_k c_{k,\sigma}^\dagger c_{k,\sigma} \tag{1.30}$$

with impurity solvers such as numerical renormalization group (NRG) [36, 37, 65] and quantum Monte Carlo simulations (QMC) [66]. Eq.(1.29) is called single impurity Anderson model and Eq.(1.30) is called Kondo model. In mean field theory, a lattice problem is mapped onto a single site model, whose local degree of freedoms couple to a Weiss field [67, 68]. This Weiss field can be thought of as a spatially and temporally averaged effective conjugate field due to the environment of the site we have interest in. One may wonder if it is possible to transform the Hubbard model into Eq.(1.29) or Eq.(1.30) and solve this problem self-consistently with the help of impurity solvers and obtain thermodynamical properties. If it is possible, what is the condition?

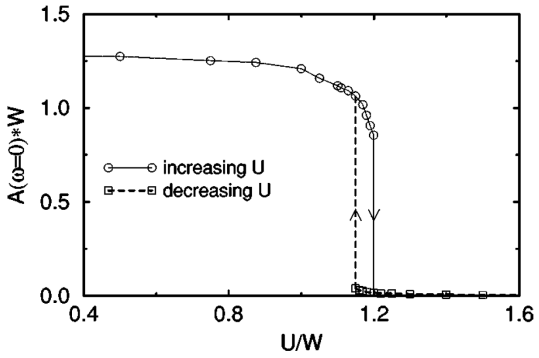

Figure 1.8: *Phase diagram of Hubbard model as a function of Hubbard potential U and single particle excitation $A(\omega = 0)$ [10]. A conducting state is seperated from insulating state at $\frac{U}{W} \approx 1.2$. The phase diagrams with respect to increasing U and decreasing U are different. This hysteresis loop is interpreted as a first order phase insulator-conductor transition.*

The answer is yes: DMFT shows that it is possible to map a lattice problem onto a single impurity problem under the condition that the coordination number z goes to infinity or the self-energy $\Sigma_{ij}(\omega)$ is local [69]. In the DMFT framework, similar to mean field theory, these is also a Weiss field as function of time or frequency. Derivation based on the cavity method and path integrals on the Hubbard model can be found in [68] and for the Anderson lattice model will be shown in Sec.1.5.2. The logic behind the cavity method is simple: a site 0 is isolated from the lattice and the environement forms an effective Weiss field acting on this isolated site, then the Weiss field is calculated self-consistently with the Green's function of the isolated site. Impurity solvers such as NRG or QMC are used to perform the calculation.

With NRG + DMFT, it can be shown that there is a first order insulating phase transition below a phase transition temperature T_c [10] that be observed by the hysteresis quasi-particle peaks as a function of Hubbard potential U shown in Fig.(1.8).

Today, DMFT has become one of the most active research topics in condensed matter theory. It includes mapping a lattice model onto a single impurity model or vice versa as well as developing impurity solvers for single impurity models and for physical quantities one wants to probe experimentally. There are various impurity solvers that can incorporate DMFT [70] and the applications are not limited to fermions. Each of these impurity solvers has its strength and ideal topics to be investigated. For example, NRG can be used to study superconductivity, ferromagnetism, commensurate antiferromagnetism, while QMC is specialized to spin systems. Bosonics systems [71, 72] and even system, which mixes bosons and fermions [73], can be investigated in the framework of DMFT. Moreover, the recent development in local density approximation (LDA) + DMFT makes it possible to study the real world strongly correlated materials more accurately [74].

Dimensionality Scaling Analysis

It was first observed by Metzner and Vollhardt [69] that when the dimensionality (or coordination number) of the system goes to infinite, the self energy of the system becomes local (i.e. momentum independent).

Here we perform a scaling analysis of a tight-binding model on a d-dimensional hypercubic lattice [75, 76]. The kinetic energy of the system is

$$H_{\text{kin}} = -2t \sum_{k_1} \cdots \sum_{k_d} \left(\cos k_1 a + \cdots + \cos k_d a\right) c_{\mathbf{k}}^{\dagger} c_{\mathbf{k}} \tag{1.31}$$

and the corresponding dispersion relation is

$$\begin{aligned} \epsilon\left(\mathbf{k}\right) &= -2t \left(\cos k_1 a + \cdots + \cos k_d a\right) \\ &= -2t \sum_{i=1}^{d} \cos k_i a \end{aligned} \tag{1.32}$$

Now we treat each of $-2t\sqrt{d}\cos k_i a$ as a random variable K_i with a uniform distribution $\frac{a}{2\pi}$ in the region $\left[-\frac{\pi}{a}, \frac{\pi}{a}\right]$ such that

$$\epsilon\left(\mathbf{k}\right) \equiv X = \frac{1}{\sqrt{d}} \sum_{i=1}^{d} K_i \tag{1.33}$$

Then the K_is are independent identical distributions which have average 0 and variance $2dt^2$. Then X follows normal distribution

$$P_X\left(x\right) = \frac{1}{t\sqrt{4\pi d}} \exp\left(-\frac{x^2}{4dt^2}\right) \tag{1.34}$$

by central limit theorem (CLT) in the limit $d \to \infty$. To have a finite variable, we have to rescale t properly:

$$dt^2 = t^{*2}, \tag{1.35}$$

which means that the hopping strength follows the scaling law with respect to the dimensionality d:

$$t \sim \frac{1}{\sqrt{d}}. \tag{1.36}$$

From this result we obtain how the Green's function scales with respect to the dimensionality d. From Eq.(1.31) in real space, we have

$$\frac{\left\langle H_{\text{kin}} \right\rangle}{N} = -\frac{t}{N} \sum_{\{i,j\}} \left\langle a_i^{\dagger} a_j \right\rangle \tag{1.37}$$

Since $\frac{\left\langle H_{\text{kin}} \right\rangle}{N}$ is finite, summation over i or j gives d (the other index counts all the lattice points and will be canceled by $\frac{1}{N}$). While $\left\langle a_i^{\dagger} a_j \right\rangle$ which can be interpreted as transition amplitude from site j to site i has the scaling form

$$\left\langle a_i^{\dagger} a_j \right\rangle \sim t \sim \frac{1}{\sqrt{d}} \tag{1.38}$$

This is consistent with the analysis that $\left|\left\langle a_i^\dagger a_j \right\rangle\right|^2 \sim \frac{1}{d}$ because the number of neighbor is $O\left(d\right)$ and the probability to hop from one site to any of its neighbor is equal. According to Eq.(1.38), the Green's function G_{ij} should have the scaling form

$$G_{ij} \sim d^{-\frac{\|i-j\|}{2}}, \tag{1.39}$$

where $\left\|i-j\right\|$ is the so-called New York metric because hopping can only takes place along the chemical bonds just like a taxi moving in Big Apple. We now use Eq.(1.39) to show that the self-energy becomes local when dimensionality becomes infinity.

Let us consider a two particle interaction, for example Hubbard interaction:

$$H_{int} = \frac{U}{2}\sum_{i,j} n_{i\sigma} n_{j\sigma}. \tag{1.40}$$

If we expand the corresponding self-energy in skeleton form, which means all the Green's functions are fully dressed Green's functions, we the see that any diagram having more than two different sites has at least three non-local Green's functions G_{ij}, which means the magnitude of these diagrams are suppressed at least by a factor $d^{-\frac{3\|i-j\|}{2}}$. By fixing i and summing over j, we obtain another factor $d^{\|i-j\|}$ for the self-energy. Therefore self-energies including more than one site are suppressed by $d^{-\frac{\|i-j\|}{2}}$ and we conclude that in the limit $d \to \infty$ the self-energy is local:

$$\Sigma_{ij}\left(\omega\right) = \delta_{ij}\Sigma\left(\omega\right) \tag{1.41}$$

and contains only local Green's function $G_{ij}\left(\omega\right) = \delta_{ij}G\left(\omega\right)$.

Free Energy Analysis

Besides the scaling analysis, there is another way to conclude that only local Green's function $G_{ii}\left(\omega\right)$ have to be considered based on the assumption that the self-energy is local as shown in Eq.(1.41).

According to Ref.[77], the thermodynamical potential (free energy) Γ can be written as a functional of full Green's function G:

$$\Gamma\left(G\right) = \mathrm{Tr}\log G - \mathrm{Tr}\left(\Sigma G\right) + \Phi\left(G\right), \tag{1.42}$$

with $\Phi\left(G\right)$ the sum of all compact diagrams and Σ the self-energy. Because G is the solution of potential Γ, Γ must be at its extreme; therefore the variation of Γ with respect to G is zero [78]:

$$\frac{\delta\Gamma\left(G\right)}{\delta G} = 0. \tag{1.43}$$

Applying functional derivative on Eq.(1.42), we arrive at

$$\delta\Gamma\left(G\right) = \left(\frac{\delta\Phi\left(G\right)}{\delta G} - \Sigma\right)\delta G. \tag{1.44}$$

With the condition imposed by Eq.(1.43), we obtain

$$\Sigma = \frac{\delta\Phi\left(G\right)}{\delta G}. \tag{1.45}$$

By requiring that Σ is local (Eq.(1.41)), we see from the equation above that only the local Green's function is taken into account in $\Phi\left(G\right)$. As a result, $\Phi\left(G\right)$ is constructed by the local Green's function. The traces over $\log G$ and ΣG also show that only the local Green's functions are taken into account,. Therefore, we conclude that free energy is composed of only local Green's function.

DMFT on Anderson Lattice Model

Here, the derivation of the mapping of the Anderson lattice model onto a single impurity problem is shown by using cavity method. We start from the partition function

$$Z = \int \prod_i D\left[c^\dagger_{i,\sigma} c_{i,\sigma}\right] \prod_i D\left[f^\dagger_{i,\sigma} f_{i,\sigma}\right] e^{-S} \tag{1.46}$$

with the action corresponding to the Anderson lattice model shown in Eq.(1.16) with $V_{ij} = \delta_{ij} V$:

$$\begin{aligned} S &= \int_0^\beta d\tau \left[\sum_{i,\sigma} f^\dagger_{i,\sigma} \partial_\tau f + \sum_{i,\sigma} c^\dagger_{i,\sigma} (\partial_\tau + \mu) c_{i,\sigma} + \sum_{i,\sigma} \epsilon_0 f^\dagger_{i,\sigma} f_{i,\sigma} + \sum_i U n^f_{i,\uparrow} n^f_{i,\downarrow} \right. \\ &\left. + V \sum_{i,\sigma} \left(f^\dagger_{i,\sigma} c_{i,\sigma} + c^\dagger_{i,\sigma} f_{i,\sigma} \right) - \sum_{i,j} t_{ij} c^\dagger_{i,\sigma} c_{j,\sigma} \right] \end{aligned} \tag{1.47}$$

After integrating out the conduction band degrees of freedem [67], Eq.(1.47) can now be written as

$$\begin{aligned} S^{(f)}_{eff} &= \int_0^\beta d\tau \left[\sum_{i,\sigma} f^\dagger_{i,\sigma} \partial_\tau f + \sum_{i,\sigma} \epsilon_0 f^\dagger_{i,\sigma} f_{i,\sigma} + \sum_i U n^f_{i,\uparrow} n^f_{i,\downarrow} \right. \\ &\left. + \sum_{\mathbf{k},\sigma} f^\dagger_{\mathbf{k},\sigma}(\tau) \frac{V^2}{i\omega - \epsilon_{\mathbf{k}}} f_{\mathbf{k},\sigma}(\tau) \right]. \end{aligned} \tag{1.48}$$

Next we put Eq.(1.48) into the form of Eq.(30) in [68] by requiring that

$$\sum_{\mathbf{k},\sigma} f^\dagger_{\mathbf{k},\sigma}(\tau) \frac{\hat{V}^2}{i\omega - \epsilon_{\mathbf{k}}} f_{\mathbf{k},\sigma}(\tau) = \sum_{ij} t_{ij} f^\dagger_{i,\sigma} f_{j,\sigma} \tag{1.49}$$

and we obtain

$$\begin{aligned} S^{(f)}_{eff} &= \int_0^\beta d\tau \left[\sum_{i,\sigma} f^\dagger_{i,\sigma} \partial_\tau f + \sum_{i,\sigma} \epsilon_0 f^\dagger_{i,\sigma} f_{i,\sigma} + \sum_i U n^f_{i,\uparrow} n^f_{i,\downarrow} \right. \\ &\left. + \sum_{ij,\sigma} t_{ij} f_{i,\sigma} f_{j,\sigma} \right] \end{aligned} \tag{1.50}$$

By following the procedure shown in [68], we obtain the equation of Weiss field G_0^{-1} for the f-shell electrons:

$$G_0^{-1} = i\omega - \epsilon_0 - \sum_{ij} t_{0i} t_{j0} G_{ij}^{(0)} \tag{1.51}$$

which describes the environment scattering with the *impurity* site. To obtain $G_{ij}^{(0)}\left(i\omega_n\right)$, we start from the Dyson equation with an effective medium represented by $G_{ij}\left(i\omega_n\right)$ scattering with the impurity site 0 with energy V, which is later sent to infinity:

$$\begin{aligned} \lim_{V\to\infty} G_{ij}\left(V\right) &= G_{ij} + \lim_{V\to\infty} G_{i0} V G_{0j}\left(V\right) \\ &= G_{ij} - \frac{G_{i0}G_{0j}}{G_{00}}. \end{aligned} \tag{1.52}$$

In the end, combining Eq.(1.51) and Eq.(1.52) we have to calculate

$$\sum_{ij} t_{0i} t_{j0} \left(G_{ij} - \frac{G_{i0}G_{0j}}{G_{00}} \right) \tag{1.53}$$

The first part reads

$$\sum_{ij} t_{0i} t_{j0} G_{ij} = \int d\epsilon \frac{D\left(\epsilon\right)\Gamma\left(\epsilon\right)^2}{i\omega - \epsilon_0 - \Gamma - \Sigma} \tag{1.54}$$

with $\Gamma = \frac{V^2}{i\omega - \epsilon_{\mathbf{k}}}$. The equation above becomes

$$\begin{aligned} \int d\epsilon \frac{D\left(\epsilon\right)\Gamma\left(\epsilon\right)^2}{i\omega - \epsilon_0 - \Gamma - \Sigma} &= -\int d\epsilon D\left(\epsilon\right)\Gamma\left(\epsilon\right) - \left(i\omega - \epsilon_0 - \Sigma\right) \\ &\quad + \left(i\omega - \epsilon_0 - \Sigma\right)^2 G_{00} \end{aligned} \tag{1.55}$$

and the numerator of the second order can be written as

$$\sum_{ij} t_{0i} G_{i0} = -1 + \left(i\omega - \epsilon_0 - \Sigma\right) G_{00} \tag{1.56}$$

As a result, we have

$$G_0^{-1} = \Sigma + G_{00}^{-1} \tag{1.57}$$

with G_{00} the local Green's function and Eq.(1.57) is the self-consistent condition for the Weiss field. In Eq. (1.57) we use the result that

$$\int d\epsilon D\left(\epsilon\right)\Gamma\left(\epsilon\right) = 0 \tag{1.58}$$

Therefore, starting from the Weiss field G_0^{-1} and the Coulomb potential, a single impurity problem can be solved and the self-energy Σ is obtained. Then, the lattice Green's function G_{00} can be obtained. By using the self-energy Σ and lattice Green's function G_{00}, a new Weiss field G_0^{-1} is obtained. This problem is solved self-consistenly until the input and output Weiss fields are sufficiently similar. Detailed algorithms for this iteration will be given in Chapter 3.

Chapter 2
2 Model

The parent compound of heavy fermion system $Ce_{1-x}La_xCu_2Ge_2$ is shown in Fig.(2.1) [11]. La plays the role of non-magnetic impurity doping and substitutes Ce, which contributes local moment by $4f$-electron [12]. $CeCu_2Ge_2$ is an AFM system with Néel temperature $T_N \sim 4$K [1]. By substituting Ce by non-magnetic La, long-range magnetic ordering is suppressed and eventaully vanishes.

The parent compound $CeCu_2Ge_2$ can be described as a system composed of conduction band states and the localized f-orbitals of cerium. Because $f-$orbitals are highly localized, the electron-electron Coulomb interaction must be taken into account. The dominant part of this interaction is the on-site Coulomb interaction. $LaCu_2Ge_2$ is an intermetallic compound [79]. The conduction band, composed of $d-$orbitals, is approximately singly occupied. It can be assumed that this conduction band is well described by traditional band theory and strong Coulomb correlation effects are not relevant. Since spins originate from the $f-$orbitals, a hybridization with conduction band is required to give rise to heavy fermion behavior.

As a result, we start from the Anderson lattice model which is composed of three parts:

$$H = H_{\text{loc}} + H_{\text{hyb}} + H_{\text{c}} \tag{2.1}$$

with H_{loc} the local site Hamiltonian, H_{hyb} describing the hybridization between local sites and the conduction band, and H_{c} the conduction band Hamiltonian. Since each cerium contributes one f-orbital acting as the local energy level, we use Ce as the symbol for lattice points which contribute local states. The corresponding second quantized form is

$$\begin{aligned} H_{\text{loc}} &= \sum_{\sigma}\sum_{i\in\text{Ce}} \epsilon_0 f^{\dagger}_{i,\sigma} f_{i,\sigma} + U \sum_{i\in\text{Ce}} f^{\dagger}_{i,\uparrow} f_{i,\uparrow} f^{\dagger}_{i,\downarrow} f_{i,\downarrow} \\ H_{\text{hyb}} &= V \sum_{\sigma}\sum_{i\in\text{Ce}} \left(f^{\dagger}_{i,\sigma} c_{i,\sigma} + c^{\dagger}_{i,\sigma} f_{i,\sigma} \right) \\ H_{\text{c}} &= \sum_{\sigma}\sum_{i,j} t_{ij} c^{\dagger}_{i,\sigma} c_{j,\sigma} \end{aligned} \tag{2.2}$$

where $f^{\dagger}_{i,\sigma}$ ($f_{i,\sigma}$) is the creation (annihilation) operator on a local orbital at site i and with spin σ. $c^{\dagger}_{i,\sigma}$ ($c_{i,\sigma}$) is the creation (annihlation) operator on a Wannier orbital at site i with spin σ, ϵ_0 is the local site energy measured relative to chemical potential, t_{ij} describes the hopping between two sites, U is the Hubbard interaction, and V is the strength of the hybridization.

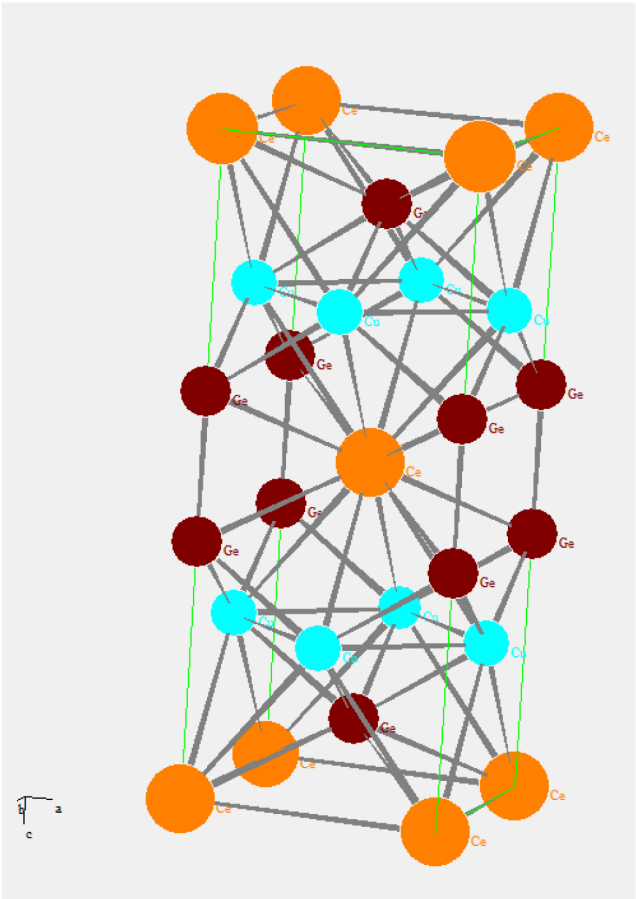

Figure 2.1: *Lattice structure of $CeCu_2Ge_2$ [11]. Cerium atoms are represented by the orange spheres, germanium atoms are represented by the brown spheres, and copper atoms are represented by the cyan atoms. Cerium has eletronic structure $[Xe]\,4f^1 5d^1 6s^2$. Extensive 5d- orbitals of Ce overlap with the outer orbitals of Cu and Ge to form the conduction band and $4f$-electrons are localized and provide magnetic moment of the lattice [12].*

This Hamiltonian can be generalized to all sites, those with Ce and those with La atoms, with a simple trick:

$$\begin{aligned} H_{\rm loc} &= \sum_{\sigma}\sum_{i}\epsilon_i f^{\dagger}_{i,\sigma}f_{i,\sigma} + \sum_{i} U_i f^{\dagger}_{i,\uparrow}f_{i,\uparrow}f^{\dagger}_{i,\downarrow}f_{i,\downarrow} \\ H_{\rm hyb} &= V\sum_{\sigma}\sum_{i}\left(f^{\dagger}_{i,\sigma}c_{i,\sigma} + c^{\dagger}_{i,\sigma}f_{i,\sigma}\right) \\ H_{\rm c} &= \sum_{\sigma}\sum_{i,j} t_{ij}c^{\dagger}_{i,\sigma}c_{j,\sigma}, \end{aligned} \tag{2.3}$$

where

$$\left(\epsilon_i, U_i\right) = \begin{cases} \left(\epsilon_0, U\right) & \text{if } i \in \text{Ce} \\ \left(\infty, 0\right) & \text{if } i \in \text{La} \end{cases}. \tag{2.4}$$

It is assumed that conduction band hopping element t_{ij} and hybridization do not change by doping La. At a La site the artificial local energy is very high. Thus local level of La sites are decoupled from the rest of system and the two models Eq.(2.2) and Eq.(2.3) become equivalent. As we are considering a randomly diluted system, $\left(\epsilon_i, U_i\right)$ is governed by the probability distribution

$$\begin{aligned} P\left(\left(\epsilon_i, U_i\right) = \left(\epsilon_0, U\right)\right) &= 1 - x, \\ P\left(\left(\epsilon_i, U_i\right) = \left(\infty, 0\right)\right) &= x. \end{aligned} \tag{2.5}$$

Let us consider two important limits: 1. $\forall i:\ i \in$ Ce corresponds to $x = 0$ and is equivalent to the periodic Anderson lattice (PAM). 2. If only one Ce site exists, we recover the single impurity Anderson model (SIAM). For case 1, the Hamiltonian becomes

$$\begin{aligned} H &= \sum_{\sigma}\sum_{\mathbf{k}}\epsilon_0 f^{\dagger}_{\mathbf{k},\sigma}f_{\mathbf{k},\sigma} + U\sum_{\mathbf{k}} n^{f}_{\mathbf{k},\uparrow}n^{f}_{-\mathbf{k},\downarrow} \\ &\quad + V\sum_{\sigma}\sum_{\mathbf{k}}\left(f^{\dagger}_{\mathbf{k},\sigma}c_{\mathbf{k},\sigma} + c^{\dagger}_{\mathbf{k},\sigma}f_{\mathbf{k},\sigma}\right) + \sum_{\sigma}\sum_{\mathbf{k}}\epsilon_{\mathbf{k}}c^{\dagger}_{\mathbf{k},\sigma}c_{\mathbf{k},\sigma}, \end{aligned} \tag{2.6}$$

where $n^{f}_{\mathbf{k},\sigma}$ is the number operator f-electron with momentum $\mathbf{k}$ and spin σ. While the Hamiltonian of the SIAM can be written as [80]:

$$H_{SIAM} = \sum_{\sigma}\epsilon_0 f^{\dagger}_{\sigma}f_{\sigma} + U n^{f}_{\uparrow}n^{f}_{\downarrow} + \sum_{\sigma} V\left(f^{\dagger}_{\sigma}c_{0,\sigma} + c^{\dagger}_{0,\sigma}f_{\sigma}\right) + \sum_{\sigma}\sum_{i,j} t_{ij}c^{\dagger}_{i,\sigma}c_{j,\sigma}. \tag{2.7}$$

In the next chapter, we will show that by using the CPA, the Anderson lattice model can be mapped on to an effective SIAM. In the dilute limit it is equivalent to the actual SIAM.

We can give derivations of Green's functions on these two extreme cases by looking at their local Green's functions which will be important quantities in our work.

2.1 Green's Functions of the periodic and single-impurity Anderson models

2.1.1 Periodic Anderson Model

In this section, we derive the analytical form of the f-electron Green's function $G\left(f_{\mathbf{k},\sigma}, f^{\dagger}_{\mathbf{k},\sigma};\omega\right)$. Let us start from the PAM defined in Eq.(2.6) with Heisenberg equation of motion:

$$\begin{aligned} G\left(A,B;t\right) &= -i\Theta\left(t\right)\left\langle \left[A\left(t\right),B\left(0\right)\right]_{+}\right\rangle \\ \Rightarrow \omega G\left(A,B;\omega\right) &= \left\langle \left[A,B\right]_{+}\right\rangle + G\left(\left[A,H\right],B;\omega\right). \end{aligned} \tag{2.8}$$

Here we set $A = f_{\mathbf{k},\sigma}$ and $B = f^{\dagger}_{\mathbf{k},\sigma}$ and it follows

$$\omega G\left(f_{\mathbf{k},\sigma}, f^{\dagger}_{\mathbf{k},\sigma};\omega\right) = 1 + G\left(\left[f_{\mathbf{k},\sigma},H\right], f^{\dagger}_{\mathbf{k},\sigma};\omega\right) \tag{2.9}$$

where the commutator is given by

$$\left[f_{\mathbf{k},\sigma},H\right] = f_{\mathbf{k},\sigma}\epsilon_0 + U\sum_{\mathbf{p}} f_{\mathbf{k}-\mathbf{p},\sigma}n^{f}_{-\mathbf{p},\bar{\sigma}} + Vc_{\mathbf{k},\sigma}. \tag{2.10}$$

Thus we obtain

$$\begin{aligned} \omega G\left(f_{\mathbf{k},\sigma}, f^{\dagger}_{\mathbf{k},\sigma};\omega\right) &= 1 + \epsilon_0 G(f_{\mathbf{k},\sigma}, f^{\dagger}_{\mathbf{k},\sigma};\omega) + UG\left(\sum_{\mathbf{p}} f_{\mathbf{k}-\mathbf{p},\sigma}n^{f}_{-\mathbf{p},\bar{\sigma}}, f^{\dagger}_{\mathbf{k},\sigma};\omega\right) \\ &\quad + VG\left(c_{\mathbf{k},\sigma}, f_{\mathbf{k},\sigma};\omega\right). \end{aligned} \tag{2.11}$$

The third term in the RHS of Eq.(2.11) can be used to define the self energy $\Sigma_{\sigma}\left(\mathbf{k},\omega\right)$ [81]:

$$UG\left(\sum_{\mathbf{p}} f_{\mathbf{k}-\mathbf{p},\sigma}n^{f}_{-\mathbf{p},\bar{\sigma}}, f^{\dagger}_{\mathbf{k},\sigma};\omega\right) = \Sigma_{\sigma}\left(\mathbf{k},\omega\right)G\left(f_{\mathbf{k},\sigma}, f^{\dagger}_{\mathbf{k},\sigma};\omega\right) \tag{2.12}$$

The last term in Eq.(2.11) can be written as a function of f-electron Green's function by using Heisenberg equation of motion:

$$\begin{aligned} \omega G\left(c_{\mathbf{k},\sigma}, f_{\mathbf{k},\sigma};\omega\right) &= G\left(\left[c_{\mathbf{k},\sigma},H\right], f^{\dagger}_{\mathbf{k},\sigma};\omega\right) \\ \Rightarrow G\left(c_{\mathbf{k},\sigma}, f_{\mathbf{k},\sigma};\omega\right) &= \frac{V}{\omega-\epsilon_{\mathbf{k}}}G\left(f_{\mathbf{k},\sigma}, f^{\dagger}_{\mathbf{k},\sigma};\omega\right) \end{aligned} \tag{2.13}$$

From Eq.(2.12) and Eq.(2.13), Eq.(2.11) can be written as

$$\left(\omega - \epsilon_0 - \frac{V^2}{\omega-\epsilon_{\mathbf{k}}}\right)G\left(f_{\mathbf{k},\sigma}, f^{\dagger}_{\mathbf{k},\sigma};\omega\right) = 1 + \Sigma_{\sigma}\left(\mathbf{k},\omega\right)G\left(f_{\mathbf{k},\sigma}, f^{\dagger}_{\mathbf{k},\sigma};\omega\right). \tag{2.14}$$

Therefore, the f-electron Green's function has the following closed form

$$G\left(f_{\mathbf{k},\sigma}, f^{\dagger}_{\mathbf{k},\sigma};\omega\right) = \frac{1}{\omega - \epsilon_0 - \frac{V^2}{\omega-\epsilon_{\mathbf{k}}} - \Sigma_{\sigma}\left(\mathbf{k},\omega\right)}. \tag{2.15}$$

Fourier transformation then yields the lattice Green's function:

$$G_{ij}(\omega) = \frac{1}{N}\sum_{\mathbf{k}} G\left(f_{\mathbf{k},\sigma}, f^{\dagger}_{\mathbf{k},\sigma};\omega\right) e^{i\mathbf{k}\cdot\left(\mathbf{R}_i-\mathbf{R}_j\right)}. \tag{2.16}$$

As in this thesis a significant part of the calculation is performed in the AFM state of a bipartite lattice, we will also illustrate how to build up the model for a state with long ranged AFM order, assuming that the self energy $\Sigma_\sigma\left(\mathbf{k},\omega\right)$ is local:

$$\Sigma_\sigma\left(\mathbf{k},\omega\right) = \Sigma_\sigma(\omega) \tag{2.17}$$

To generalize our case to AFM state in the frame work of DMFT, self energy is set to be site i dependent:

$$\Sigma_\sigma(\omega) = \Sigma_{i,\sigma}(\omega) \tag{2.18}$$

Next we introduce sublattice degrees of freedom α and map each lattice site i onto a sublattice α such that $\Sigma_{i,\sigma}(\omega) \to \Sigma_{\alpha,\sigma}(\omega)$.

In DMFT, non-local Green's functions are suppressed with respect to increasing coordination number Z; therefore, when $Z \to \infty$, only local Green's functions survive [68, 69] or only they contribute to free energy [77]. As a result, only local Green's functions will be considered and they are sublattice m and spin σ dependent:

$$G_{\alpha,\sigma}(\omega) = \frac{1}{N}\sum_{\mathbf{k}} G_\alpha\left(f_{\mathbf{k},\sigma}, f^{\dagger}_{\mathbf{k},\sigma};\omega\right) \tag{2.19}$$

2.1.2 Periodic Anderson Model on Bipartite Lattice

For a commensurate AFM system with sublattices A and B, we have the following property for the self-energy

$$\Sigma_{A,\sigma} = \Sigma_{B,\bar{\sigma}} \tag{2.20}$$

therefore we can express the self-energy as

$$\Sigma_{i\sigma}(\omega) = \Sigma_0(\omega) + \sigma e^{i\mathbf{Q}\cdot\mathbf{R}_i}\Sigma_m(\omega), \tag{2.21}$$

with $\Sigma_0(\omega)$ acting as a homogeneous "background" and Σ_m as an effective dynamic staggered magnetic field. Here we represent the Coulomb interaction directly in form of the self-energy and the local state Hamiltonian is

$$\begin{aligned} H_{loc} &= \sum_{i,\sigma}\left(\epsilon_0+\Sigma_{i,\sigma}\right) f^{\dagger}_{i,\sigma} f_{i,\sigma} \\ &= \sum_{i,\sigma}\left(\epsilon_0+\Sigma_0+\sigma\exp^{i\mathbf{Q}\cdot\mathbf{R}_i}\Sigma_m\right) f^{\dagger}_{i,\sigma} f_{i,\sigma} \\ &= \sum_{\mathbf{k},\sigma}\left[\left(\epsilon_0+\Sigma_0\right) f^{\dagger}_{\mathbf{k},\sigma} f_{\mathbf{k},\sigma} + \sigma\Sigma_m f^{\dagger}_{\mathbf{k},\sigma} f_{\mathbf{k}+\mathbf{Q},\sigma}\right] \end{aligned} \tag{2.22}$$

Due to the AFM wavevector $\mathbf{Q}$, we only need to consider the reduced Brillouin zone which is half the size of the original Brillouin zone and the region outside the Brillouin zone can be included by connecting the reduced Brillouin zone and wavevector $\mathbf{Q}$. Therefore the local Hamiltonian H_{loc} can be written as

$$\begin{aligned} H_{\mathrm{loc}} &= \sum_{\mathbf{k},\sigma}{}' \left[\left(\epsilon_0 + \Sigma_0\right) f^{\dagger}_{\mathbf{k},\sigma} f_{\mathbf{k},\sigma} + \left(\epsilon_0 + \Sigma_0\right) f^{\dagger}_{\mathbf{k}+\mathbf{Q},\sigma} f_{\mathbf{k}+\mathbf{Q},\sigma} \right] \\ &+ \sum_{\mathbf{k},\sigma}{}' \left[\sigma\Sigma_m f^{\dagger}_{\mathbf{k},\sigma} f_{\mathbf{k}+\mathbf{Q},\sigma} + \sigma\Sigma_m f^{\dagger}_{\mathbf{k}+\mathbf{Q},\sigma} f_{\mathbf{k},\sigma} \right], \end{aligned} \tag{2.23}$$

where $\sum'$ denotes summation over the reduced Brillouin zone. The corresponding matrix form of this Hamiltonian is

$$H_{\mathrm{loc}} = \sum_{\mathbf{k},\sigma}{}' \left(f^{\dagger}_{\mathbf{k},\sigma}, f^{\dagger}_{\mathbf{k}+\mathbf{Q},\sigma} \right) \begin{pmatrix} \epsilon_0 + \Sigma_0 & \sigma\Sigma_m \\ \sigma\Sigma_m & \epsilon_0 + \Sigma_0 \end{pmatrix} \begin{pmatrix} f_{\mathbf{k},\sigma} \\ f_{\mathbf{k}+\mathbf{Q},\sigma} \end{pmatrix}. \tag{2.24}$$

Next we consider the conduction band and its hybridization with the 4f-states:

$$H_{\mathrm{c}} = \sum_{\mathbf{k},\sigma}{}' \left(c^{\dagger}_{\mathbf{k},\sigma}, c^{\dagger}_{\mathbf{k}+\mathbf{Q},\sigma} \right) \begin{pmatrix} \epsilon_{\mathbf{k}} & 0 \\ 0 & \epsilon_{\mathbf{k}+\mathbf{Q}} \end{pmatrix} \begin{pmatrix} c_{\mathbf{k},\sigma} \\ c_{\mathbf{k}+\mathbf{Q},\sigma} \end{pmatrix} \tag{2.25}$$

$$H_{\mathrm{hyb}} = V \sum_{\mathbf{k},\sigma}{}' \left(c^{\dagger}_{\mathbf{k},\sigma} f_{\mathbf{k},\sigma} + f^{\dagger}_{\mathbf{k},\sigma} c_{\mathbf{k},\sigma} + c^{\dagger}_{\mathbf{k}+\mathbf{Q},\sigma} f_{\mathbf{k}+\mathbf{Q},\sigma} + f^{\dagger}_{\mathbf{k}+\mathbf{Q},\sigma} c_{\mathbf{k}+\mathbf{Q},\sigma} \right). \tag{2.26}$$

If we integrate out the conduction band degree of freedom [67], we obtain for the inverse Green's function:

$$G^{-1}_{\sigma}\left(\mathbf{k},\omega\right) = \begin{pmatrix} \omega - \epsilon_0 - \Sigma_0 - \frac{V^2}{\omega - \epsilon_{\mathbf{k}}} & -\sigma\Sigma_m \\ -\sigma\Sigma_m & \omega - \epsilon_0 - \Sigma_0 - \frac{V^2}{\omega - \epsilon_{\mathbf{k}}} \end{pmatrix} \tag{2.27}$$

The basis $\left(f^{\dagger}_{\mathbf{k},\sigma}, f^{\dagger}_{\mathbf{k}+\mathbf{Q},\sigma} \right)$ is convenient for studying antiferromagnetic order and SDW. However, it is not the right basis to use the NRG because the calculation is performed on a single site. Therefore we use a unitary transformation to rotate the basis via

$$\begin{pmatrix} f_{\mathbf{k},\sigma} \\ f_{\mathbf{k}+\mathbf{Q},\sigma} \end{pmatrix} = \frac{1}{\sqrt{2}} \begin{pmatrix} 1 & -1 \\ 1 & 1 \end{pmatrix} \begin{pmatrix} f_{A,\mathbf{k},\sigma} \\ f_{B,\mathbf{k},\sigma} \end{pmatrix} \tag{2.28}$$

and

$$G^{-1}_{\sigma}\left(\mathbf{k},\omega\right) = \begin{pmatrix} \omega - \epsilon_0 - \Sigma_0 - \sigma\Sigma_m - \frac{V^2}{\omega - \epsilon_{\mathbf{k}}} & 0 \\ 0 & \omega - \epsilon_0 - \Sigma_0 + \sigma\Sigma_m - \frac{V^2}{\omega - \epsilon_{\mathbf{k}}} \end{pmatrix} \tag{2.29}$$

The local Green's function is then given as:

$$G_{\sigma}\left(\omega\right) = \sum_{\mathbf{k}}{}' G_{\sigma}\left(\mathbf{k},\omega\right). \tag{2.30}$$

2.1.3 Single Impurity Anderson Model

Next we consider the single impurity Anderson model. Since momentum is not conserved in the SIAM, we have to modify our analysis. We define

$$\begin{aligned} c^\dagger_{i,\sigma} &= \sum_l a^*_{il,\sigma} c^\dagger_{l,\sigma} \\ c_{i,\sigma} &= \sum_l a_{il,\sigma} c_{l,\sigma}, \end{aligned} \tag{2.31}$$

where l is an additional single particle index and $a_{il,\sigma}$ and $a^*_{il,\sigma}$ are elements of the matrix A which can diagonalizes the hopping matrix T:

$$\left(A^\dagger T A\right)_{ij} = \epsilon_i \delta_{ij} \tag{2.32}$$

If we insert this representation into the Hamiltonian Eq.(2.7) of the SIAM, we obtain

$$\begin{aligned} H_{SIAM} &= \sum_\sigma \epsilon_0 f^\dagger_\sigma f_\sigma + U n^f_\uparrow n^f_\downarrow + \sum_\sigma \sum_l V \left(a_{0l,\sigma} f^\dagger_\sigma c_{l,\sigma} + a^*_{0l,\sigma} c^\dagger_{l,\sigma} f_\sigma \right) \\ &\quad + \sum_\sigma \sum_l \epsilon_l c^\dagger_{l,\sigma} c_{l,\sigma}, \end{aligned} \tag{2.33}$$

with

$$\sum_{i,j} a^\dagger_{il,\sigma} t_{ij} a_{jk,\sigma} = \epsilon_l \delta_{lk}, \tag{2.34}$$

as follows from Eq.(2.32). If we define $V_{l,\sigma} = V a_{0l,\sigma}$ and $V^*_{l,\sigma} = V a^*_{0l,\sigma}$, we arrive at

$$\begin{aligned} H_{SIAM} &= \sum_\sigma \epsilon_0 f^\dagger_\sigma f_\sigma + U n^f_\uparrow n^f_\downarrow + \sum_\sigma \sum_l \epsilon_l c^\dagger_{l,\sigma} c_{l,\sigma} \\ &+ \sum_\sigma \sum_l \left(V_{l,\sigma} f^\dagger_\sigma c_{l,\sigma} + V^*_{l,\sigma} c^\dagger_{l,\sigma} f_\sigma \right) \end{aligned} \tag{2.35}$$

With this form, we can perform a similar calculation as for the PAM and obtain the SIAM Green's function:

$$G_\sigma(\omega) = \frac{1}{\omega - \epsilon_0 - \sum_l \frac{\left|V_{l,\sigma}\right|^2}{\omega - \epsilon_l} - \Sigma_\sigma(\omega)} \tag{2.36}$$

which is a local quantity.

The main reason why we go through these two limits is that we need Eq.(2.19) and Eq.(2.36) in the next chapter to build up a self-consistent algorithm for solving our impurity problem.

Chapter 3
3 Methods

In this chapter, we will show how to apply DMFT, NRG, and CPA to solve dilute lattice problems self-consistently. It can be shown that the result of dilute system is consistent with that of clean system when there is no impurity doping; while for high doping concentration, a dilute system can be effectively described as a single impurity problem in section 3.2. A brief summary on the NRG algorithm will also be given in section 3.3. The algorithms will be summarized in three flow diagrams, corresponding to PM state, AFM state with/without staggered magnetic field, and AFM state with uniform magnetic field in section 3.4.

3.1 Dynamical Mean Field Theory: Clean System

In the end of chapter 1, we showed that in the framework of DMFT, a lattice system can be mapped onto a single impurity problem characterized by Weiss mean field $G_0^{-1}(\omega)$ and on-site Coulomb interaction U. As a result, we have the local action S_{loc}:

$$\begin{aligned} S_{loc} &= \int d\tau d\tau' \sum_{\sigma} f_{\sigma}^{\dagger}(\tau) \left[G_0^{-1}\left(\tau - \tau'\right) \right] f_{\sigma}\left(\tau'\right) \\ &\quad + \int d\tau U_l n_{\uparrow}^{f}(\tau) n_{\downarrow}^{f}(\tau), \end{aligned} \tag{3.1}$$

where the Weise mean field contains the local energy level ϵ_0 and the hybridization function $\Gamma(\omega)$ which decribes the coupling between this impurity site and its environment. Here l and σ denote the lattice site and the spin, respectively. Therefore, G_0 effectively represents the non-interacting Hamiltonian

$$H_0 = \sum_{\sigma} \epsilon_0 f_{\sigma}^{\dagger} f_{\sigma} + \sum_{l,\sigma} \left(V_l f_{\sigma}^{\dagger} c_{l,\sigma} + V_l^{*} c_{l,\sigma}^{\dagger} f_{\sigma} \right) + \sum_{l,\sigma} \epsilon_l c_{l,\sigma}^{\dagger} c_{l,\sigma} \tag{3.2}$$

with $c_{l,\sigma}^{\dagger}\left(c_{l,\sigma}\right)$ the creation (annihilation) operator of an auxiliary field with quantum number l, ϵ_l the auxiliary field dispersion relation, and V_l the effective interaction between local site and auxiliary field. We see that together with the Coulomb interaction U, Eq.(3.1) is the single impurity Anderson model shown in the last chapter. Therefore, this problem can be solved by a impurity solver such as NRG [36]. Since V_l and ϵ_l are not known in advance, they will be determined self-consistently.

For a given Weiss mean field $G_0^{-1}(\omega)$ and Coulomb interaction U, the full impurity Green's function G_{imp} and impurity self-energy Σ_{imp} can be obtained by NRG [81]. The lattice Green's function G_{lat} can also be obtained. Then from the DMFT self-consistent equation, we have to compare G_0^{-1} and $G_{lat}+\Sigma_{imp}$. If they are not equal then a new Weiss field is chosen to perform the next calculation. This process continues until the difference between old and new Weiss fields is sufficiently small.

3.2 Dynamic Mean Field Theory: Dilute System

In a dilute system with different constituents, the local action depends on the site l:

$$\begin{aligned} S_{loc}(l) &= \int d\tau d\tau' \sum_{\sigma} f_{\sigma}(\tau) \left[G_0^{-1}\left(\tau-\tau'\right) + \epsilon_l \delta\left(\tau-\tau'\right)\right] f_{\sigma}\left(\tau'\right) \\ &\quad + \int d\tau U_l n_{\uparrow}^{f}(\tau) n_{\downarrow}^{f}(\tau). \end{aligned} \tag{3.3}$$

In our study on $Ce_{1-x}La_xCu_2Ge_2$, we showed in the last chapter there are two possible choices for $S_{loc}(l)$ and each of them corresponds to a Green's function

$$G(\omega; l) = \begin{cases} G(\epsilon_0, U; \omega) & , \text{ if } l \in \text{Ce} \\ G(\infty, 0; \omega) & , \text{ if } l \in \text{La}. \end{cases} \tag{3.4}$$

Next we apply CPA which approximates the Green's function of the system as the average of the Green's functions of these two sites:

$$\begin{aligned} \bar{G} &= x G(\epsilon_0, U; \omega) + (1-x) G(\infty, 0; \omega) \\ &= \frac{x}{G_0^{-1} - \epsilon_0 - \Sigma(\epsilon_0, U; \omega)} \end{aligned} \tag{3.5}$$

and the CPA self-consistency condition gives

$$\bar{G} = \sum_{\mathbf{k}} \frac{1}{\omega - \bar{\Sigma}(\omega) - \frac{V^2}{\omega - \epsilon_{\mathbf{k}}}}, \tag{3.6}$$

where $\bar{\Sigma}$ is the averaged self-energy which includes both Coulomb interaction and disorder. To obtain $\bar{\Sigma}$, we expressed the averaged Green's function as

$$\bar{G}(\omega) = \frac{1}{G_0^{-1} - \bar{\Sigma}}. \tag{3.7}$$

As a result, the averaged self-energy can be obtained by solving Eq.(3.5) and Eq.(3.7):

$$\bar{\Sigma} = \Sigma_{imp}(\omega) + \epsilon_0 + \left(1 - \frac{1}{x}\right) G_{imp}^{-1}(\omega). \tag{3.8}$$

Next we discuss DMFT + CPA in two limit of the PM case: perfect lattice $x \to 1$ and dilute limit $x \to 0$. The extension to an AFM state can be done straightforwardly by taking sublattice and spin dependences into account.

3.2.1 Perfect Lattice

In this limit, $x \to 1$ and

$$\begin{aligned} \lim_{x\to 1} \bar{G} &= \lim_{x\to 1} \frac{x}{G_0^{-1} - \epsilon_0 - \Sigma\left(\epsilon_0, U; \omega\right)} \\ &= \frac{1}{G_0^{-1} - \epsilon_0 - \Sigma\left(\epsilon_0, U; \omega\right)} \end{aligned} \tag{3.9}$$

and

$$\begin{aligned} \lim_{x\to 1} \bar{\Sigma} &= \lim_{x\to 1} \left(\Sigma_{imp}\left(\omega\right) + \epsilon_0 + \left(1 - \frac{1}{x}\right) G_{imp}^{-1}\left(\omega\right) \right) \\ &= \Sigma_{imp}\left(\omega\right) + \epsilon_0 \end{aligned} \tag{3.10}$$

such that

$$G_{CPA} = \sum_{\mathbf{k}} \frac{1}{\omega - \epsilon_0 - \Sigma_{imp}\left(\omega\right) - \frac{V^2}{\omega - \epsilon_{\mathbf{k}}}} \tag{3.11}$$

which is the result of PAM.

3.2.2 Dilute Limit

In this limit, $x \to 0$. As in the previous chapter it was mentioned that an effective SIAM can be derived from the Anderson lattice model. In this section I will show how to achieve it within a self-consistent calculation.

From Eq.(3.8) we obtain

$$\bar{G} = \frac{1 - x}{\Sigma_{imp} + \epsilon_0 - \bar{\Sigma}}. \tag{3.12}$$

In this limit, to make sure that $\bar{G} \to 0$, $\bar{\Sigma} \propto \frac{1}{x}$ in the leading order which can be seen from Eq.(3.8). On the other hand from Eq. (3.6) we have

$$G_{CPA} = \sum_{\mathbf{k}} \frac{1}{\omega - \bar{\Sigma}\left(\omega\right) - \frac{V^2}{\omega - \epsilon_{\mathbf{k}}}}. \tag{3.13}$$

Due to self-consistent condition, it is required that $\bar{G} = G_{CPA}$:

$$\frac{1 - x}{\Sigma_{imp} + \epsilon_0 - \bar{\Sigma}} = \sum_{\mathbf{k}} \frac{1}{\omega - \bar{\Sigma}\left(\omega\right) - \frac{V^2}{\omega - \epsilon_{\mathbf{k}}}}. \tag{3.14}$$

The doping concentration x can be used as a control parameter for a Taylor expansion. We make the ansatz that $\bar{\Sigma}$ has the following form:

$$\bar{\Sigma} \sim \frac{\sigma_{-1}}{x} + \sigma_0 + x\sigma_1 + O\left(x^2\right). \tag{3.15}$$

It can be shown that terms like $\frac{\sigma_{-\alpha}}{x^\alpha}$ with positive α are zero except for $\alpha = 1$ by expanding $\bar{G}$ and G_{CPA} with respect to small x and comparing the coefficients. To make sure nothing is left behind in

the calculation, we include the third order term in the Taylor expansion in Eq.(3.15). If both averaged Green's functions in Eq.(3.14) are expanded, we will obtain σ_{-1} in this form and σ_0 as:

$$\sigma_{-1} = \left(\Sigma_{imp} + \epsilon_0 - \omega - \sum_k F_k\right), \tag{3.16}$$

$$\sigma_0 = \left(\omega + \sum_k F_k\right) + \frac{1}{\sigma_{-1}}\left[\left(\sum_k F_k\right)^2 - \sum_k F_k^2\right] \tag{3.17}$$

with

$$F_k = -\frac{V^2}{\omega - \epsilon_k}. \tag{3.18}$$

If we consider the averaged self-energy in the first leading order, we combine Eq.(3.8), Eq.(3.15) and Eq.(3.16) to obtain:

$$G_{imp}(\omega) = \frac{1}{\omega - \epsilon_0 - \Sigma_{imp}(\omega) - \sum_k \frac{V^2}{\omega - \epsilon_k}}, \tag{3.19}$$

which happens to be in the form of SIAM Green's function.

Suppose bare Green's function G_0 has the following form

$$G_0 = \frac{1}{\omega + \Gamma} \tag{3.20}$$

with Γ taking into account the medium and having to be determined self-consistently, then Eq.(3.5) gives

$$\bar{G} = \frac{x}{\omega - \epsilon_0 - \Sigma_{imp}(\omega) + \Gamma} \tag{3.21}$$

while Eq.(3.12) gives

$$\bar{G} = \frac{x}{\omega - \epsilon_0 - \Sigma_{imp}(\omega) - \sum_k \frac{V^2}{\omega - \epsilon_k}}. \tag{3.22}$$

This implies that $\Gamma = -\sum_k \frac{V^2}{\omega - \epsilon_k}$ and there is no correction with respect to the impurity concentration, which happens to be the case of SIAM or the so-called atomic limit. If we are in the small x limit and we want to take the effect of an impurity into account, we need to include σ_0 shown in Eq.(3.17) in the averaged self-energy and Γ has the following self-consistent form

$$\Gamma = \sum_k F_k - \frac{x}{(1-x)\,\sigma_{-1}}\left[\left(\sum_k F_k\right)^2 - \sum_k F_k^2\right]. \tag{3.23}$$

The next question is how do we determine the Green's function and the self energy to solve our problem if Γ is not known in advance? To calculate the Green's function we use the impurity solver NRG we introduced in Chapter 1. In the next section it will be illustrated how it works in PM state. The AFM state in the calculation is equivalent to the calculation in the PM state with magnetic field. As a result, the algorithm remains the same except that spin degrees of freedom are included.

3.3 Numerical Renormalization Group

In DMFT which maps a lattice problem onto a single impurity problem, we start from the SIAM Hamiltonian [80]:

$$\begin{aligned} H &= \sum_{\sigma} \epsilon_0 f_{\sigma}^{\dagger} f_{\sigma} + U n_{\uparrow}^{f} n_{\downarrow}^{f} + \sum_{l\sigma} \epsilon_l c_{l,\sigma}^{\dagger} c_{l,\sigma} \\ &\quad + \sum_{l\sigma} \left(V_l f_{\sigma}^{\dagger} c_{l,\sigma} + V_l^{*} c_{l,\sigma}^{\dagger} f_{\sigma} \right). \end{aligned} \tag{3.24}$$

Next we map Eq.(3.24) which contains all different modes labelled by l into a 1-D Hamiltonian:

$$\begin{aligned} H_{1-D} &= \sum_{\sigma} \epsilon_0 f_{\sigma}^{\dagger} f_{\sigma} + U n_{\uparrow}^{f} n_{\downarrow}^{f} + \sum_{\sigma} \int_{-1}^{1} d\epsilon g_{\sigma}(\epsilon) a_{\epsilon,\sigma}^{\dagger} a_{\epsilon,\sigma} \\ &\quad + \sum_{\sigma} \int_{-1}^{1} d\epsilon h_{\sigma}(\epsilon) \left(f_{\sigma}^{\dagger} a_{\epsilon,\sigma} + a_{\epsilon,\sigma}^{\dagger} f_{\sigma} \right). \end{aligned} \tag{3.25}$$

From Eq.(3.25), we can define the hybridization function $\Gamma_{\sigma}(\omega)$, which describes the strength of coupling by integrating out the auxiliary field $c_{k,\sigma}$ (Hubbard-Stratonovich transformation) and taking the imaginary part:

$$\begin{aligned} \Gamma_{\sigma}(\omega) &= -\Im \left(\sum_{k} \frac{V_{k,\sigma}^{2}}{\omega - \epsilon_k + i\delta} \right) \\ &= \pi V_{\omega,\sigma}^{2} \rho_0(\omega). \end{aligned} \tag{3.26}$$

Since Eq.(3.24) and Eq.(3.25) are equivalent, their resulting hybrization function should also be equal; therefore the relation between the hybridization function $\Gamma_{\sigma}(\omega)$, the dispersion relation $g_{\sigma}(\epsilon)$, and the impurity-fermionic bath interaction $h_{\sigma}(\epsilon)$ can be written as

$$\Gamma_{\sigma}(\omega) = \pi \frac{d\epsilon(\omega)}{d\omega} \left[h\left(\epsilon(\omega)\right) \right]^{2}, \tag{3.27}$$

which can be obtained by integrating out all the $a_{\epsilon,\sigma}$ modes via Hubbard-Stratonovich transformation. From Eq.(3.27) we see the combination of $g(\epsilon)$ and $h(\epsilon)$ is not unique. One choice is $\left\{ g(\epsilon), h(\epsilon) \right\} = \left\{ \epsilon, V_{\epsilon} \sqrt{\rho(\epsilon)} \right\}$ which can be obtained by transforming plane wave particles into spherical wave particles [36]. However, we can choose other combinations of $g(\epsilon)$ and $h(\epsilon)$ to make our calculation easier which will be introduced in the next section.

3.3.1 Logarithmic Discretization

Similar to the Fourier series in which a function is transformed into the linear combination of various modes characterized by some integers, we transform all the modes a_{ϵ} and $a_{\epsilon}^{\dagger}$ into the linear combinations

of modes $\psi^{\dagger}_{n,l}$ and $\psi_{n,l}$ characterized by two integers n and l which can be considers as principle quantum number and azimuthal quantum number, respectively:

$$\begin{aligned}\psi^{+}_{nl} &= \frac{1}{\sqrt{d_n}} e^{i\omega_n l\epsilon} \text{ for } \Lambda^{-n-1} < \epsilon < \Lambda^{-n}, \\ \psi^{-}_{nl} &= \frac{1}{\sqrt{d_n}} e^{-i\omega_n l\epsilon} \text{ for } -\Lambda^{-n} < \epsilon < -\Lambda^{-n-1},\end{aligned} \tag{3.28}$$

with Λ the discretization parameter whose value is chosen between 1 and 10 in practice , and

$$d_n = \Lambda^{-n}\left(1 - \Lambda^{-1}\right), \tag{3.29}$$

$$\omega_n = \frac{2\pi}{d_n}. \tag{3.30}$$

We expand the operator $a_{\epsilon\sigma}$ in this basis:

$$a_{\epsilon\sigma} = \sum_{nl}\left(a_{nl\sigma}\psi^{+}_{nl}(\epsilon) + b_{nl\sigma}\psi^{-}_{nl}(\epsilon)\right), \tag{3.31}$$

with inverse transformation:

$$\begin{aligned}a_{nl\sigma} &= \int_{-1}^{1} d\epsilon \left(\psi^{+}_{nl}(\epsilon)\right)^{*} a_{\epsilon\sigma}, \\ b_{nl\sigma} &= \int_{-1}^{1} d\epsilon \left(\psi^{-}_{nl}(\epsilon)\right)^{*} a_{\epsilon\sigma}.\end{aligned} \tag{3.32}$$

It can be shown in Ref.[15] that by keeping only the $l = 0$ terms and relabelling $a_{n\sigma} = a_{n0\sigma}$ as well as $b_{n\sigma} = b_{n0\sigma}$, the approximation for the Hamiltonian Eq.(3.25) is

$$\begin{aligned}H &= \sum_{\sigma}\epsilon_0 f^{\dagger}_{\sigma} f_{\sigma} + U n^{f}_{\uparrow} n^{f}_{\downarrow} + \sum_{n\sigma}\left(\xi^{+}_{n} a^{\dagger}_{n\sigma} a_{n\sigma} + \xi^{-}_{n} b_{n\sigma} b_{n\sigma}\right) \\ &\quad + \frac{1}{\sqrt{\pi}}\sum_{\sigma n} f^{\dagger}_{\sigma}\left(\gamma^{+}_{n} a_{n\sigma} + \gamma^{-}_{n} b_{n\sigma}\right) + \frac{1}{\sqrt{\pi}}\sum_{\sigma n}\left(\gamma^{+}_{n} a^{\dagger}_{n\sigma} + \gamma^{-}_{n} b^{\dagger}_{n\sigma}\right) f_{\sigma}.\end{aligned} \tag{3.33}$$

In a real calculation, this single discretization scheme might introduce some artificial oscillations into the thermodynamic expectation values. One way to remove these artificial effects is by using z-averaging proposed in Ref.[14]. N_z different discretization meshes are set up and the average over several calculations for different z is used. An example with $N_z = 4$ is shown in Fig.(3.1). Further improvement in dynamical quantities is done by Zitko and Pruschke [82, 83].

As can be seen from Eq.(3.33), the impurity couples to all the modes and direct diagonalization is not realistic due to the enormous size of the corresponding matrix, extra treatment is required to make the calculation manageable and to achieve the desired low energy scale.

3.3.2 Tridiagonalization

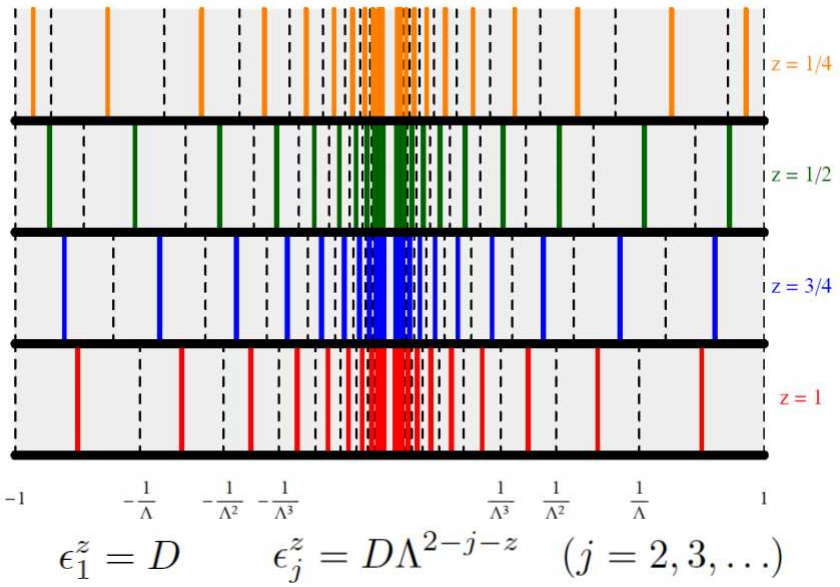

Figure 3.1: *Z-averaging by discretizing hybridization function* $\Gamma(\omega)$ *with different meshes[13, 14]. This figure represents z-averaging with* $N_z = 4$ *such that* $z \in \left\{\frac{1}{4}, \frac{2}{4}, \frac{3}{4}, 1\right\}$. *NRG calculation runs through different discretization meshes corresponding to different zs. In the end the obtained results, such as spectral function and particle occupation number, will be averaged.*

Eq.(3.33) is rotated such that the Hamiltonian corresponds to a semi-infinite chain whose Hamiltonian looks like that of a tight-binding model. From the hybridization term of Eq.(3.33), we define an operator on the zeroth site which couples directly to the impurity site as :

$$c_{0\sigma} = \frac{1}{\sqrt{\xi_0}} \sum_{n=0}^{\infty} \left(\gamma_n^+ a_{n\sigma} + \gamma_n^- b_{n\sigma}\right) \tag{3.34}$$

with fermionic commutation relation $\left[c_{0\sigma}, c_{0\sigma}^\dagger\right]_+ = 1$ and normalization factor:

$$\xi_0 = \sum_{n=0}^{\infty} \left(\gamma_n^{+2} + \gamma_n^{-2}\right). \tag{3.35}$$

Then from the impurity site, Schmidt orthgonalization is applied to construct a new set of mutually orthogonal operators $c_{n,\sigma}^\dagger$ and $c_{n,\sigma}$ such that a semi-infinite chain Hamiltonian can be obtained [15, 36]

$$\begin{aligned} H &= \sum_\sigma \epsilon_0 f_\sigma^\dagger f_\sigma + U n_\uparrow^f n_\downarrow^f + \sqrt{\frac{\xi_0}{\pi}} \sum_\sigma \left(f_\sigma^\dagger c_{0,\sigma} + c_{0,\sigma}^\dagger f_\sigma\right) \\ &+ \sum_{\sigma,n=0} \left[\epsilon_n c_{n,\sigma}^\dagger c_{n,\sigma} + t_n \left(c_{n\sigma}^\dagger c_{n+1,\sigma} + c_{n+1,\sigma}^\dagger c_{n\sigma}\right)\right] \end{aligned} \tag{3.36}$$

in which ϵ_n and t_n act as onsite energy and hopping between two sites, respectively. The energy scales of ϵ_n and t_n decrease with respect to increasing site number n as Λ^{-n} and $\Lambda^{-\frac{n}{2}}$ for sufficiently large

n [15], respectively. In a realistic calculation, n must be terminated at some point. The lowest energy scale decreases by $\Lambda^{-\frac{1}{2}}$ by including one extra site into the chain, hence the coupling between the old chain and the new site can be thought of as an interaction with strength $O\left(\Lambda^{-\frac{1}{2}}\right)$ if the lowest energy scale of the old chain is $O(1)$. Due to $\Lambda > 1$, the coupling can be treated as a perturbation and this is the reason why Eq.(3.36) can be diagonalized iteratively.

3.3.3 Iterative Diagonalization

The idea of iterative diagonalization is simple: we start from a given Hamiltonian H_N, diagonalize it such that it becomes $H_N^{(diag)}$, then connect a new site to the diagonalized Hamiltonian $H_N^{(diag)}$. The interactions between the new site and $H_N^{(diag)}$ will be determined recursively. This procedure keeps going until we decide to stop the calculation.

In the beginning of the calculation, an initial Hamiltonian, representing the impurity site plus the zeroth site, is chosen. It can be written as the first three terms of Eq.(3.36). It is then rescaled by the discretization parameter $\Lambda^{-\frac{1}{2}}$:

$$\begin{aligned} H_0 &= \Lambda^{-\frac{1}{2}}\left(\sum_\sigma \epsilon_0 f_\sigma^\dagger f_\sigma + U n_\uparrow^f n_\downarrow^f + \sum_\sigma \epsilon_0 c_{0,\sigma}^\dagger c_{0,\sigma}\right. \\ &\quad \left. + \sqrt{\frac{\xi_0}{\pi}}\sum_\sigma\left(f_\sigma^\dagger c_{0,\sigma} + c_{0,\sigma}^\dagger f_\sigma\right)\right) \end{aligned} \tag{3.37}$$

and the recursion relation is

$$\begin{aligned} H_{N+1} &= \Lambda^{\frac{1}{2}} H_N + \Lambda^{\frac{N}{2}}\sum_\sigma \epsilon_{N+1} c_{N+1,\sigma}^\dagger c_{N+1,\sigma} \\ &\quad + \Lambda^{\frac{N}{2}}\sum_\sigma t_N\left(c_{N,\sigma}^\dagger c_{N+1,\sigma} + c_{N+1,\sigma}^\dagger c_{N,\sigma}\right). \end{aligned} \tag{3.38}$$

The factor $\Lambda^{\frac{N}{2}}$ in Eq.(3.38) has been chosen to cancel the N dependence of t_N and the perturbation is of $O(1)$ while the lowest energy scale of $\Lambda^{\frac{1}{2}} H_N$ is of $O(\Lambda)$. In each step N, H_N is diagonalized and has a set of eigenstates $\left\{|r\rangle_N\right\}$. By adding a new site to build H_{N+1}, each of the eigenstates $|r\rangle_N$ is connected to four other states: $\left\{|0\rangle_{N+1}, |\uparrow\rangle_{N+1}, |\downarrow\rangle_{N+1}, |\uparrow\downarrow\rangle_{N+1}\right\}$.

To the Nth site, a matrix with Hilbert space of size 4^{N+2} can be expected. For example, $N = 60$, this are 2.12×10^{37} eigenstates and it is not possible to perform the task numerically. To overcome this problem, truncation is introduced which only keeps the energetically lowest N_{kept} states and connects them with the next site. Generally speaking, the higher the N_{kept} the more accurate the information about the system we have. However, there is a trade off between accuracy and efficiency as the computational time for diagonalization scales as $O\left(N_{kept}^3\right)$. With some modern day techniques such as complete Fock space (CFS) [84, 85] which take the interactions between high energy modes (those discarded) and low energy modes (those kept) into account. Results such as spectral functions and thermodynamical quantities with different temperatures and magnetic fields with N_{kept} as small as 50

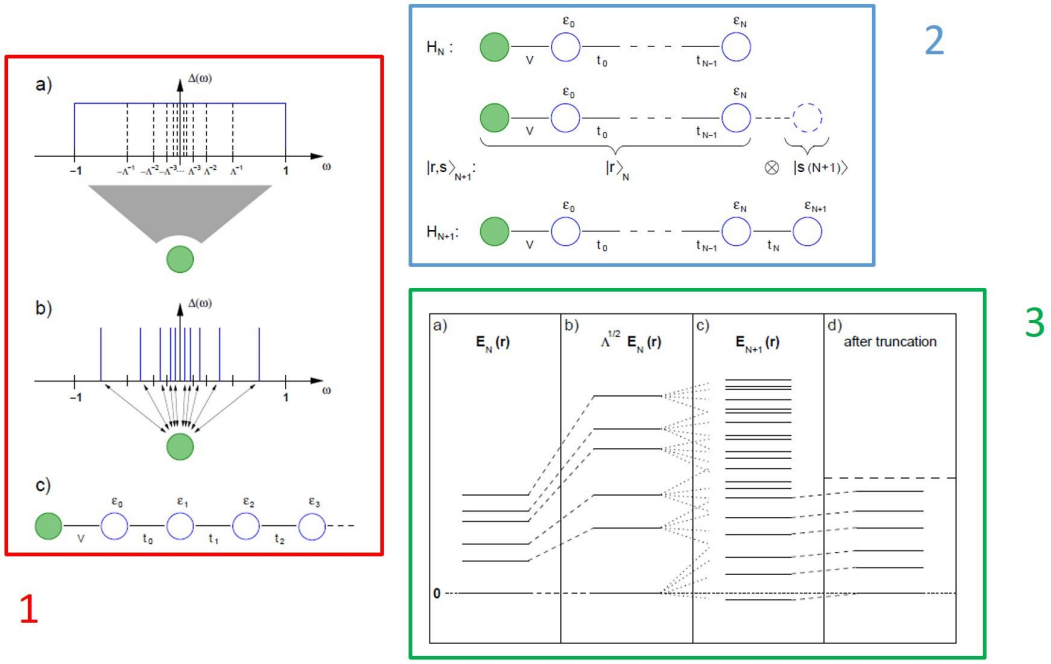

Figure 3.2: *NRG workflow [15]. First a SIAM is transformed into a semi-infinite tight binding model by logarithmic diagonalization and tridiagonalization (1). Then the tight-binding Hamiltonian is diagonalized iteratively and new sites connecting to the diagonalized Hamiltonian play the role of perturbations (2). After each diagonalization, low lying energy states will be kept and high energy states will be discarded (3).*

agree well with those with $N_{kept} = 500$. In the following calculation, N_{kept} is chosen between 500 and 1000 and the details are left to Ljubljana NRG.

Here we summarize how NRG works. First a SIAM is transformed into a semi-infinite tight binding model by logarithmic diagonalization and tridiagonalization. Secend the tight-binding Hamiltonian is diagonalized iteratively and new sites connecting to the diagonalized Hamiltonian play the role of perturbations. After each diagonalization, low lying energy states will be kept and high energy states will be discarded. Fig.(3.2) shows how NRG works diagramatically [15].

3.4 Self-Consistent Algorithm

In this section we summarize how dilute lattice problems are solved self-consistently in the framework of NRG + DMFT + CPA in three different cases: PM state, AFM state with/without staggered magnetic field, and AFM state with uniform magnetic field. The corresponding algorithm flow diagrams will also be shown.

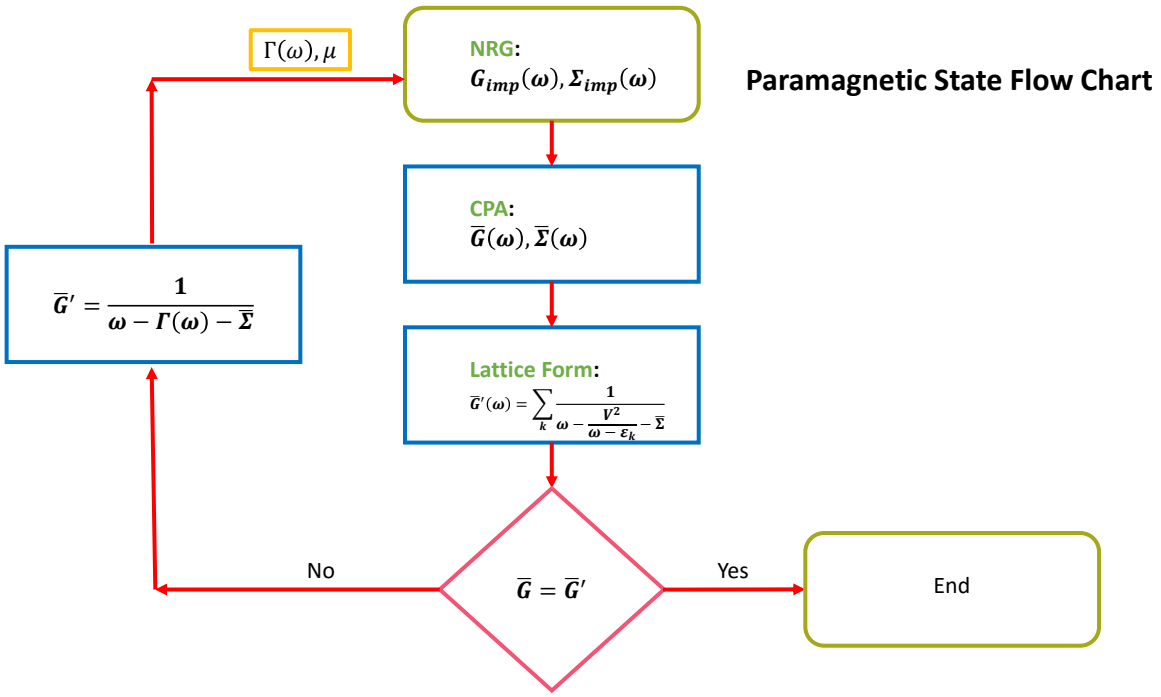

Figure 3.3: *Flow diagram of the NRG + DMFT + CPA self-consistent calculation in the PM state. The calculation starts with NRG to obtain the impurity Green's function $G_{imp}(\omega)$ and the impurity self-energy $\Sigma_{imp}(\omega)$. Then CPA is applied to obtain the averaged Green's function $\bar{G}(\omega)$ and the averaged self-energy $\bar{\Sigma}(\omega)$. With the averaged self energy $\bar{\Sigma}(\omega)$, the averaged Green's function $\bar{G}'(\omega)$in the lattice form is calculated. Next $\bar{G}(\omega)$ and $\bar{G}'(\omega)$ are compared. If they are sufficiently close to each other, the calculation converges. Otherwise, a new hybridization function $\Gamma(\omega)$ is constructed and a new chemical potential μ is obtained to be used in NRG in the next calculation.*

3.4.1 Paramagnetic State

The calculation starts with NRG to obtain the impurity Green's function $G_{imp}(\omega)$ and the impurity self energy $\Sigma_{imp}(\omega)$. Then CPA is applied to obtain the averaged Green's function $\bar{G}(\omega)$ and the averaged self-energy $\bar{\Sigma}(\omega)$. With the averaged self-energy $\bar{\Sigma}(\omega)$, the averaged Green's function $\bar{G}'(\omega)$ in the lattice form is calculated. Next $\bar{G}(\omega)$ and $\bar{G}'(\omega)$ are compared. If they are sufficiently close to each other, the calculation converges. Otherwise, a new hybridization function $\Gamma(\omega)$ is constructed and the chemical potential μ is obtained to be used in NRG in the next calculation. Here the self-consistent algorithms is shown in Fig.(3.3).

3.4.2 Antiferromagnetic State with/without Staggered Magnetic Field

Because of the symmetry of AFM state $G_{A,\sigma}(\omega) = G_{B,\bar{\sigma}}(\omega)$, sublattice dependence can be ignored

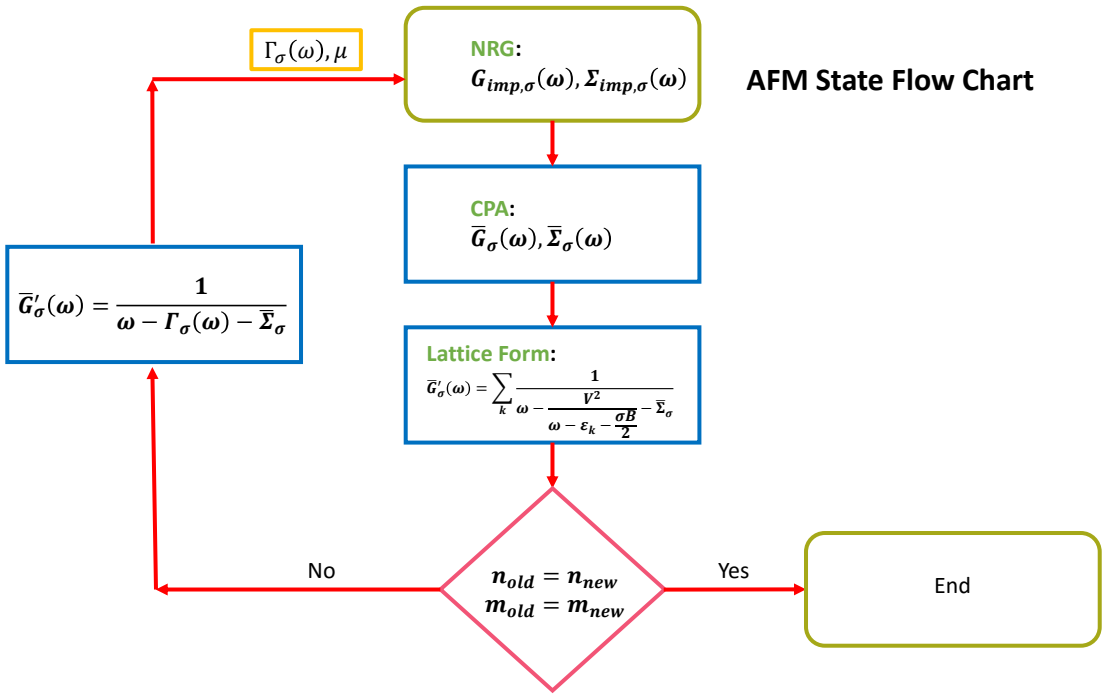

Figure 3.4: *Flow diagram of NRG + DMFT + CPA self-consistent calculation in the AFM state subjected to a staggered magnetic field. The calculation starts with NRG to obtain the spin dependent impurity Green's functions $G_{imp,\sigma}(\omega)$ and the impurity self-energies $\Sigma_{imp,\sigma}(\omega)$. Then CPA is applied to obtain the average Green's functions $\bar{G}_\sigma(\omega)$ and the averaged self-energies $\bar{\Sigma}_\sigma(\omega)$. With the averaged self-energies $\bar{\Sigma}_\sigma(\omega)$, the averaged Green's functions $\bar{G}'_\sigma(\omega)$ in the lattice form are calculated. The magnetizations and the carrier densities per site from two consecutive calculations are compared. If they are sufficiently close to each other, the calculation converges. Otherwise, two new spin dependent hybridization functions $\Gamma_\sigma(\omega)$ are constructed and a new chemical potential μ is obtained to be used in NRG in the next calculation.*

and only spin dependence is considered. The calculation starts with NRG to obtain spin dependent impurity Green's functions $G_{imp,\sigma}(\omega)$ and impurity self-energies $\Sigma_{imp,\sigma}(\omega)$. Then CPA is applied to obtain average Green's functions $\bar{G}_\sigma(\omega)$ and averaged self-energies $\bar{\Sigma}_\sigma(\omega)$. With averaged self-energies $\bar{\Sigma}_\sigma(\omega)$, averaged Green's functions $\bar{G}'_\sigma(\omega)$ in the lattice form are calculated. In contrast to comparing $\bar{G}_\sigma(\omega)$ and $\bar{G}'_\sigma(\omega)$, the magnetizations and carrier densities per site from two consecutive calculations are compared. If they are sufficiently close to each other, the calculation converges. Otherwise, two new spin dependent hybridization functions $\Gamma_\sigma(\omega)$ are constructed and a new chemical potential μ is obtained to be used in NRG in the next calculation. Here the self-consistent algorithms is shown in Fig.(3.4).

3.4.3 Antiferromagnetic State with Uniform Magnetic Field

Under uniform magnetic field, the sublattice degeneracy due to AFM symmetry is lifted. Then

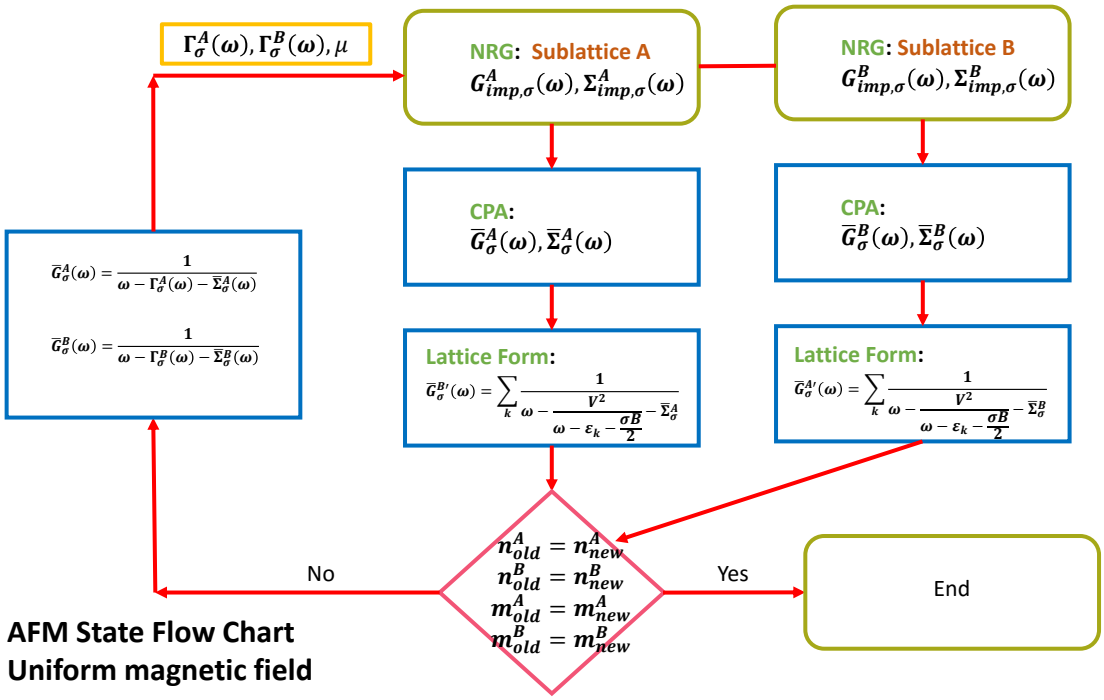

Figure 3.5: *Flow diagram of NRG + DMFT + CPA self-consistent calculation in the AFM state subjected to a uniform magnetic field. NRG calculation will be performed on sublattice A and B, respectively. The sublattice and spin dependent impurity Green's functions* $G_{imp,\sigma}^i(\omega)$ *and the impurity self-energies* $\Sigma_{imp,\sigma}^i(\omega)$*. Then CPA is applied to obtain the average Green's functions* $\bar{G}_\sigma^i(\omega)$ *and the averaged self-energies* $\bar{\Sigma}_\sigma^i(\omega)$*. With the averaged self-energies* $\bar{\Sigma}_\sigma^i(\omega)$*, the averaged Green's functions* $\bar{G}_\sigma^{i\prime}(\omega)$*in the lattice form are calculated. The magnetizations and the carrier densities per site of both sublattices A and B are compared. If they are sufficiently close to each other, the calculation converges. Otherwise, four new sublattice and spin dependent hybridization functions* $\Gamma_\sigma^i(\omega)$ *are constructed and a new chemical potential* μ *is obtained to be used in NRG in the next calculation.*

both the sublattice and spin dependences must be considered. Because NRG is designed for single site calculation, this problem have to be broken into two steps: sublattice A and sublattice B. The NRG calculation will be performed on these two sublattices, respectively. The sublattice and spin dependent impurity Green's functions $G_{imp,\sigma}^i(\omega)$ and the impurity self-energies $\Sigma_{imp,\sigma}^i(\omega)$. Then CPA is applied to obtain the average Green's functions $\bar{G}_\sigma^i(\omega)$ and the averaged self-energies $\bar{\Sigma}_\sigma^i(\omega)$. With the averaged self-energies $\bar{\Sigma}_\sigma^i(\omega)$, the averaged Green's functions $\bar{G}_\sigma^{i\prime}(\omega)$ in the lattice form are calculated. Similar to the case with a staggered magnetic field, the magnetizations and the carrier densities per site of both sublattices A and B are compared. If they are sufficiently close to each other, the calculation converges. Otherwise, four new sublattice and spin dependent hybridization functions $\Gamma_\sigma^i(\omega)$ are constructed and a new chemical potential μ is obtained to be used in NRG in the next calculation. Here the self-consistent algorithms is shown in Fig.(3.5).

Chapter 4

4 Phase Diagram and Lattice Coherence

In this chapter, the macroscopic physical properties of the AFM phase of the Anderson lattice model will be shown. Both the magnetic order parameter and the resistivity are calculated as functions of temperature and impurity concentration x. The obtained phase diagram is consistent with that of $Ce_{1-x}La_xCu_2Ge_2$ [1]. Mechanism behind the magnetic ordering and resistivity will be analyzed in the next chapter.

4.1 Magnetic Order Parameter $M\left(x,T\right)$

Here magnetization is defined as the difference between spin up and down occupation of the f-electron state on a single site divided by two:

$$M = \frac{\left|n_{\uparrow}^{f} - n_{\downarrow}^{f}\right|}{2}. \tag{4.1}$$

Fig.(4.1) shows magnetization as a function of temperature and impurity concentration. It can be seen that the magnetization developes in a narrow temperature range when the Néel temperature is approached. Also, the saturation magnetization decreases with respect to increase in impurity concentration x. In chapter 6 we will show that zero temperature magnetization continuously reduces to zero by increasing the doping concentration of non-magnetic impurity. Hence, there is a second order QPT at some critical concentration. By using the zero temperature magnetization, the critical concentration $x = x_c$ and the critical exponent β can be probed.

In the metallic heavy fermion systems, the long-range magnetic ordering has two possible origins [18]: Ruderman-Kittel-Kasuya-Yosida (RKKY) [86] and spin density wave (SDW) [87, 88]. For RKKY-type AFMs, the magnetizations originate from the ordering of the local spins of the f-orbitals. The interactions between these spins are mediated via the conduction band. While for the SDW-type AFMs, it is a two step processes: the local moments and the conduction band electrons form the Kondo singlets and the interaction between these singlets causes the spontaneous symmetry breaking and gives rise to the long-range magnetic ordering. In the vicinity of the QCPs, two different quantum critical behaviors may develop. One is described by the Hertz-Millis-Moriya theory [21–23] in the SDW picture. The other one is called the local quantum criticality at which the critical exponents are wavevector independent and the underlying mechanism is still under debate [89, 90].

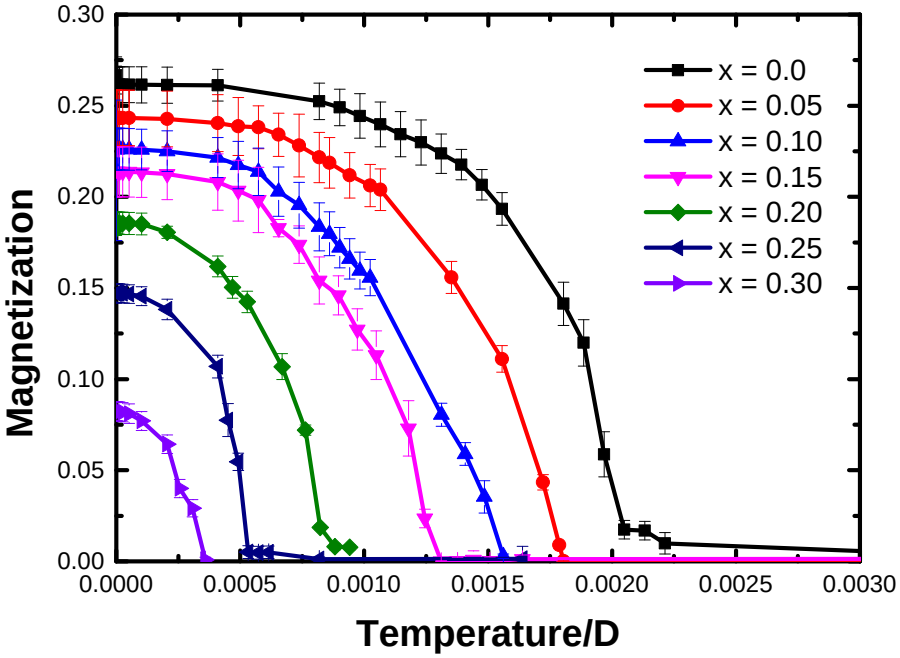

Figure 4.1: *Magnetization as functions of temperature and impurity concentration x. From the magnetization, Néel's temperature T_N can be calculated. Also, the saturation magnetization reduces by increasing impurity concentration.*

The universality class of the obtained QCP will be investigated in chapter 6 by calculating the critical exponents and comparing them with that of other heavy fermion AFM systems.

4.2 Resistivity

Fig.(4.2) shows the temperature and impurity concentration dependent resistivities of PM and AFM states (blue squares and red circles, respectively). Here we define lattice coherence temperature T^* as the temperature corresponding to the maximum of the resistivity. Two phenomena can be observed. First, including AFM phase does not affect the onset of lattice coherence. Lattice coherence means c-electrons and f-electrons hybridize and develope quasiparticles. This suggests the onset of lattice coherence is due to the Kondo exchange. Second, long-range magnetic ordering suppresses resistivity when lattice coherence is developed. This can be interpreted as loss of spin disorder scattering because magnetic ordering locks in the orientation of spin such that the Kondo exchange process is weakened. Conclusions will be given by more detailed investigations in the next chapter. Fig.(4.3) shows the resistivity and the magnetization as functions of temperature and impurity concentration x. Long range magnetic ordering take place below T^*. Therefore, we conclude that the lattice coherence is important to antiferromagnetism. It can be seen from Fig.(4.4), in which there is no impurity concentration, that the resistivity of the AFM phase much smaller than that of the PM phase.

To the end, the Mott-Ioffe-Regel limit [16, 91, 92] is used to test if charge carriers in the AFM state

can be considered as quasiparticles by comparing our resistivity with the MIR resistivity

$$\rho_{MIR}^{-1} = \sigma_{MIR} = \frac{1}{D}\int_0^D \sigma(\omega)\, d\omega, \tag{4.2}$$

where $\sigma(\omega)$ is the optical conductivity and D is the half band width. If the resistivity is larger than the ρ_{MIR}, we cannot think our system has coherent transport of quasiparticles anymore because the mean free path is shorter than the inter-particle distance. Optical conductivity $\sigma(\omega)$ will be calculated in chapter 5 and here we simply use the result. Fig.(4.5) shows the ρ and the ρ_{MIR} as functions of temperature and impurity concentration. This result suggests that at low temperature, charge carriers can be considered as quasiparticles in the Mott-Ioffe-Regel limit. In the next chapter, the f-electron dispersion relation shows that for sufficiently high temperature, lattice coherence disappears in our system.

Combining the magnetization and the resistivity as functions of temperature and impurity concentration x, it is possible to construct the phase diagram.

4.3 Phase Diagram

The phase diagram of our Anderson lattice model as a function of temperature and impurity concentration x is shown in Fig.(4.6). The AFM phase (blue) is seperated from the PM phase (pink) at low temperature. T^* is the onset temperature of lattice coherence. Above T^* (the white area), it is a PM state with incoherent scattering between local moments of f-electrons and conduction band c-electrons. It can be seen that the lattice coherence is important to the magnetic ordering. The phase diagram shows that there is a critical concentration x_c between $x = 0.3$ and $x = 0.35$. More detailed investigations in the region close to x_c will be shown in chapter 6. It also shows that the lattice coherence disappears at $x^* = 0.5$. This phase diagram, is consistent with that of the $Ce_{1-x}La_xCu_2Ge_2$ [1], shows that it is possible to have robust lattice coherence and magnetization with respect to high impurity concentration.

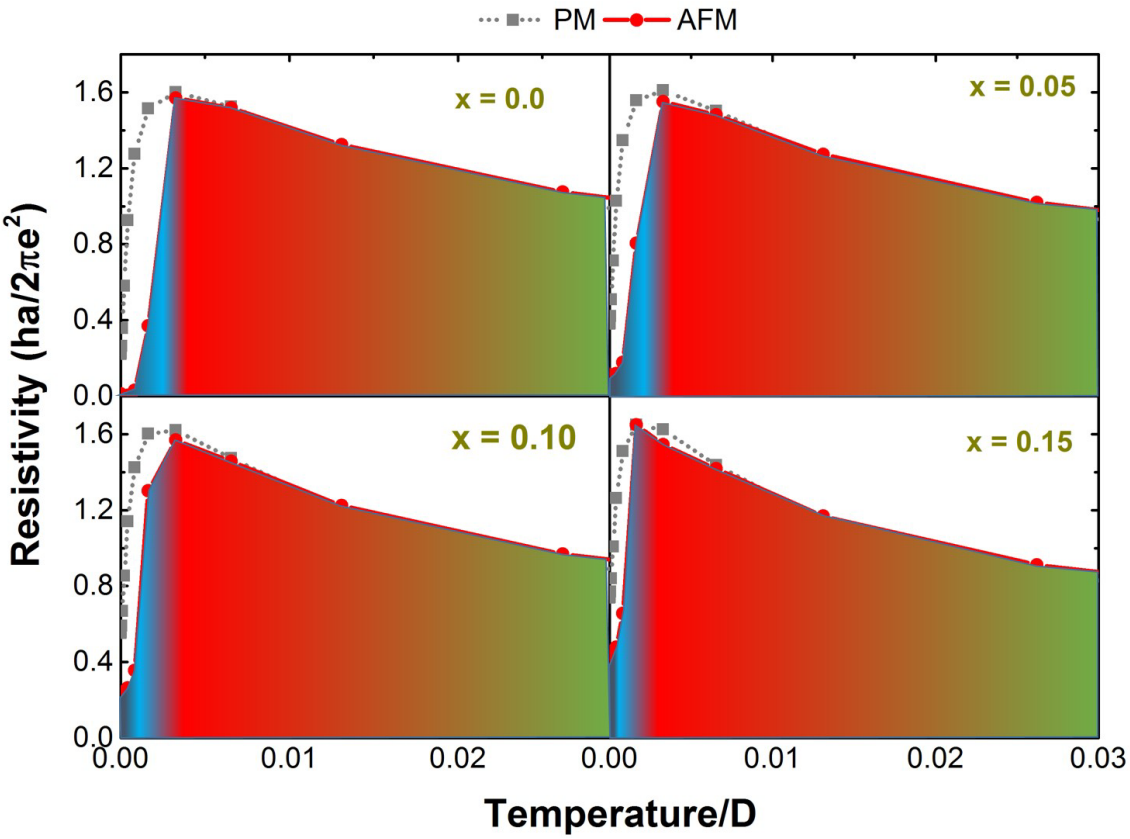

Figure 4.2: *Resistivities as functions of temperature and impurity concentration x in the PM and the AFM phases. The gray squares and the red circles represent the resistivity in the PM and the AFM phases, respectively. Two phenomena can be observed. First, including the AFM phase does not affect the onset of lattice coherence. Second, long-range magnetic ordering suppresses the resistivity when the lattice coherence is developed. This can be interpreted as loss of spin disorder scattering because magnetic ordering locks in the orientation of spin such that the Kondo exchange process is weakened. Lattice coherence temperature is defined as the temperature corresponding to the maximum of the resistivity.*

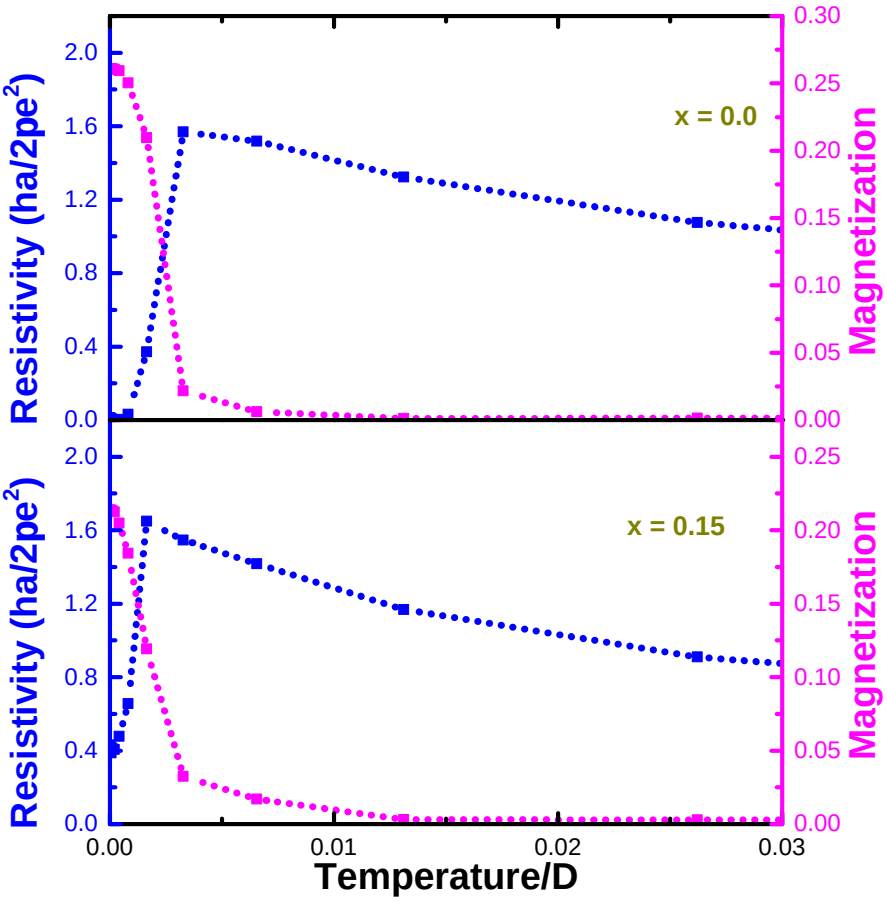

Figure 4.3: *Resistivity and magnetization as functions of temperature at impurity concentration* $x = 0.0$ *and* $x = 0.15$*. Blue squares and magenta diamonds represent the resistivity and the magnetization, respectively. The long-range magnetic ordering and the lattice coherence take place at the same temperature. Therefore we conclude that the lattice coherence is important to the antiferromagnetism.*

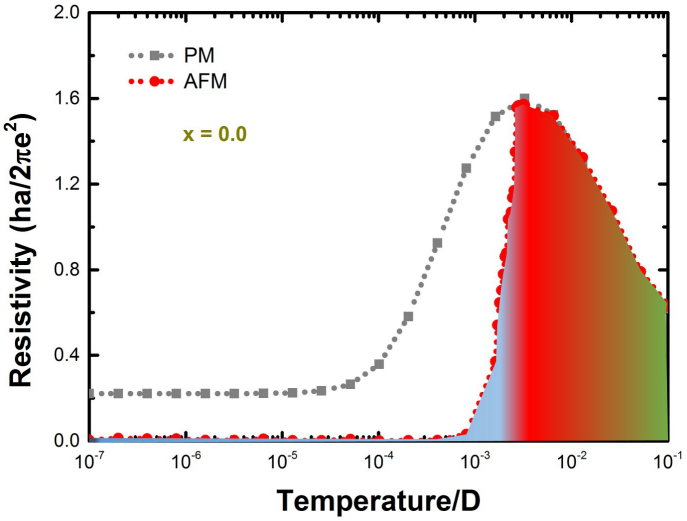

Figure 4.4: *Resistivities as functions of temperature at impurity concentration $x = 0.0$ in the PM and the AFM phases. The gray squares and the red circles represent the resistivities in the PM and the AFM phases, respectively. Here we want to emphasize that the magnetic ordering strongly suppresses the resistivity.*

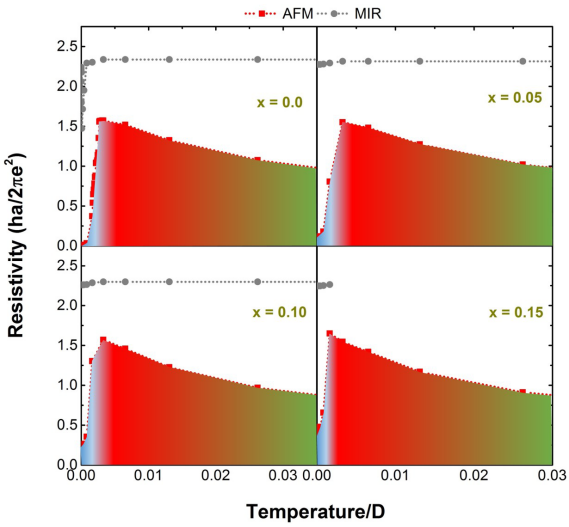

Figure 4.5: *MIR resistivity ρ_{MIR} (gray dots) and AFM resistivity ρ (red dots) as functions of temperature and impurity concentration x. The obtained ρ_{MIR} is consistent with other heavy fermion compounds [16]. This result suggests that at low temperature, charge carriers can be considered as quasiparticles in the Mott-Ioffe-Regel limit. In the next chapter, the f-electron dispersion relation shows that for sufficiently large temperature, lattice coherence disappears in our system.*

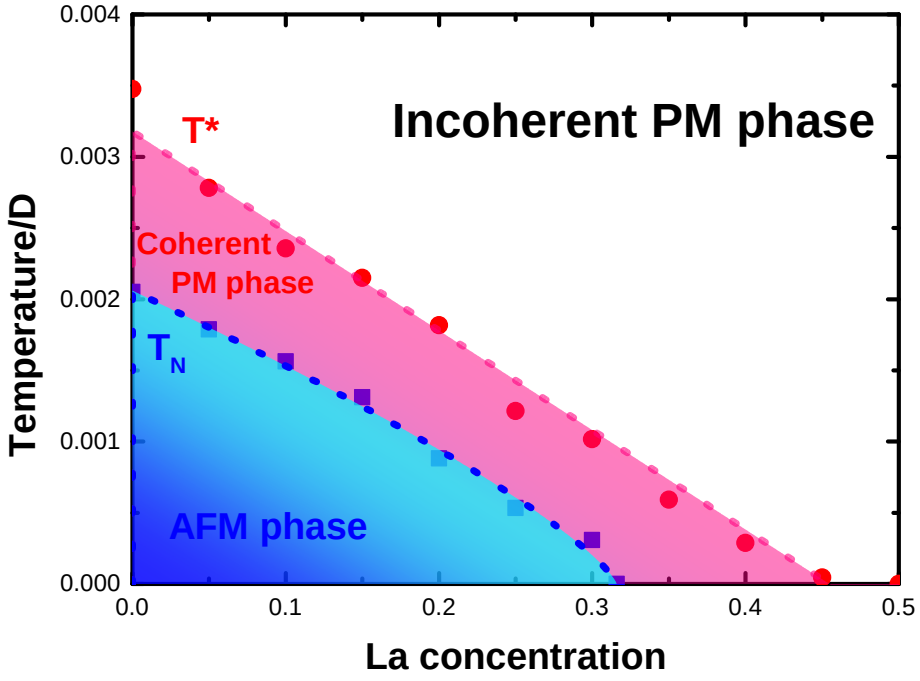

Figure 4.6: *Phase diagram of our Anderson lattice model as a function of temperature and impurity concentration x. An AFM phase (blue) is seperated from a PM phase (pink) at low temperature. Above T^* (the white area), it is a PM state with incoherent scattering between local moments of f-electrons and conduction band c-electrons. A quantum phase transition takes place close to $x \sim 30\%$. Meanwhile, the lattice coherence disappears at impurity concentration $x = 50\%$. This diagram is consistent with that of the $Ce_{1-x}La_xCu_2Ge_2$ [1]. Our result suggests that the lattice coherence is crucial to the long-range magnetic ordering.*

Chapter 5
5 Single Particle and Optical Excitation

In this chapter, a general physical picture of the obtained AFM heavy fermion system will be given. To achieve our goal, various quantities such as the spectral function, the dispersion relation, the self energy, and the optical conductivity will be investigated systematically.

5.1 f-Electron Spectral Function

In this section we exam the f-electron spectral function to investigate the difference between single particle excitations in the AFM and the PM phases. From Fig.(5.1), it can be seen that in the AFM phase a gap is opened at the Fermi level between the two spin states and the peaks of the spectral functions are shifted away from the PM Friedel-Anderson resonance. The gap in the AFM spin up spectral function coincides with the maximum of spin down state. Hence in the AFM phase, the spin up and down states avoid each other and the electron-electron scattering is reduced. Therefore, the resistivity can be significantly decreased by effectively reducing the Coulomb interaction. Moreover, the spin dependent single particle excitations close to the Fermi level suggest non-static Kondo coupling because the Kondo singlet requires the spin up and down states be on an equal footing. Because the static Kondo singlet is short lived, if it still exists, it cannot be the main mechanism for the reduction in the resistivity by screening local spins; therefore, it can be concluded that the low resistivity is mainly due the formation of the magnetic ordering. This point of view is supported by the dispersion relations and the hybridization functions shown later.

It can be seen that close to the QCP, the AFM and the PM spectral functions converge. As a result, the static Kondo singlet can be expected on the other side of the QCP.

Here we ask two questions: 1. How do we know when the f-electrons evolve from the itinerant wave-like state to the atomic particle-like state? 2. What causes the crossover? Fig.(5.2) shows the f-electron spectral functions at two different impurity concentrations: 0% and 99%. From the spectral functions, it is impossible to tell the difference between them experimentally. Therefore, other methods must be used to tell when the f-electrons are localized again. In section 5.5.4 we will show that the electromagnetic response is a useful tool to distinquish the duality of the f-electron state. We will also try to give an answer to the second question based on our results.

In the end of this section, analysis based on the dispersion relations in the PM and the AFM phases will be used to investigate the characters of the lattice coherence. The PM phase will be analyzed first

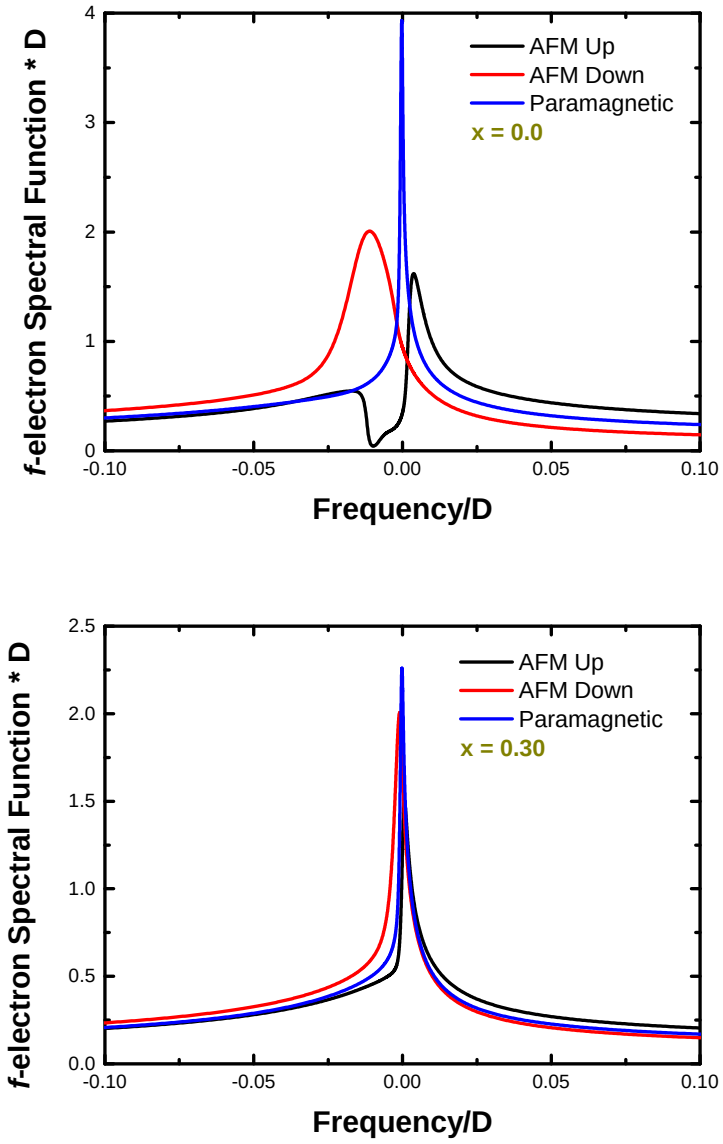

Figure 5.1: *f-electron spectral function $A^f_\sigma = -\frac{1}{\pi}\Im G^f_\sigma\left(\frac{\omega}{D}\right)$ as a functions of frequency at zero temperature at the impurity concentration $x = 0.0$ and $x = 0.30$ in two different phases. Black line, red line, blue line represent the AFM spin up state, the AFM spin down state, the PM state, respectively. The gap in the AFM spin up spectral function coincides with the maximum of the spin down state. Hence, in the AFM phase spin up and down states avoid each other and the Coulomb interaction is effectively reduced. By increasing the impurity concentration, these three spectral functions converge close to the QCP.*

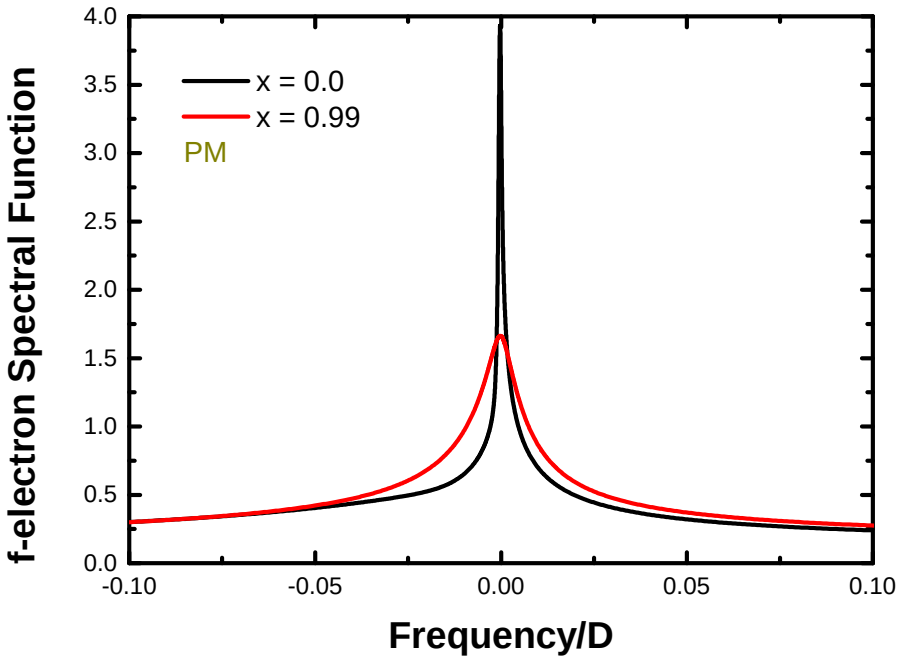

Figure 5.2: *f-electron spectral function $A^f_\sigma = -\frac{1}{\pi}\Im G^f_\sigma\left(\frac{\omega}{D}\right)$ as a functions of frequency at zero temperature at impurity concentration $x = 0.0$ and $x = 0.99$ in the PM phase. Black line and red line represent $x = 0\%$ and $x = 99\%$, respectively. From this result we know that it is impossible to tell if the system has lattice coherence by the spectral function at low temperature. Therefore, other experiments should be used to distinguish the particle-wave duality of the f-electron state.*

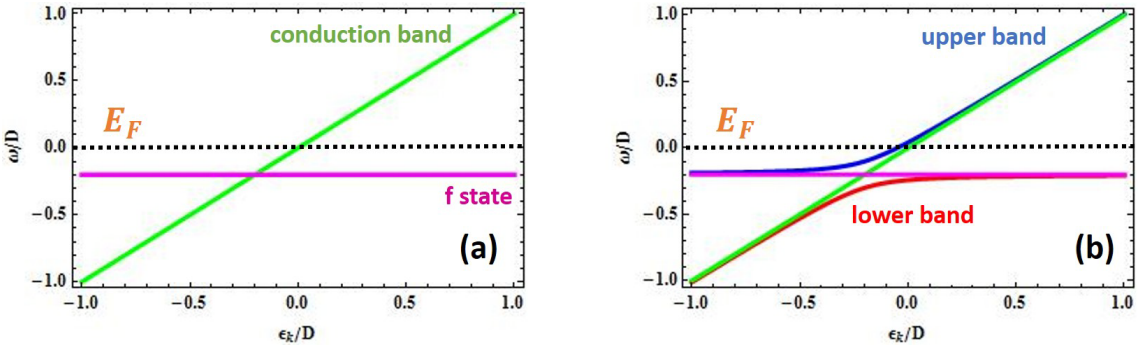

Figure 5.3: *(a) The c-electron (green line) and the f-electron (pink line) dispersion relations before hybridization. (b) By including interaction between the c-electron and the f-electron, they develop a two bands structure indicated by the red line and the blue line. Interband transition takes place between these two bands and can be used as an indicator for the lattice coherence.*

so a clearer picture can be established.

5.1.1 PM Phase Dispersion

In Fig.(5.3), we use a toy model to illustrate how the f-electrons and the c-electrons hybridize. In Fig.(5.3.a) it shows the c-electron and the f-electron dispersion relations before hybridization. When they hybridize, they develop a two bands structure indicated by the red line and the blue line shown in Fig.(5.3.b). Interband transition takes place between these two bands and can be used as an indicator for the lattice coherence. Although this is an overly simplified picture which does not include the many body effect, it captures the necessary ingredients of band hybridization and help us understand the more complicated case in which the many-body effect comes in.

At $x = 0.0$, a quasiparticle state at energy $\epsilon_k = \epsilon^*$ is formed which implies a strongly renormalized Fermi liquid quasiparticle shown in Fig.(5.4). With increasing impurity concentration, single particle excitations gradually lose quasiparticle character and become localized indicated by the broadening of the extended red region. When the impurity concentration is sufficiently high, the excitation spectrum extends over all ϵ_k and the f-electron state is localized. The evolution of the quasiparticle state as a function of frequency at various impurity concentrations x at zero temperature is shown in Fig.(5.5).

From the f-electron dispersion relation, the formation of the Fermi liquid quasiparticle can be seen clearly; therefore, we may ask the question that what happens close to the maximum of the PM resistivity shown in the last chapter. The temperature dependent f-electron dispersion relation of $x = 0.0$ is shown in Fig.(5.6). It can be seen that close to the maximum of the resistivity, the lattice coherence breaks down.

Based on the conclusions obtained from this section, we continue our analysis in the AFM phase.

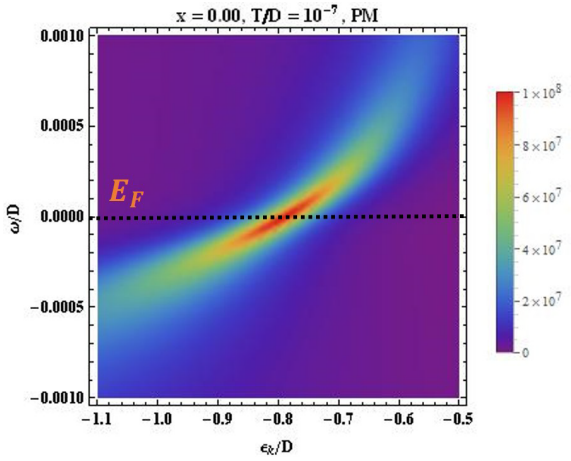

Figure 5.4: *Zero temperature f-electron dispersion relation $A^f = -\frac{1}{\pi}G^f\left(\frac{\epsilon}{D}, \frac{\omega}{D}\right)$ at impurity concentration $x = 0$ in the PM phase. A strongly renormalized Fermi-liquid quasiparticle is formed with $\frac{\epsilon_k}{D} = -0.8$ indicating the f-electrons behave as waves and develope the lattice coherence.*

5.1.2 AFM Phase Dispersion

In the AFM phase, the zero temperature f-electron dispersion relation shows the spin dependence at impurity concentration $x = 0.0$ in the AFM state as can be seen in in Fig.(5.7). Both the spin up and down states develope the strongly renormalized quasiparticles. However, they have different characters. The spin up state is *insulating* and the spin down state is *itinerant*. A gap is opened close to the Fermi level in the spin up state and this is consistent with the spin up f-electron spectral function shown in Fig.(5.1). The dispersion relation of the spin down state indicates a fast group velocity:.

$$v_g = \frac{\partial \omega}{\partial k}. \tag{5.1}$$

Hence the spin down quasiparticle has a strong dynamical character. By increasing the impurity concentration, it can be seen in Fig.(5.8) that the spin up and the spin down dispersion relations converge close to the QCP. The convergence suggests that the AFM state is suppressed and the static Kondo singlet reemerges close to the QCP.

5.2 Self Energy

In this section we investigate the reduction of the resistivity in the AFM state from the perspective of the self energy.

The electron scattering strength can be analyzed via the imaginary part of the impurity averaged self energy, which includes both the electron-electron scattering and the electron-impurity scattering.

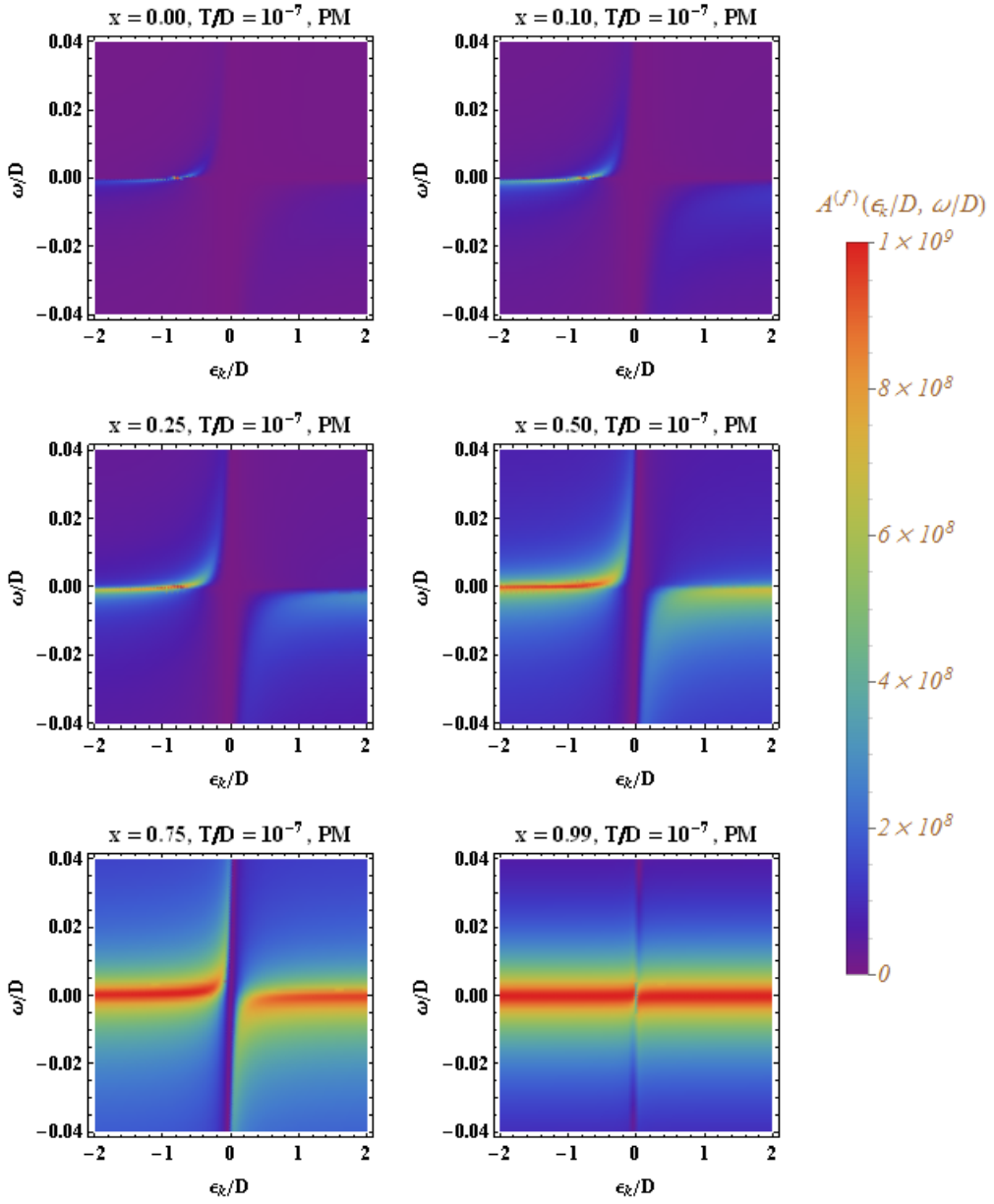

Figure 5.5: *Evolution of the f-electron dispersion relation $A^f = -\frac{1}{\pi}G^f\left(\frac{\epsilon}{D}, \frac{\omega}{D}\right)$ at zero temperature in the PM phase at several different the impurity concentrations. The lattice coherence is sabotaged with increase in the impurity concentration. For sufficiently large impurity concentration, the lattice coherence disappears and the f-electrons become particle-like.*

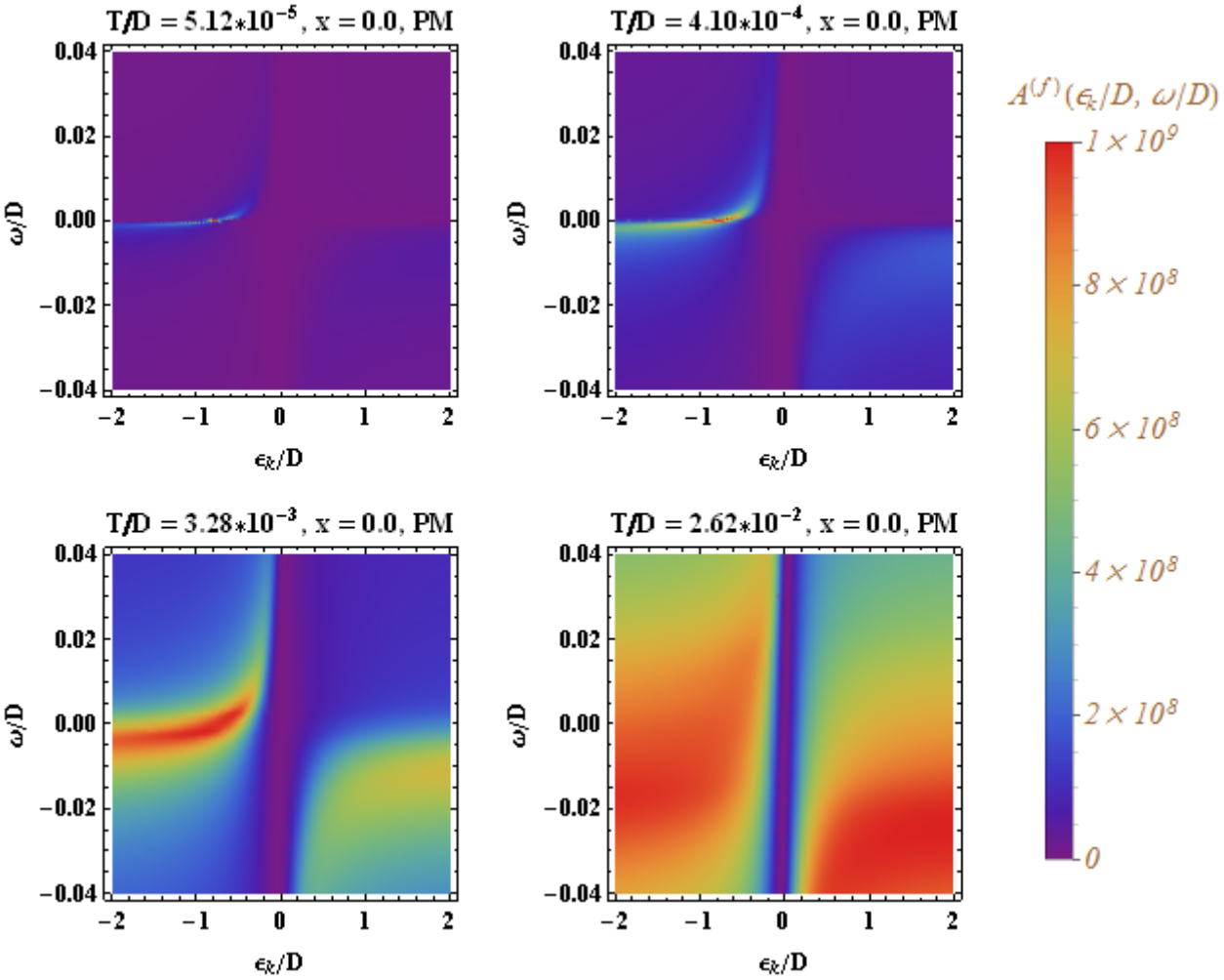

Figure 5.6: *Evolution of the f-electron dispersion relation $A^f = -\frac{1}{\pi}G^f\left(\frac{\epsilon}{D}, \frac{\omega}{D}\right)$ at impurity concentration $x = 0$ in the PM phase at several different temperatures. The lattice coherence is suppressed with the increase in temperature. For sufficiently high temperature, the lattice coherence disappears and the f-electrons become particle-like.*

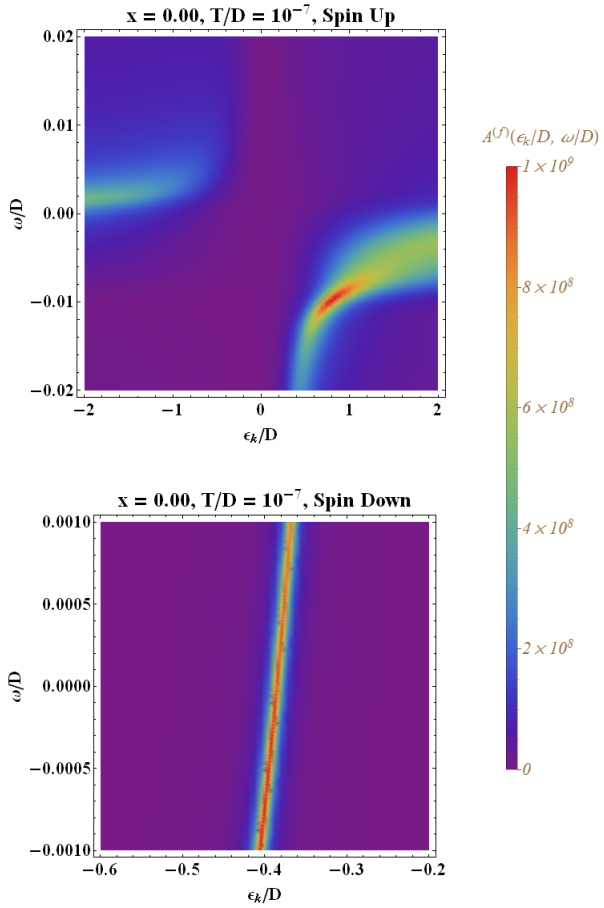

Figure 5.7: *Zero temperature spin dependent f-electron dispersion relation $A^f_\sigma = -\frac{1}{\pi}G^f_\sigma\left(\frac{\epsilon}{D}, \frac{\omega}{D}\right)$ at impurity concentration $x = 0$ in the AFM phase. Both the spin up and down states develope strongly renormalized quasiparticles. However, they have different characters. The spin up state is **insulating** and the spin down state is **itinerant**. A gap is opened close to the Fermi level in the spin up state and this is consistent with the spin up f-electron spectral function shown in Fig.(5.1). The dispersion relation of the spin down state indicates a fast group velocity; therefore the spin down quasiparticle has a strong dynamics character.*

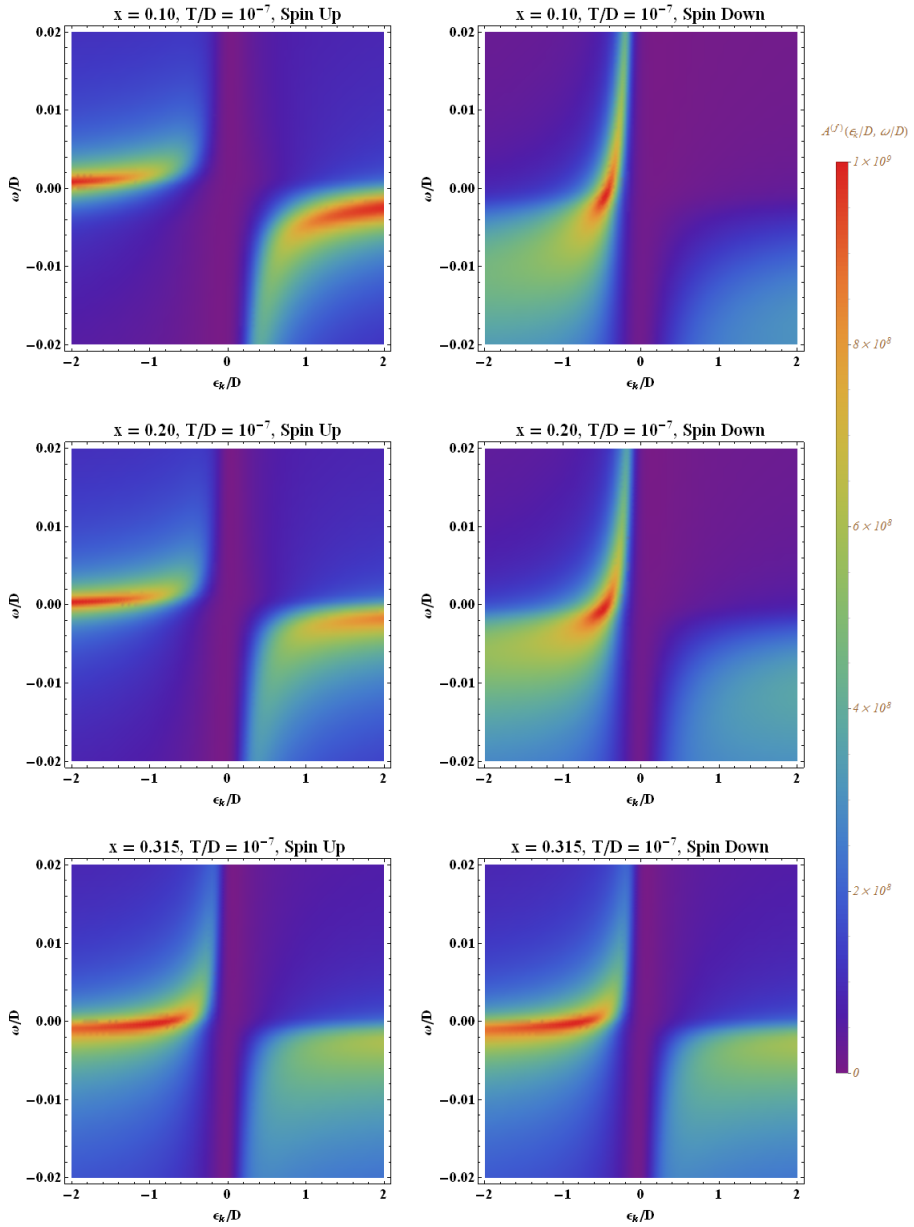

Figure 5.8: *Zero temperature spin dependent f-electron dispersion relation $A^f_\sigma = -\frac{1}{\pi} G^f_\sigma \left(\frac{\epsilon}{D}, \frac{\omega}{D}\right)$ in the AFM phase at the impurity concentrations $x = 0.10,\ 0.20,\ 0.315$. Both the lattice coherence and the difference in the dispersion relation are suppressed with increase in the impurity concentration x. For sufficiently high impurity concentration, the f-electron dispersion relations converge close to the QCP. As a result, the spin up and down states are degenerate. Therefore, the magnetic ordering disappears and the static Kondo singlet reemerges.*

To illustrate the effect of the impurity concentration on the scattering rate in the AFM state, the zero temperature ratios between the imaginary part of the spin dependent impurity averaged self energy in the AFM state$\Sigma_{\sigma}^{f,AFM}$ and the impurity averaged self energy $\Sigma^{f,PM}$ in the PM state as a function of the impurity concentration are shown in Fig.(5.9). It can be seen that the AFM state reduces both the electron-electron and electron-impurity scattering. The reason for the decrease in the effective Coulomb interaction is provided in section 5.5.1 and we want to discuss the physics behind the reduction in the impurity scattering strength.

An impurity can be effectively considered as a potential barrier for the quantum coherence state. In the introductory quantum mechanics class, we learned that for a quantum state with energy smaller than that of a potential wall, there is a finite probability for the state to penetrate through the wall and the result is energy dependent: the higher the energy of the quantum state is, the higher the chance to move to the other side of the wall. In the previous section it was shown that the quantum coherence state in the AFM phase has a strong dynamical charater which means that it has a wider energy profile than that of the quantum state in the PM phase. Therefore, the quantum state in the AFM phase has a higher probability to pass through the impurity barrier. As a result, the impurity scattering is relatively weak in the AFM phase.

5.3 cf-Hybridization

By investigating the occupation numbers of the f-electron and the c-electron, the properties of cf-hybridization can be revealed.

Our previous results suggest that the static Kondo singlet state is not energetically favorable in the AFM phase due to the difference between the spin up and down states. This perspective is also supported by the hybridization function shown in Fig.(5.10). At $x = 0.0$ in the AFM state, the static coupling between the f-electron spin down state and the c-electron state (the red line) are not stable indicated by the relatively large value of the hybridization function $\Gamma(0)$, which is defined in Chapter 3. The f-electron spin up state and the c-electron state (the black line) are strongly coupled. Because the Kondo coherence state requires both the f-electron spin up and down states to couple equally to the c-electron state, the static Kondo coupling breaks down in the AFM phase at low temperature. Close to the QPT, the spin up and down states become degenerate and the static Kondo singlet emerges.

Here we may ask what the interaction channel between the cf-hybridization is and the c-electron spectral function is examed. Fig.(5.11) shows the zero temperature spectral functions of the f-electrons and the c-electrons at zero impurity concentration. From the occupation number, it can be seen that they are coupled antiferromagnetically.

In the next section, we will see that by measuring the optical conductivity with microwave spectroscopy and Fourier transform infrared spectroscopy (FTIR), more insights into the mechanism of the AFM heavy fermion systems might be provided.

5.4 Optical Conductivity and f-sum Rule

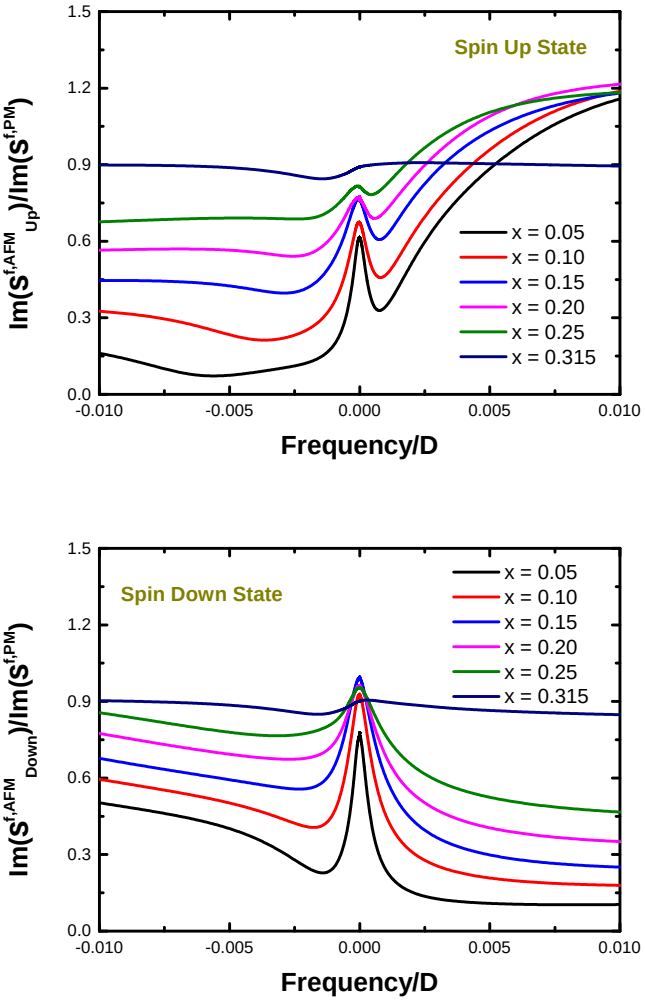

Figure 5.9: *Zero temperature ratios between the imaginary part of the spin dependent impurity averaged self-energy in the AFM state* $\Sigma_\sigma^{f,AFM}$ *and the impurity averaged self-energy in the PM state* $\Sigma^{f,PM}$ *as functions of frequency for several different impurity concentrations. AFM state reduces both electron-electron and electron-impurity scattering in spin up and down states.*

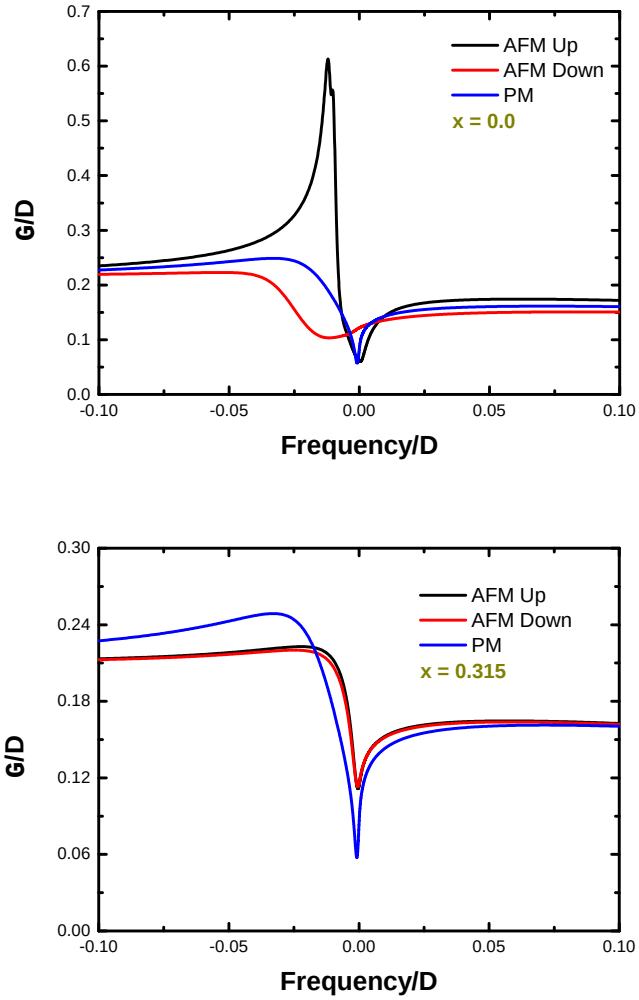

Figure 5.10: *Zero temperature hybridization functions* Γ *in the AFM and the PM phases as functions of frequency at the impurity concentrations* $x = 0.0$ *and* $x = 0.315$*. At* $x = 0.0$ *in AFM state, the static coupling between the* f*-electron spin down state and the c-electron state (the red line) are not stable indicated by the relatively large value of the hybridization function* $\Gamma(0)$*. The* f*-electron spin up state and the c-electron states (the black line) are strongly coupled. Close to the QCP, the spin up and down states become degenerate.*

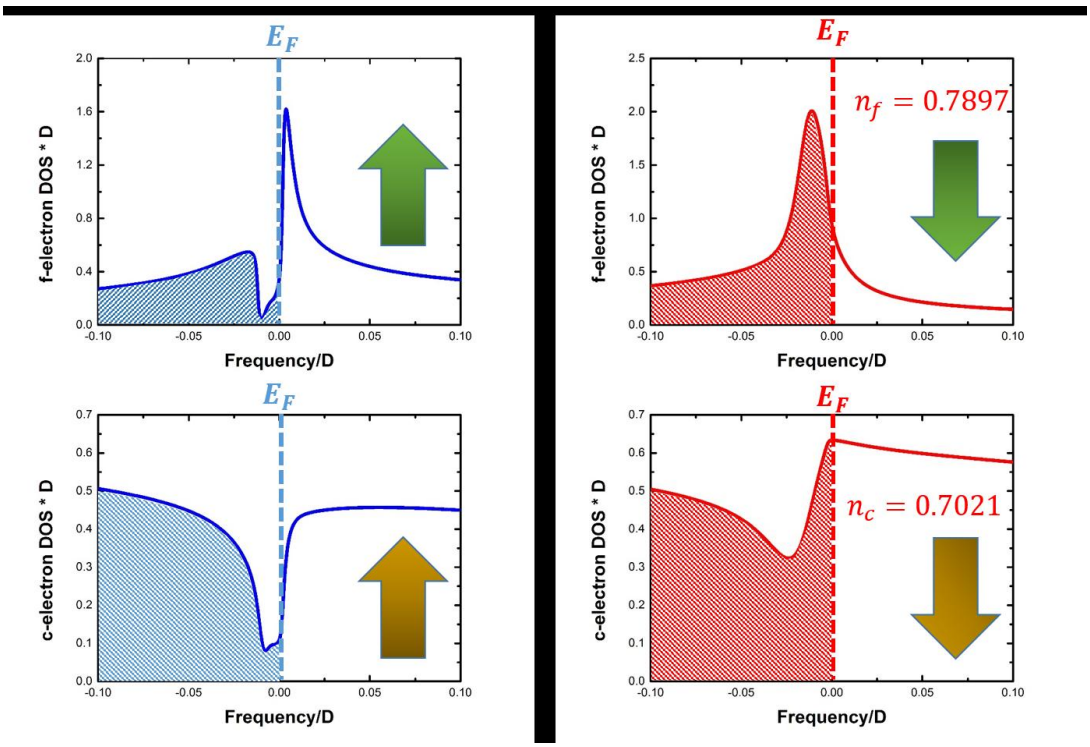

Figure 5.11: *Zero temperature spectral functions of the f-electron and the c-electron at impurity concentration $x = 0.0$. From the occupation number, it can be seen that f-electrons and c-electrons are coupled antiferromagnetically.*

The real part of optical conductivity $\sigma_{xx}\left(\omega,T\right)$ can be written as [93]

$$\begin{aligned}\sigma_{xx}\left(\omega,T\right) &= -\pi e^2\sum_{\sigma}\int d\epsilon\Phi_{xx}\left(\epsilon\right)\int d\omega'\left[\frac{f\left(\omega',T\right)-f\left(\omega'+\omega,T\right)}{\omega}\right] \\ & A_{\sigma}\left(\omega',\epsilon,T\right)A_{\sigma}\left(\omega'+\omega,\epsilon,T\right) \end{aligned} \tag{5.2}$$

with

$$\Phi_{xx}\left(\epsilon\right)=\sum_{k}\left(\frac{\partial\epsilon}{\partial k_x}\right)^2\delta\left(\epsilon-\epsilon_k\right) \tag{5.3}$$

where $A_{\sigma}\left(\omega,\epsilon,T\right)$ is the single particle c-electron dispersion relation and $f\left(\omega,T\right)$ is the Fermi distribution function. Then by the Kramers-Kronig transformation, the imaginary part of the optical conductivity can also be obtained:

$$\Im\left(\sigma\left(\omega\right)\right) = -\frac{1}{\pi}\Pr\int_{-\infty}^{\infty}d\omega'\frac{\Re\left(\sigma\left(\omega'\right)\right)}{\omega'-\omega} \tag{5.4}$$

such that the optical conductivity is a complex quantity:

$$\sigma\left(\omega\right)=\sigma_1\left(\omega\right)+i\sigma_2\left(\omega\right) \tag{5.5}$$

By combining the real part and the imaginary part of the optical conductivity, the extended Drude model (EDM) [17, 94, 95] yields analyze the effective mass m^*/m_0 enhancement and the scattering rate $1/\tau\left(\omega\right)$ of the system:

$$\frac{m^*}{m_0} = \frac{\Omega^2}{4\pi\omega}\frac{\sigma_2}{\sigma_1^2+\sigma_2^2} \tag{5.6}$$

$$\frac{1}{\tau} = \frac{\Omega^2}{4\pi}\frac{\sigma_1}{\sigma^2+\sigma_2^2} \tag{5.7}$$

with Ω the plasma frequency. Again we start with the PM optical conductivity to establish the foundation for the analysis of the optical conductivity in the AFM state.

5.4.1 Optical Conductivity in PM Phase

Fig.(5.12) shows σ_1 and σ_2 as a function of frequency for different temperatures at impurity concentration $x = 0.0$. It can be seen that at low temperature, σ_1 develops a sharp Drude-like peak at low frequency and a strong absorption at zero frequency is shown in σ_2. This behavior indicates a metallic state [96]. This result suggests that a strongly renormalized Fermi liquid is formed. By increasing temperature, the sharp peak disappears and the high temperature optical conductivity can be fitted by the classical Drude model, which can be seen in Fig.(5.13). The temperature dependence of the absorption shows the evolution of electrons from a strongly renormalized Fermi liquid to a non-interacting metallic state.

In Fig.(5.14) the effective mass enhancement m^*/m_0 as a function of frequency for different temperatures at impurity concentration $x = 0.0$ are shown. At low temperature the c-electrons show the strong mass renormalization and lose the heavy fermion character at high temperature. On the other hand, the position of the maximum of $1/\tau(\omega)$ corresponds to the onset of the mass renormalization and the peak feature indicates the temporal coherence. Therefore, this strong scattering process can be interpreted as coherent dynamical Kondo scattering. The Kondo scattering loses its temporal coherence by increasing temperature. For sufficiently high temperature, both the temporal coherence in the Kondo scattering and the mass renormalization disappear. Therefore, it shows that the large effective mass is connected with the dynamically coherent spin flip exchange interaction. The behaviors of the effective mass and the scattering rate are consistent with the experimental results of various heavy femion systems such as $YbRh_2Si_2$, $CeRu_4Sb_{12}$, and $YbFe_4Sb_{12}$ in the PM state [17, 97].

Next we investigate the optical conductivity as a function of frequency at zero temperature and different impurity concentrations shown in Fig.(5.15). The increase in the impurity concentration makes the system more insulator like and decreases the energy for the interband transition. While $\sigma_2(\omega)$ shows that for sufficiently high impurity concentration, there is no absorption at zero frequency which marks the crossover from the lattice coherent picture to the single impurity picture. This crossover is also reflected by the effective mass and the scattering rate shown in Fig.(5.16). For the impurity concentration between 40% to 50%, the effective mass flips its sign and the low frequency scattering dominates. From Fig.(5.17) it can be seen clearly that static scattering rate increases as a function of impurity concentration and for sufficiently large impurity concentration when interband scattering vanishes, there is no lattice coherence. The f-electrons become atomic particle-like by suppressing the interband scattering process.

5.4.2 Optical Conductivity in AFM Phase

Here we show the optical conductivity as a function of temperature and the impurity concentration in the AFM phase. If we only look at Fig.(5.18), we might think there is nothing special about the AFM phase compared with the PM phase from the perspective of optical conductivity. However, if we zoom in $\sigma_2(\omega)$ down to the energy scale $\omega/D = 10^{-4}$, we see that in the AFM state there is an extra bound state in Fig.(5.19). This excitation ***might*** be due to the Feshbach resonance as a result of coupling of the cf-hybridization AFM and FM channels [98]. Fig.(5.20) shows the effective mass $\frac{m^*}{m_0}$ and the scattering rate of the c-electron as a function of temperature at impurity concentration $x = 0$ in the AFM phase. Similar to the scattering rate in the PM phase, the Kondo spin flip also loses its temporal coherence by increasing temperature and becomes incoherent above the lattice coherence temperature. The negative effective mass can be interpreted as an absorption of the bound state. However, unlike the interband scattering which is characterized by a peak in the scattering rate, this bound state is not accompanied with the scattering rate and it can be interpreted as a Feshbach resonance [98]. Recently a ultracold atomic system is proposed to observe the Kondo effect by the optical Feshbach resonance [99]. Therefore, it should also be possible to detect the Feshbach resonance in the Kondo systems.

Fig.(5.21) shows the impurity concentration dependent optical conductivity in the AFM state at zero temperature. Again, it seems there is no difference between the optical conductivities in the PM and the AFM phase. Similar to the temperature dependent optical conductivity at the impurity concentration $x = 0.0$ in the AFM state, the optical conductivity shows interesting behavior below the energy scale $\frac{\omega}{D} = 10^{-4}$ in the imaginary part shown in Fig.(5.22). The effective mass shows the itinerant heavy fermion behavior in the high energy region and something unexpected in the low energy

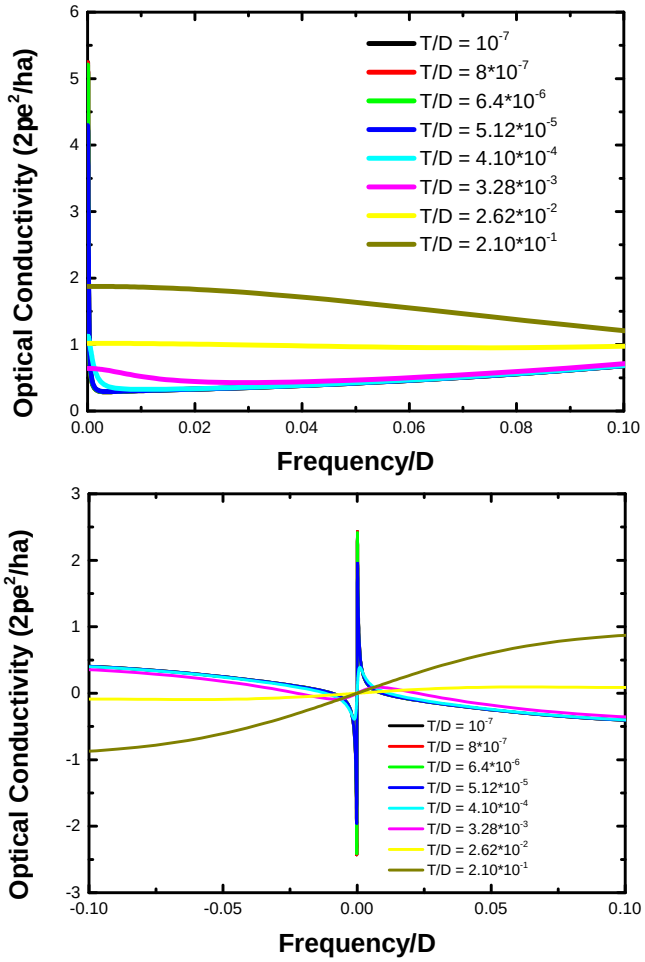

Figure 5.12: *(Upper figure) Real part of the optical conductivity $\sigma(\omega)$ of c-electron as a function of frequency at impurity concentration $x = 0.0$ and several different temperatures in PM phase. A strongly renormalized Drude peak is developed at low temperature at zero frequency. By increasing temperature, the sharp Drude peak disappears. (Lower figure) Imaginary part of optical conductivity $\sigma(\omega)$ of the c-electron as a function of frequency at $x = 0.0$ and several different temperatures in the PM phase. At low temperature there shows a strong absorption at zero frequency. The temperature dependence of the absorption shows the evolution of the c-electrons from a strongly renormalized Fermi liquid to a non-interacting charge carriers.*

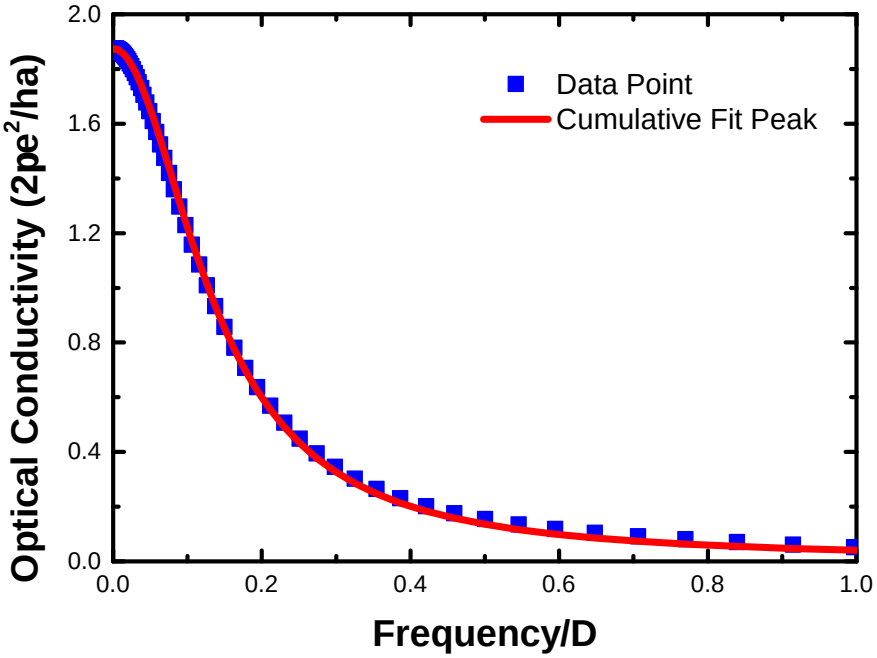

Figure 5.13: *Real part of high temperature optical conductivity $\sigma(\omega)$ of the c-electron (blue circies) as a function of frequency at impurity concentration $x = 0.0$. It can be fitted by the classical Drude model (red line).*

region. While the behavior of the scattering rate is similar to that of the PM state, the Kondo exchange becomes more static close to the QCP.

Finally, the effective masses and the scattering rates of the PM and AFM states are compared at $x = 0.0$ and zero temperature shown in Fig.(5.24). First it can be observed that in the AFM phase, the mass renormalization is much weaker than that of the PM phase. Second, in the AFM phase the cf-hybridization gap is one order of magnitude larger than that of the PM phase. By having a relatively large gap, the Kondo physics takes place at a higher frequency than that in the PM phase. Most importantly, the sharper scattering peak in the AFM phase indicates a better temporal coherence in the spin flip process.

Hence, it can be concluded that the decrease in the resistivities and the lattice coherence below the coherence temperatures in the heavy fermion systems is due to dynamically coherent Kondo exchange interaction. The better the temporal coherence, the better the lattice coherence.

5.4.3 $f-$Sum Rule

In order to check the validity of our results on the optical conductivity, the f-sum rule is applied:

$$\frac{1}{\pi}\int_0^\infty d\omega\sigma(\omega) = \frac{1}{2}\sum_{k,\sigma}\left(\frac{\partial^2\epsilon_k}{\partial k_x^2}\right)\left\langle n_{k,\sigma}\right\rangle \tag{5.8}$$

Fig.(5.25) shows that our results obey the f-sum rule for both the PM and the AFM phases.

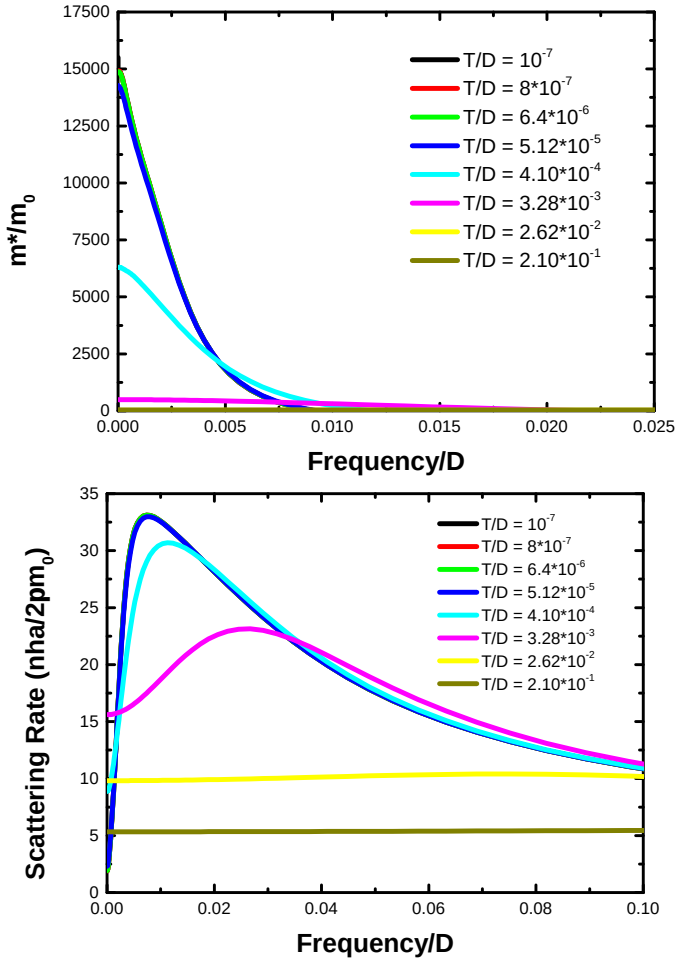

Figure 5.14: *(Upper figure) Effective mass enhancement m^*/m_0 of c-electron as a function of frequency at impurity concentration $x = 0.0$ and several different temperatures in the PM phase. At low temperature, the c-electrons show the strong mass renormalization and loss the heavy fermion character at high temperature. (Lower figure) Scattering rate of the c-electron as a function of frequency at impurity concentration $x = 0$ and several different temperatures in the PM phase. The position of the maximum of the scattering rate corresponds to the onset of mass renormalization and the peak feature indicates the temporal coherence. The system loses its coherent Kondo scattering and the mass renormalization by increasing temperature. Therefore, it can be concluded that the strong mass renormalization is due to the dynamically coherent Kondo process..*

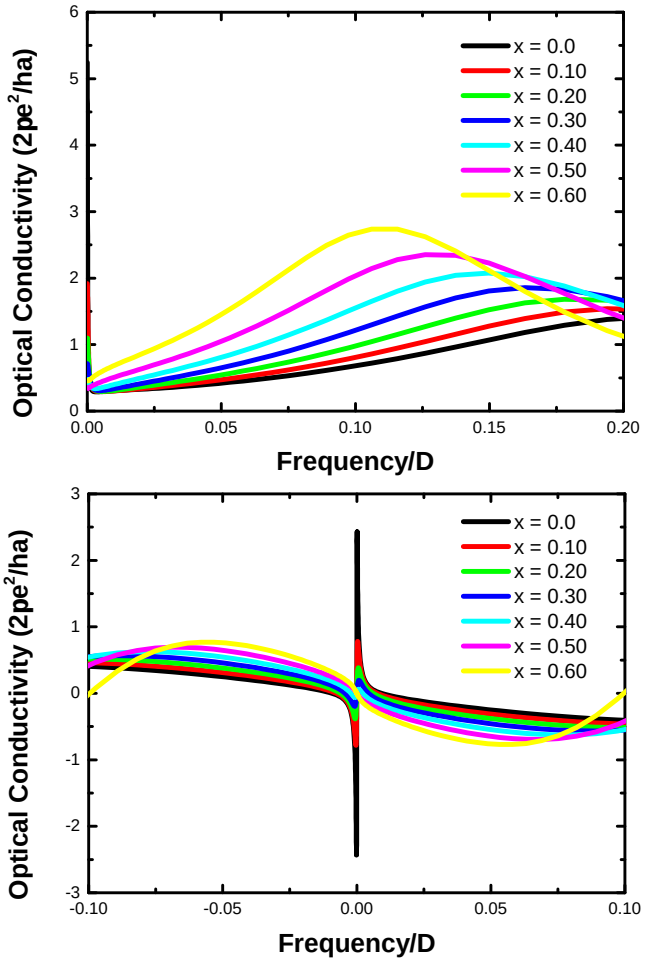

Figure 5.15: *(Upper figure) Real part of zero temperature optical conductivity $\sigma(\omega)$ of the c-electron as a function of frequency at several different impurity concentrations in the PM phase. Increase in impurity concentration makes the system more insulator like and decreases the energy of the interband transition. (Lower figure) Imaginary part of zero temperature optical conductivity $\sigma(\omega)$ c-electron as a function of frequency at several different impurity concentrations in the PM phase. For sufficiently high impurity concentration, there is no absorption at zero frequency which marks the disappearance of the itinerant state.*

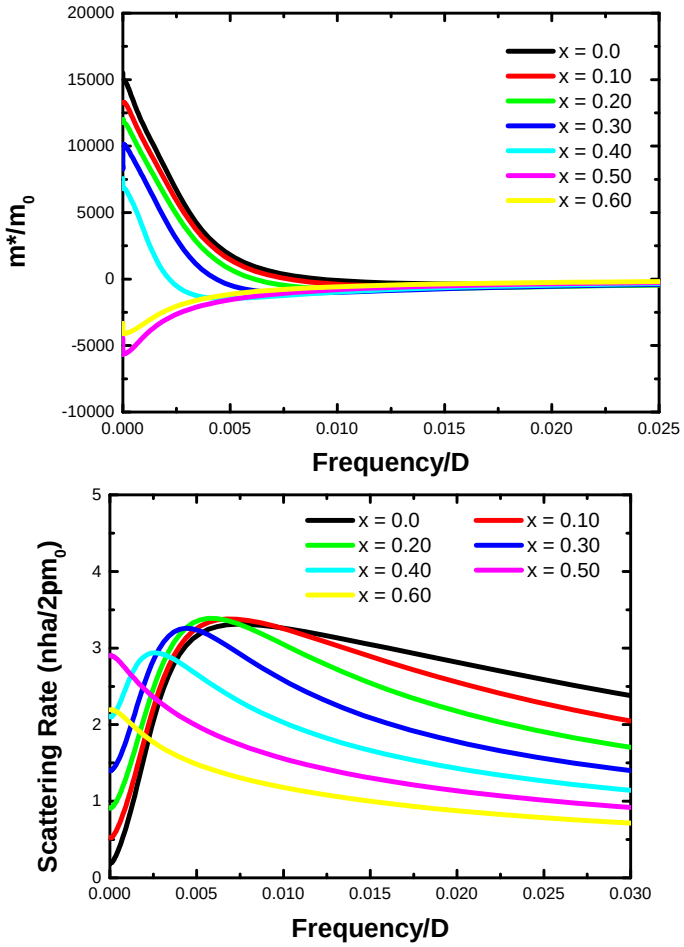

Figure 5.16: *(Upper figure) Effective mass enhancement m^*/m_0 of the c-electron as a function of frequency at zero temperature and several different impurity concentrations in the PM phase. For sufficiently high impurity concentration, the effective mass changes its sign. Therefore, the negative effective mass can be used as a signal indicating the localization of charge carriers. (Lower figure) Scattering rate of the c-electron as a function of frequency at zero temperature and several different impurity concentrations in the PM phase. For sufficiently high impurity concentration, low frequency scattering dominates.*

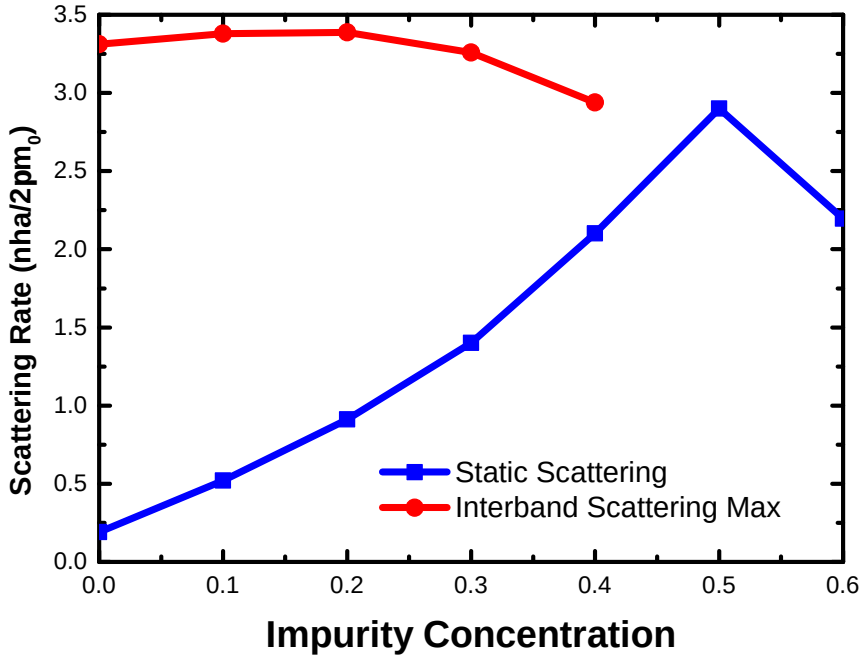

Figure 5.17: *Static scattering rate (blue squares) and maximum interband scattering rate (red circles) as a function of impurity concentration. It can be seen clearly that for sufficiently high impurity concentration, static scattering process dominates the system and the system loses lattice coherence.*

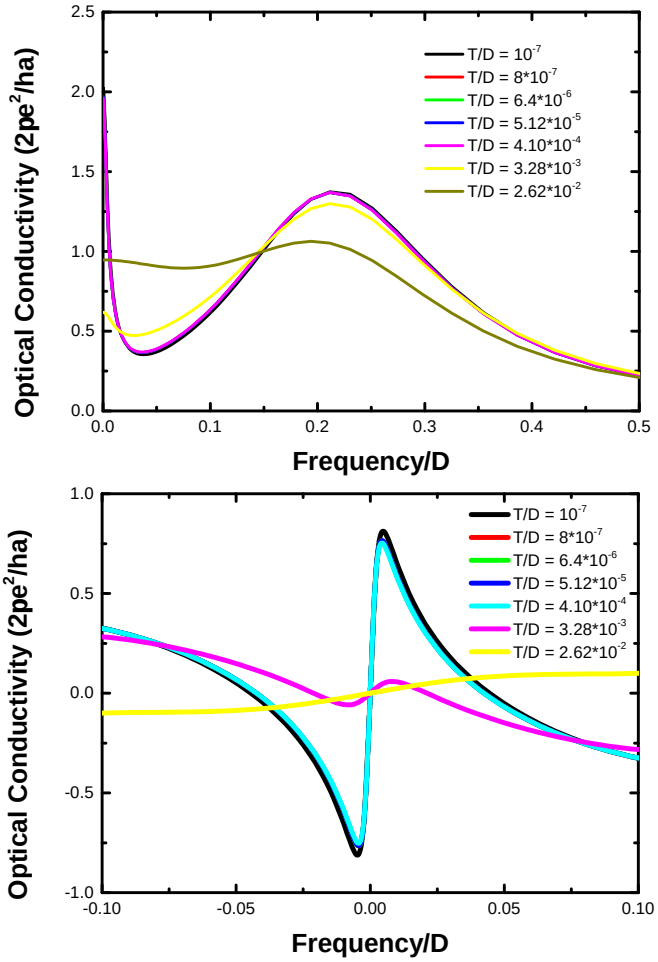

Figure 5.18: *(Upper figure) Real part of the optical conductivity $\sigma(\omega)$ of the c-electron as a function of frequency at impurity concentration $x = 0.0$ and several different temperatures in the AFM phase. A strongly renormalized Drude peak is developed at low temperature at zero frequency. By increasing temperature, the sharp Drude peak disappears and the high temperature $\sigma_1(\omega)$ can be fitted by the classical Drude model. (Lower figure) Imaginary part of the optical conductivity $\sigma(\omega)$ of the c-electron as a function of frequency at impurity concentration $x = 0.0$ and several different temperatures in the AFM phase. At low temperature there is a strong absorption at zero frequency. At first glance, we might think there is no difference beween the optical conductivities in the PM and AFM phases.*

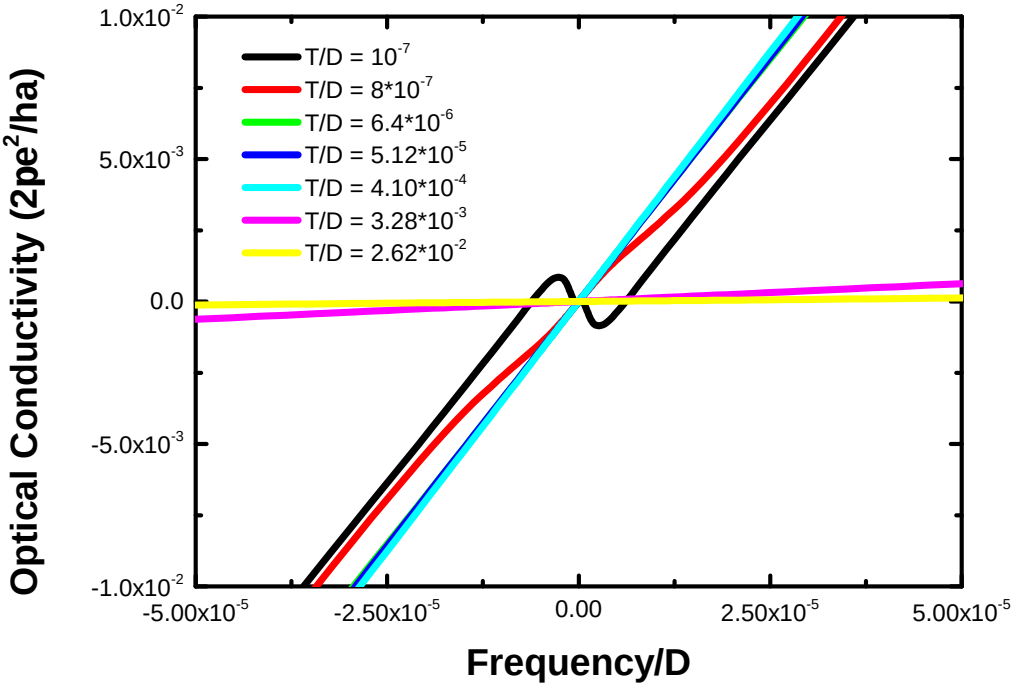

Figure 5.19: *Imaginary part of optical conductivity $\sigma(\omega)$ of c-electron as a function of frequency at impurity concentration $x = 0.0$ and several different temperatures in the low frequency regime in the AFM phase. An extra absorption appears close to the Fermi level. This excitation has an energy scale $\frac{\omega}{D} \sim 10^{-5}$.*

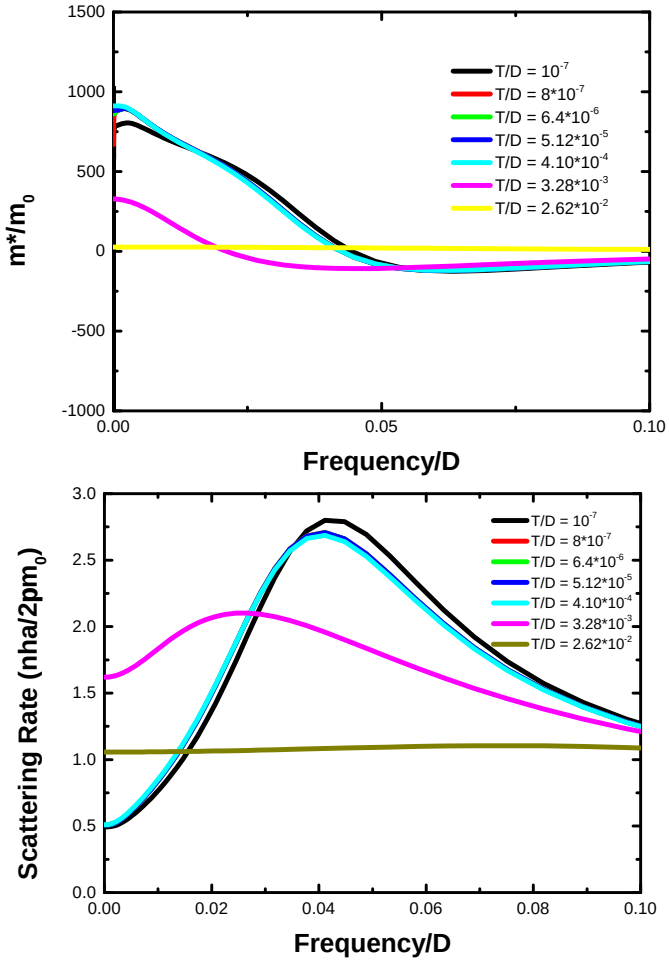

Figure 5.20: *(Upper figure) Effective mass enhancement m^*/m_0 of the c-electron as a function of frequency at impurity concentration $x = 0.0$ and several different temperatures in the AFM phase. The negative effective mass can be interpreted as an absorption of the bound state. (Lower figure) Scattering rate of the c-electron as a function of frequency at impurity concentration $x = 0.0$ and several different temperatures in the AFM phase. The position of the maximum of the scattering rate coincides with the onset of the mass renormalization. Therefore, this strong scattering process can be interpreted as the coherent dynamical Kondo scattering. Similar to the scattering rate in the PM phase, the Kondo spin flip also loses its temporal coherence by increasing temperature and becomes incoherent above lthe attice coherence temperature.*

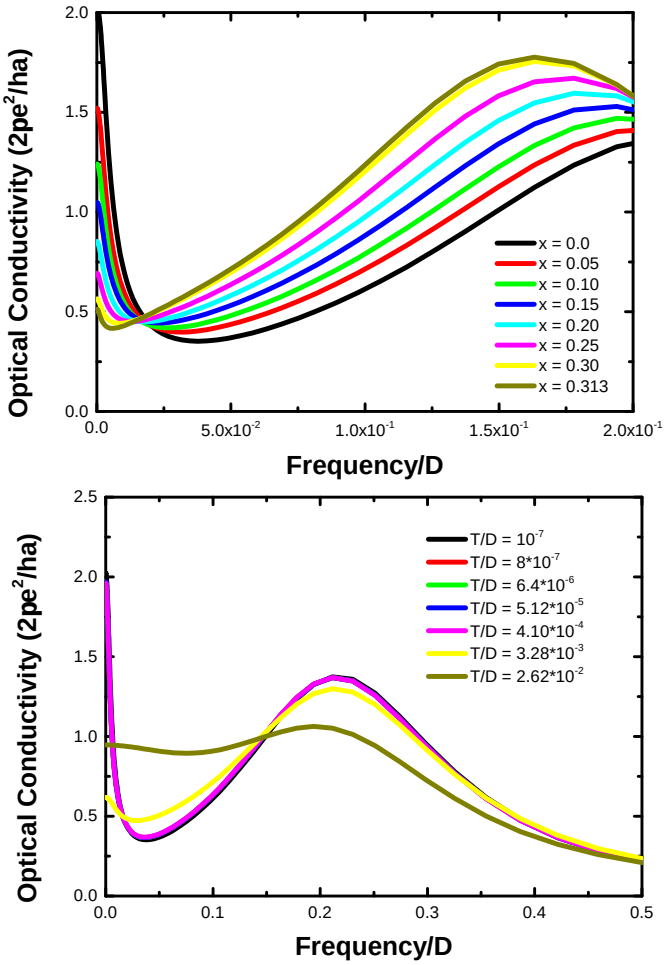

Figure 5.21: *(Upper figure) Real part of the zero temperature optical conductivity $\sigma(\omega)$ of the c-electron as a function of frequency at several different impurity concentrations in the AFM phase. A strongly renormalized Drude peak is developed at low temperature at zero frequency. Increase in the impurity concentration makes the system more insulator like and decreases the energy of the interband transition. (Lower figure) Imaginary part of the zero temperature optical conductivity $\sigma(\omega)$ of the c-electron as a function of frequency at several different impurity concentrations in the AFM phase. Zero frequency absorption becomes weaker by increasing the impurity concentration. This can be interpreted as loss of lattice coherence with respect to increase in the impurity concentration.*

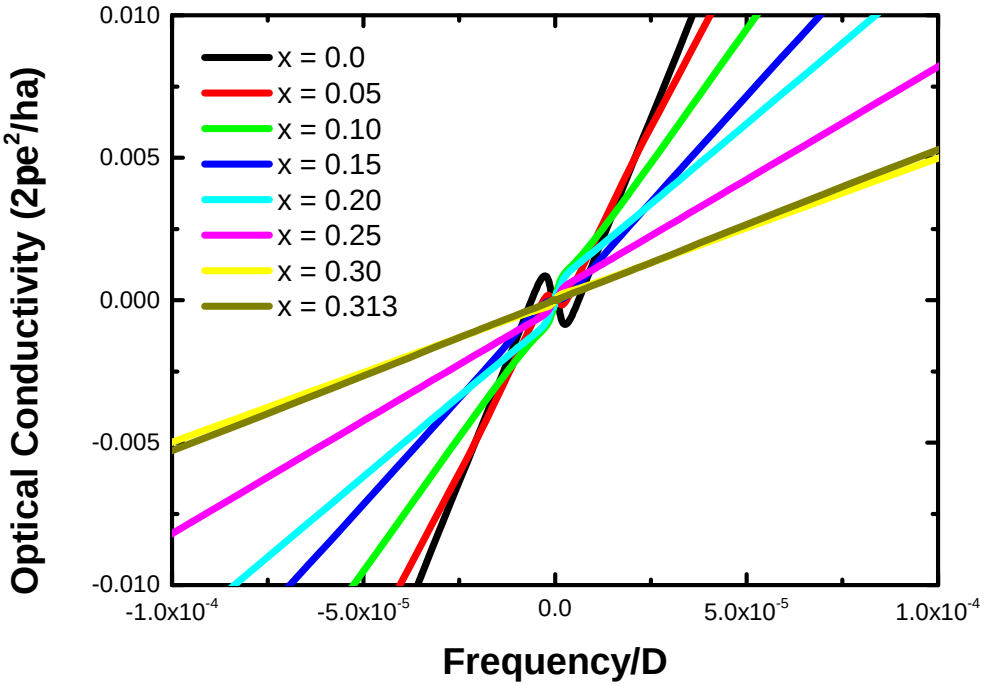

Figure 5.22: *Imaginary part of the optical conductivity $\sigma(\omega)$ of the c-electron as a function of frequency at several different impurity concentration x in the low frequency regime in the AFM phase. Extra absorption appears close to the Fermi level. The absorption becomes weaker by increasing the impurity concentration.*

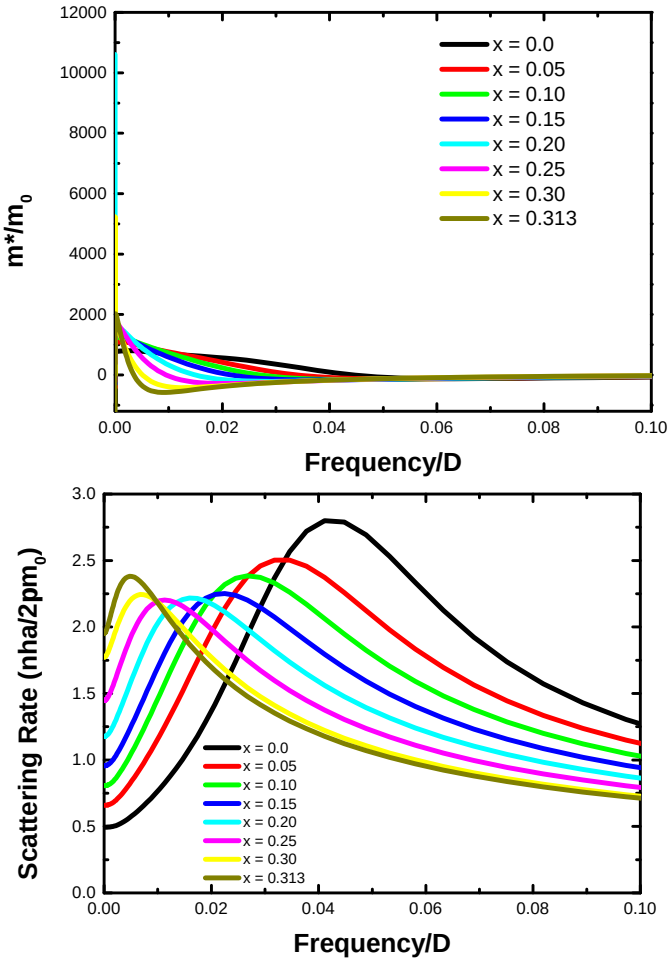

Figure 5.23: *(Upper figure) Effective mass enhancement m^*/m_0 of the c-electron as a function of frequency at several different impurity concentration x in the AFM phase. (Lower figure) Scattering rate of the c-electron as a function of frequency at several different impurity concentration x in the AFM phase. The evolution of the scattering rate suggests the the Kondo exchange become more static close to the QCP. However, some coherent dynamical component still exists.*

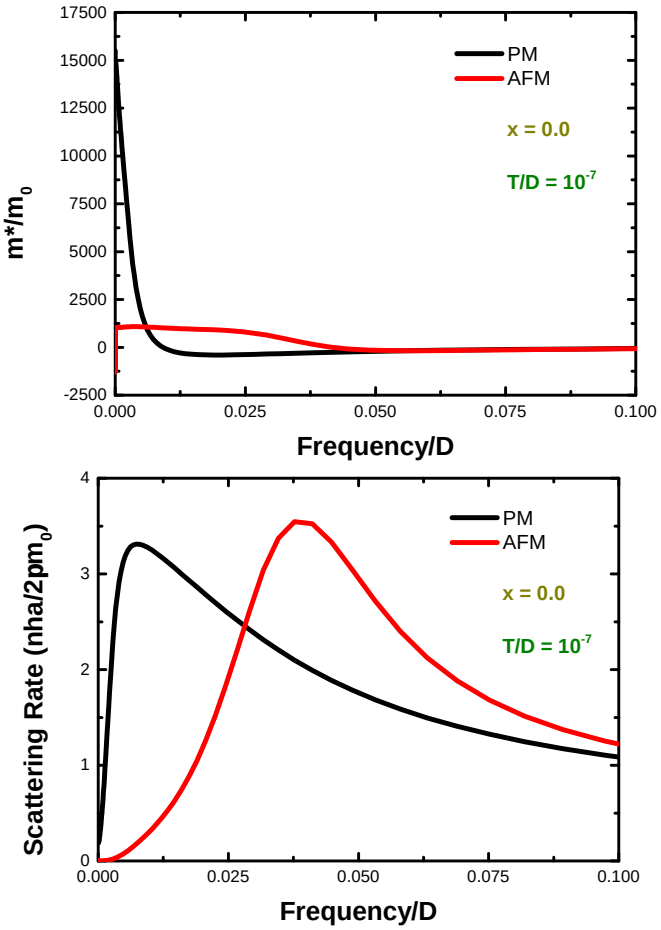

Figure 5.24: *(Upper) Effective mass m^*/m_0 enhancement in PM and AFM phases at zero temperature and impurity concentration $x = 0$. The mass renormalization in the AFM phase is about one order of magnitude smaller than that in the PM phase. (Lower) Scattering rate in the PM and the AFM phases at zero temperature at impurity concentration $x = 0$. The interband scattering rate is sharper in the AFM phase. By having a relatively large gap, the Kondo exchange in the AFM phase takes place at a much higher frequency than that in the PM phase.*

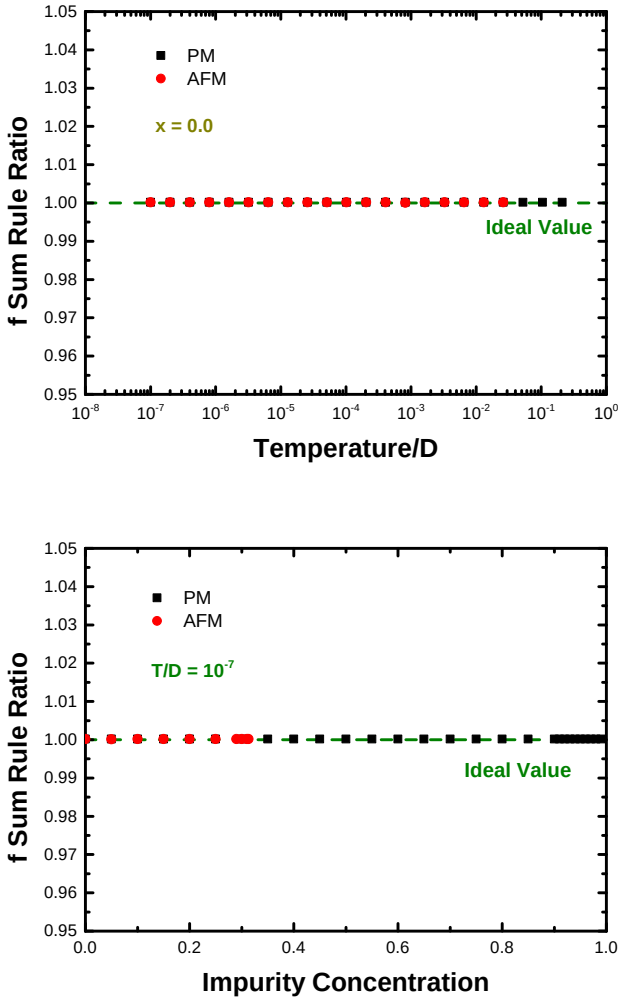

Figure 5.25: *(Upper figure) f-sum rule is checked as a function of temperature at impurity concentration $x = 0$ in both the PM and the AFM phases. (Lower figure) f-sum rule is checked as a function of the impurity concentration x at zero temperature in both the PM and the AFM phases. The results show that our results perfectly satisfy the f-sum rule.*

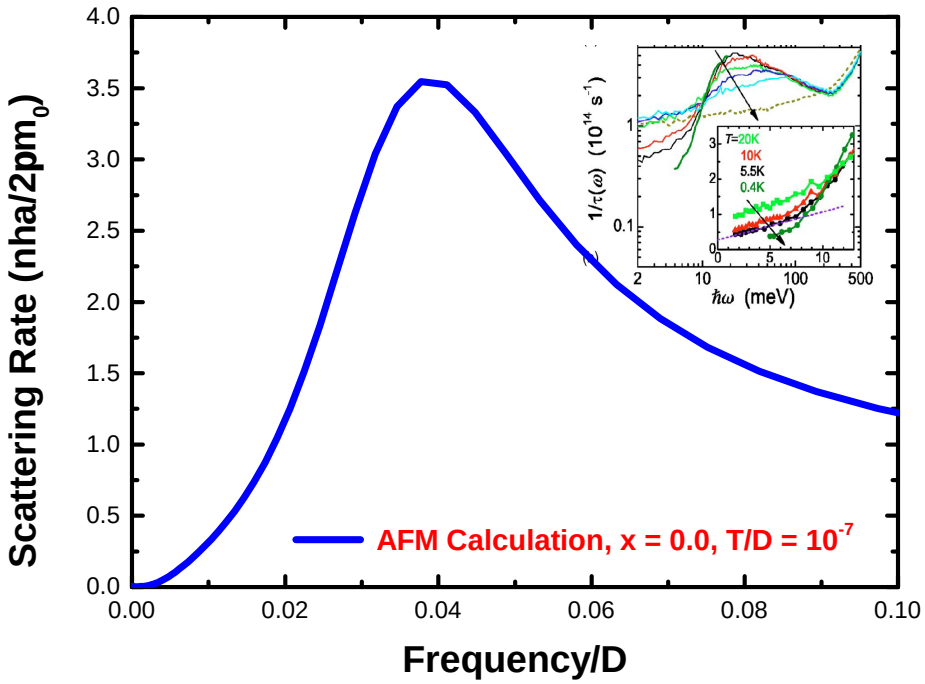

Figure 5.26: *Scattering rate in the AFM phase at zero temperature and zero impurity concentration. For a typical heavy fermion system,* $\frac{nha}{2\pi m_0}$ *is of order* $2.9 * 10^{14}(s^{-1})$*. The experiment shows that the maximum of scattering rate of* YRh_2Si_2 *is* $5 * 10^{14}(s^{-1})$ *and the result from numerical gives* $10^{13}(s^{-1})$*. The inset is taken from [17].*

5.4.4 Comparison to the experiment

How reasonable are the results of the calculation? Fortunately, experimental data of scattering rate of the heavy fermion system YRh_2Si_2 is available [17]. For a heavy fermion system, the factor $\frac{nha}{2\pi m_0}$ is of the order of $2.9 * 10^{14}(s^{-1})$ and Fig.(5.26) shows that both the behavior and the order of magnitude agree well with that of the experiment.

Chapter 6
6 Scaling of QCP

Close to the critical point, long wavelength fluctuations determine the behavior of the systems. It is a surprise to see that very different systems can be described by the same set of parameters which are called critical exponents. For example, the liquid-gas critical phase transition and the mean field Ising model share the same critical exponents. Each set of parameters represents a *universality class*. This phenomena can be interpreted as the details of the system become irrelevant and only macroscopic properties are important. Theoretically critical exponents appears in two ways: first, the power laws of physical quantities because there is no typical length scales close to a critical point; second, the scaling law in which there is a typical length scale and the exponents are connected by the hyperscaling laws. For a system with effective dimensionality above (not including equal) the upper critical dimension, mean field theory dominates and the scaling laws are not necessarily valid. Scaling laws automatically guarantee power laws but not the other way round.

The framework of DMFT + CPA has a root in the mean field theory; therefore, scaling laws do not necessarily hold. However, in experiment scaling like behavior in quantum critical antiferromagnets $CeCu_{5.9}Au_{0.1}$ was observed [18]. While the upper critical dimension of the corresponding quantum critical point is unknown, the effective dimensionality are very likely to exceed it due to the existence of the dynamical exponent. This is the case at least for the known Hertz-Millis theory of quantum critical points. As a result, it is possible that $CeCu_{5.9}Au_{0.1}$ has a mean field quantum critical point. Therefore, we calculate experimentally measurable quantities in the quantum critical regime and analyze them by the scaling hypothesis of magnetization:

$$M\left(B,x,T\right)=b^{-\frac{\beta}{\nu}}M\left(b^{y}B,b^{\frac{1}{\nu}}x,b^{z}T\right) \tag{6.1}$$

with B the conjugate field to the AFM ordering, x the impurity concentration relative to the QCP, and T the temperature. Magnetization is defined as the difference between spin up and spin down occupation number on f-electron state:

$$M\equiv\frac{\left|n_{\uparrow}^{f}-n_{\downarrow}^{f}\right|}{2} \tag{6.2}$$

To discuss QCP that can be reached by changing impurity concentration x, we set $B=T=0$:

$$M\left(x\right)=b^{-\frac{\beta}{\nu}}M\left(b^{\frac{1}{\nu}}x\right) \tag{6.3}$$

Because b is a free parameter, we choose $\left(b^*\right)^{\frac{1}{\nu}} x = 1$ such that

$$M(x) = x^{\beta} M(1) \tag{6.4}$$

The power law of the susceptibility as a function of conjugate field can be measured by applying a staggered magnetic field ($\mathbf{q} = \mathbf{Q}$ with $\mathbf{Q}$ the antiferromagnetic wave vector) at QCP at zero temperature:

$$\begin{aligned} \chi(B) &\equiv \frac{\partial M(B)}{\partial B} \\ &= b^{-\frac{\beta}{\nu}+y} \chi\left(b^y B\right) \end{aligned} \tag{6.5}$$

This time we choose $\left(b^*\right)^y B = 1$:

$$\chi(B) = B^{\frac{\beta}{y\nu}-1} \chi(1) \equiv B^{\frac{1}{\delta}-1} \chi(1) \tag{6.6}$$

By including temperature, Eq.(6.5) becomes

$$\chi(B,T) = b^{-\frac{\beta}{\nu}+y} \chi\left(b^y B, b^z T\right) \tag{6.7}$$

Again, by choosing $\left(b^*\right)^y B = 1$, we have

$$\chi(B,T) = B^{\frac{1}{\delta}-1} \chi\left(1, \frac{T}{B^{\frac{z\nu}{\delta\beta}}}\right) \equiv B^{\frac{1}{\delta}-1} \Phi\left(\frac{T}{B^{\kappa}}\right) \tag{6.8}$$

By applying data collapse on susceptibility, κ can be obtained. By fitting our data, β, δ, and κ can be obtained and we assume they may be used to calculate the exponents shown in Eq.(6.1). However, Eq.(6.1) may not be true. To avoid confusion, we should bear in our mind that those power laws are hold and Eq.(6.8) is observed in the experiment and we want to test our results with it. In the following section, it will be shown how to obtain the exponents from the results of our numerical simulation and experiment.

6.1 Order Parameter Scaling

First we measure β from the magnetization close to the QCP shown in Fig.(6.1). To fit the data, both sides of Eq.(6.4) are taken logarithmically:

$$\log_{10} M = \beta \log_{10}(x_c - x) + \alpha \tag{6.9}$$

Linear regression is applied to minimize

$$Q = \sum_i \left(\log M_i - \alpha - \beta \log(x_c - x)\right) \tag{6.10}$$

and we obtain

$$\beta_{best} = 0.4910 \pm 0.0300, \tag{6.11}$$

with 95% confidence level and

$$x_c = 0.3160 \tag{6.12}$$

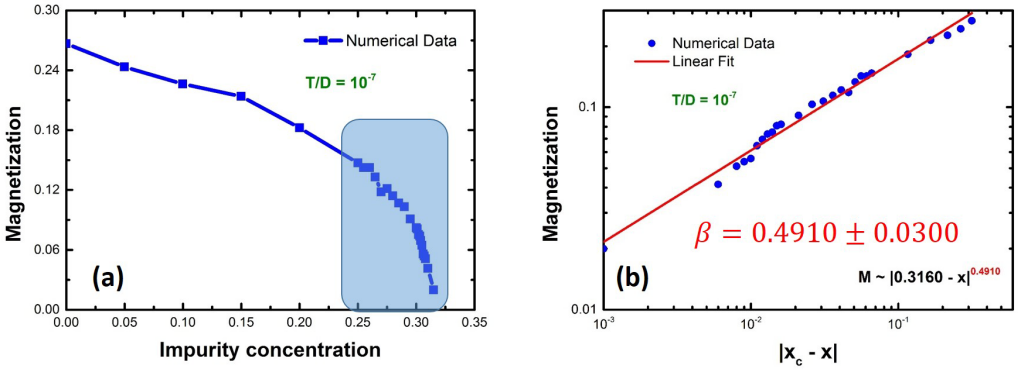

Figure 6.1: *(a) Magnetization M as a function of impurity concentration x at zero temperature. (b) Magnetization is fitted by $\log_{10} M = \beta \log_{10} |x_c - x| + \alpha$ with data points from the encircled region, critical exponent β, critical concentration x_c . Magnetization is successfully fitted with $\beta = 0.4910 \pm 0.0300$ with 95% confidence level and $x_c = 31.60\%$.*

Here we see that the obtained β is the result of mean field $\beta_{MF} = 0.5$. The linear regression fit can be seen in the inset of Fig.(6.1). The obtained QCP indicates a AFM phase surviving up to 30% of non-magnetic impurity doping concentration. Our result suggests two possible explanations for this robust AFM phase. First, the development of lattice coherence reduces the sensitivity to substitution of magnetic atoms with non-magnetic atoms; second, mean field approximation suppresses spatial fluctuations and overly estimates the critical concentration. In the following calculations we choose non-magnetic impurity concentration at $x^* = 31.56\%$. To investigate the properties of the QCP, a staggered magnetic field is applied to the system at concentration x^*.

In Fig.(6.2) we show staggered susceptibility χ_s as a function of temperature and magnetic field. It can be seen that the susceptibility increases with respect to decrease in magnetic field at low temperature and it is magnetic field independent at high temperature. Its empirical behavior at low temperature is consistent with the divergence behavior indicated by power law, while the high temperature behavior is consistent with Curie-Weiss law. To show that our result satisfies the power law behavior with respect to conjugate field, we measure critical exponent δ by investigating susceptibility at low temperature.

Fig.(6.3) shows the susceptibility as a function of staggered magnetic field at zero temperature. The data is fitted by taking both sides of Eq.(6.6) logarithmically:

$$\log_{10} \chi\left(B\right) = \left(\frac{1}{\delta} - 1\right) \log_{10} B + C \tag{6.13}$$

with C a constant. The fitting shows that

$$\frac{1}{\delta} - 1 = -0.7368 \pm 0.0050 \tag{6.14}$$

with 95% confidence level. The resulting $\delta = 3.7994 \pm 0.0722$ which is much larger than what is expected from mean field theory $\delta_{MF} = 3$. It is clear from Fig.(6.4) that the critical exponent of

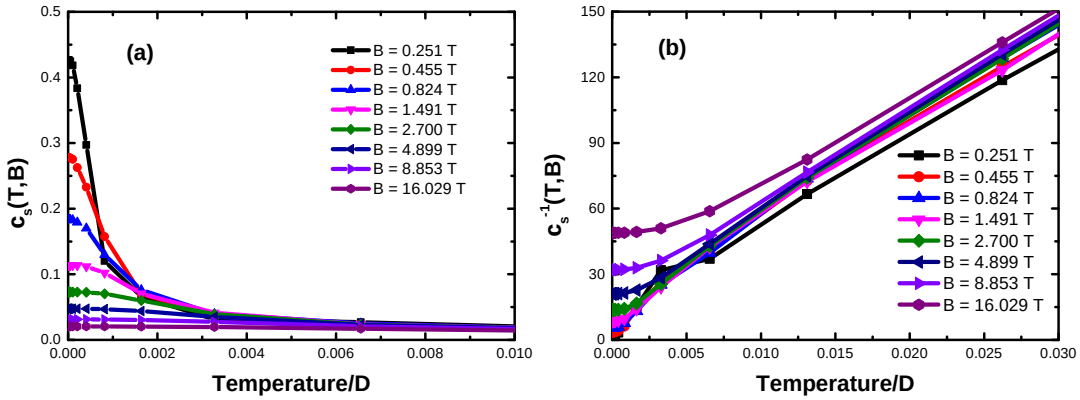

Figure 6.2: *(a) Staggered susceptibility χ_s as a function of temperature and magnetic field at $x^* = 31.56\%$. By decreasing magnetic field, susceptibility increases. (b) Inverse susceptibility χ_s^{-1} as a function of temperature and magnetic field at $x^* = 31.56\%$. Considering that the magnetic field extends over two order of magnitude, high temperature susceptibility can be considered as magnetic field independent.*

zero temperature susceptibility $\chi_s\left(T=0,B\right)$ cannot be δ_{MF}. This result might be due to either NRG systematic error or the QCP is a non-Gaussian fixed point.

To the end of the section, we want to obtain the universal function Φ_s of susceptibility by obtaining κ. To obtain κ in Eq.(6.8) data collapse is applied on susceptibilities subjected to various staggered magnetic fields ranging from 0.25T to 16T by minimizing the following quantity:

$$\sum_{ij}\left[\log_{10}\left(B_i^{1-\frac{1}{\delta}}\chi\left(\frac{T}{B_i^{\kappa}}\right)\right)-\log_{10}\left(B_j^{1-\frac{1}{\delta}}\chi\left(\frac{T}{B_j^{\kappa}}\right)\right)\right] \tag{6.15}$$

Because the magnitude of susceptibility at different temperatures is over three decades, logarithm is used to balance the weight of contribution to Eq.(6.15). The obtained κ which minimizes Eq.(6.15) is

$$\kappa = 0.8501. \tag{6.16}$$

Combining Eq.(6.8) and Eq.(6.14), we obtain

$$\chi\left(B,T\right) = B^{-0.7368}\Phi_s\left(\frac{T}{B^{0.8501}}\right). \tag{6.17}$$

The result of data collapse is shown in Fig.(6.5). The equation above suggests that in the high temperature region in which susceptibility is magnetic field independent, susceptibility follows a modified Curie-Weiss law:

$$\chi\left(T\right) \sim \frac{1}{T^{0.8667}} \tag{6.18}$$

These critical exponents should be tested by experimental measurements. However, the magnetic field used here is a staggered magnetic field which can be produced by neutron wave but is difficult to be carried out in practice. As a result, in the next section a uniform magnetic field is applied such that our results are experimentally measurable.

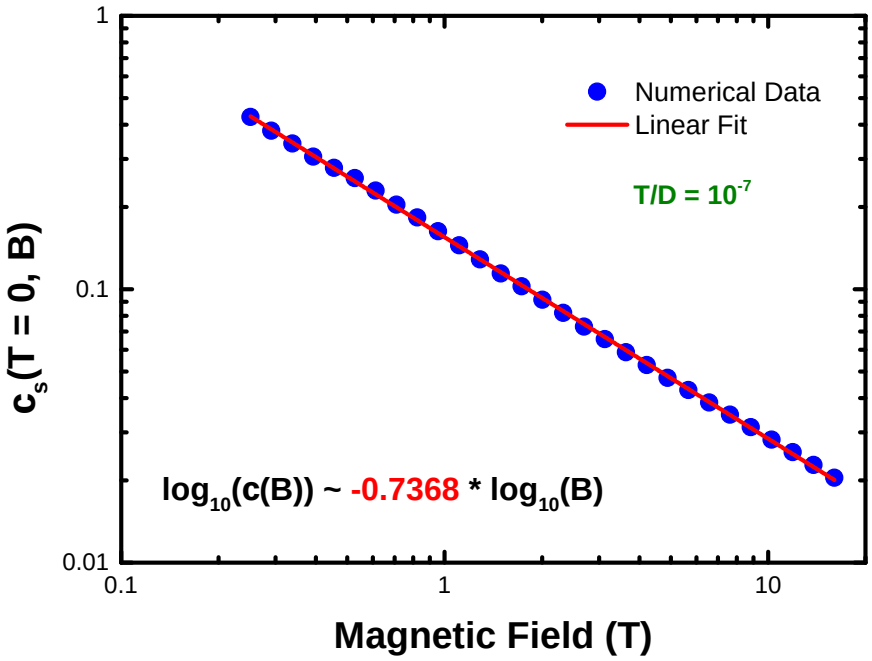

Figure 6.3: *Staggered susceptibility χ_s as a function of magnetic field at zero temperature at $x^* = 31.56\%$. χ_s versus B is shown in a log-log plot. It demostrates that $\chi_s(B)$ satisfies power law $\chi_s(B) \sim B^{\frac{1}{\delta}-1}$. Linear regression gives the critical exponent $\delta = 3.7994 \pm 0.0722$ with 95% confidence level.*

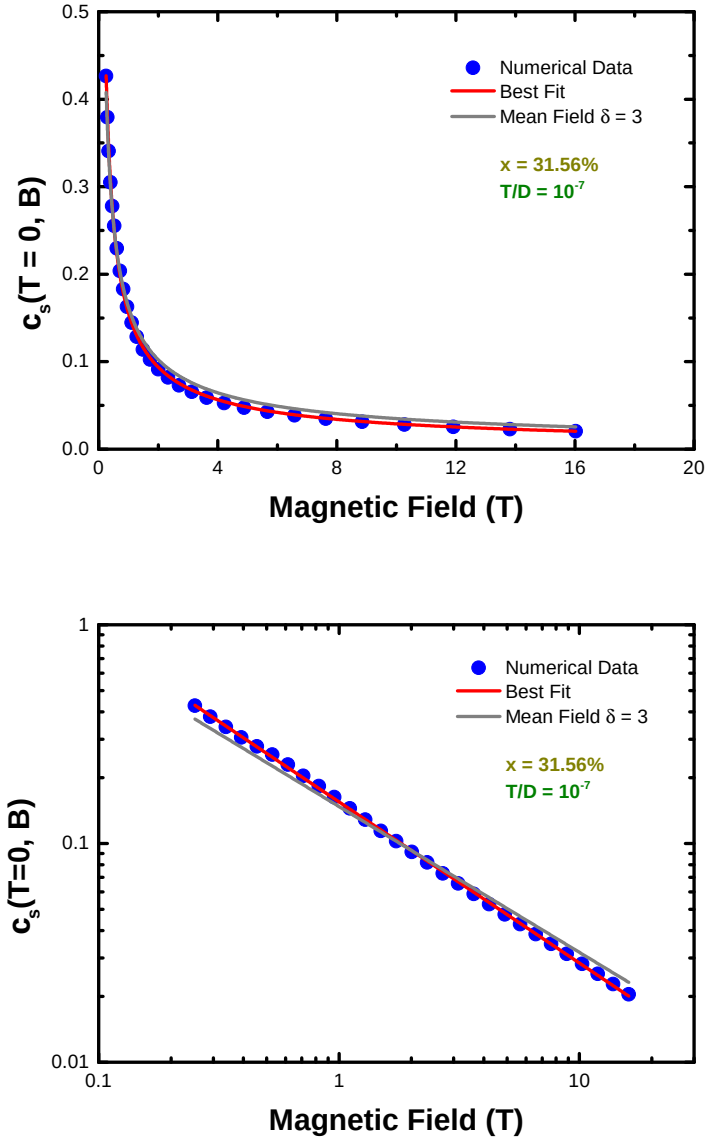

Figure 6.4: *Staggered susceptibility* $\chi_s\left(T=0,B\right)$ *at* $x^* = 31.56\%$ *is fitted with* $\delta = 3.7994$ *(red line) and* $\delta_{MF} = 3$ *(gray line), respectively. Apparantly* $\chi_s\left(T=0,B\right) \sim B^{\frac{1}{\delta}-1}$ *cannot be fitted with* $\delta = \delta_{MF}$*. This result might be due to either NRG systematic error or the QCP is a non-Gaussian fixed point.*

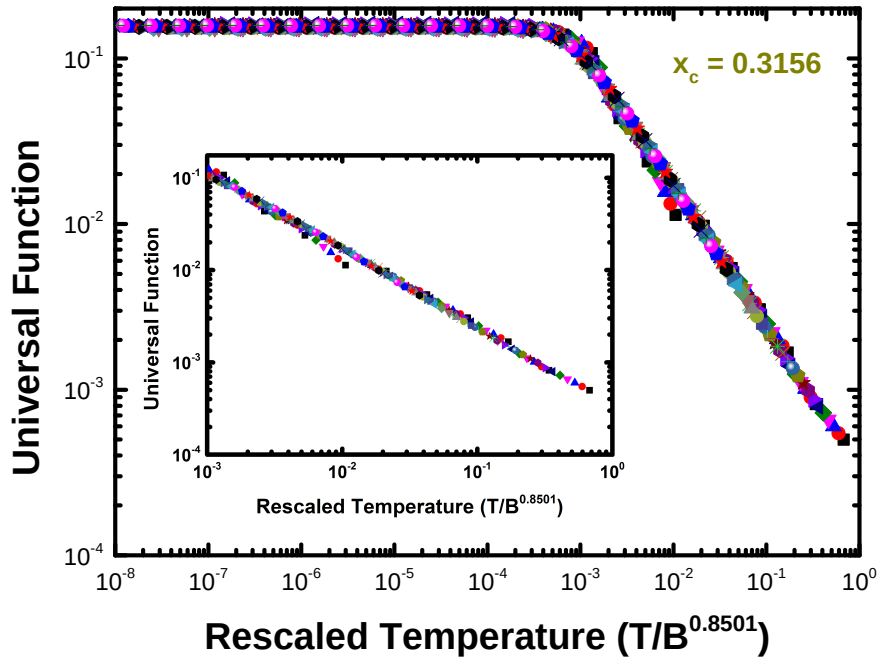

Figure 6.5: *Universal function Φ_s as a function of properly rescaled temperature T/B^{κ} with staggered magnetic field B ranging from 0.25T to 16T. Φ_s can be successfully obtained by rescaling $\chi_s\left(T,B\right)$ by $B^{1-\frac{1}{\delta}}\chi_s\left(\frac{T}{B^{\kappa}}\right)$ with $\delta = 3.7994$ and $\kappa = 0.8501$. This result implies a modified Curie-Weiss law $\chi_s\left(T\right) \sim T^{-0.8667}$ at high temperature.*

6.2 Uniform Susceptibility

Fig.(6.6) shows the zero temperature susceptibility which also increases with respect to decrease in magnetic field. Since uniform magnetic field is not conjugated to the ordering parameter, neither the scaling law nor power law hold in general. However, the uniform susceptibility χ_u ($\mathbf{q} = 0$) of AFM system $CeCu_{5.9}Au_{0.1}$ at QCP can be connected to staggered susceptibility χ_s via a constant [18, 100]:

$$\chi_u^{-1} - \chi_0^{-1} = \chi_s^{-1} \tag{6.19}$$

Therefore, we also assume that Eq.(6.19) holds for our system and test if this relation is valid in our case. From the scaling law of χ_s shown in Eq.(6.8), Eq.(6.19) becomes

$$\frac{1}{\chi_u^{-1} - \chi_0^{-1}} = B^{\frac{1}{\delta^*}-1}\Phi\left(\frac{T}{B^{\kappa^*}}\right) \tag{6.20}$$

At zero temperature Eq.(6.20) becomes

$$\frac{1}{\chi_u^{-1} - \chi_0^{-1}} \sim B^{\frac{1}{\delta^*}-1} \tag{6.21}$$

and linear regression

$$\log_{10}\left(\chi_u^{-1} - \chi_0^{-1}\right) = \left(1 - \frac{1}{\delta^*}\right)\log_{10} B + C \tag{6.22}$$

is applied to find χ_0^{-1} and critical exponent δ^*. The result is shown in Fig.(6.7) with

$$1 - \frac{1}{\delta^*} = 0.7393 \pm 0.0087 \tag{6.23}$$

and $\chi_0^{-1} = 3.0281$. Our result $\delta^* = 3.8358 \pm 0.1280$ suggests that there is no significant difference between critical exponents δ and δ^*. To this end, data collapse base on Eq(6.15) and Eq.(6.20) is used to obtain κ^* and the universal function Φ_u with uniform magnetic field. The result is shown in Fig.(6.8) and κ^* which optimizes the data collapse is

$$\kappa^* = 0.9522. \tag{6.24}$$

As a result, the uniform susceptibility satisfies the equation

$$\frac{1}{\chi_u^{-1} - 3.0281} = B^{-0.7393}\Phi_u\left(\frac{T}{B^{0.9522}}\right) \tag{6.25}$$

This equation gives us several interesting results. First, the T/B scaling which is observed at the local quantum critical point [18], at which both the Néel temperature and the onset energy scale E^*_{loc} of static Kondo singlet vanishes. At high temperature, when the susceptibility is magnetic field independent, Eq.(6.8) can be written as

$$\chi_u^{-1}(T) = \frac{T^{0.7764}}{C} + 3.0281 \tag{6.26}$$

which suggests a modified Curie-Weiss law, similar to the staggered field susceptibility. This high temperature behavior shows the most interesting result of this thesis: the exponent of temperature is consistent with that of $CeCu_{5.9}Au_{0.1}$ [18], whose corresponding exponent is reported as 0.75 ± 0.05. While quantum Monte Carlo simulations in which the local moment is connected to both fermionic bath (Kondo coupling) and bononic bath (RKKY interaction), suggests the exponent be 0.72 [25].

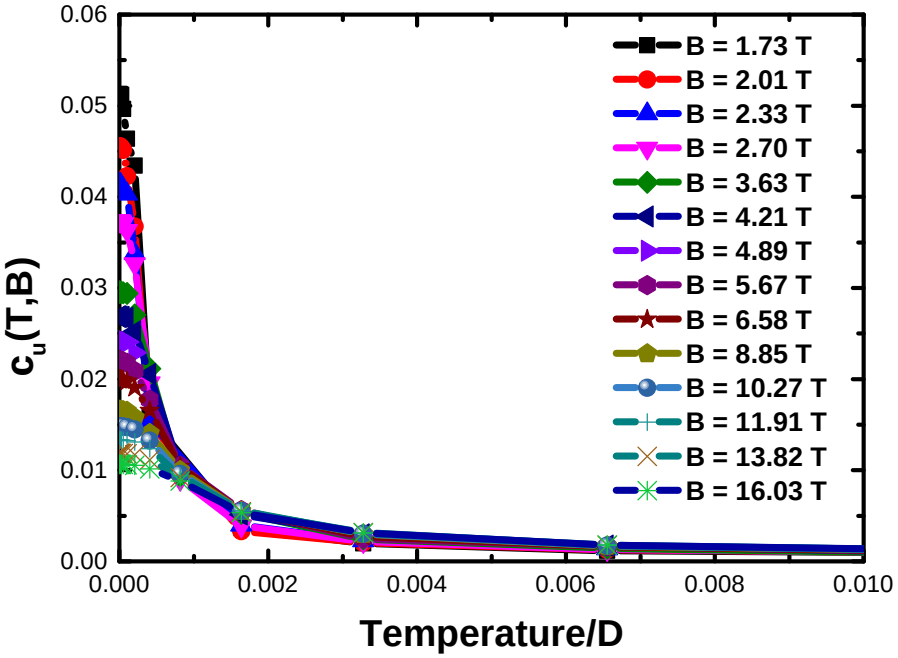

Figure 6.6: *Uniform susceptibility χ_u as a function of temperature and magnetic field at $x^* = 31.56\%$. By decreasing temperature, susceptibility increases.*

6.3 Discussion

If the results are examed more carefully, we found that our susceptibility is much more temperature sensitive as can be seen in Fig.(6.9). This suggests an effectively small g-factor in our system. But we should bear in mind there are some fundamental differences between these two systems. In our system, cerium spins are removed by impurities. While in the $CeCu_{6-x}Au_x$ the spins remain intact. Here we predict that in the quantum critical regime, the g-factor of the $Ce_{1-x}La_xCu_2Ge_2$ should be small and there is the local scaling.

Based on the critical exponents obtained from the previous sections, we are able to calculate other critical exponents which can also be probed from the experiements. It is reported that in local quantum critical AFM system $YbRh_2\left(Si_{0.95}Ge_{0.05}\right)_2$, the Grüneisen ratio has a power law temperature dependence

$$\Gamma = \frac{1}{T^x} \tag{6.27}$$

with $x = \frac{1}{z\nu} = 0.7 \pm 0.1$ [27] below 0.3K. It is also reported that in the field induced quantum critical system $YbRh_2Si_2$ magnetic Grüneisen ratio is 0.75 [24, 26]. In our numerical simulation, based on the obtained κ, β, and δ we have

$$x = \frac{1}{z\nu} = \begin{cases} 0.6306 \pm 0.0403 & \mathbf{q} = \mathbf{Q} \\ 0.5576 \pm 0.0388 & \mathbf{q} = \mathbf{0} \end{cases} \tag{6.28}$$

which is in good agreement with the experiment.

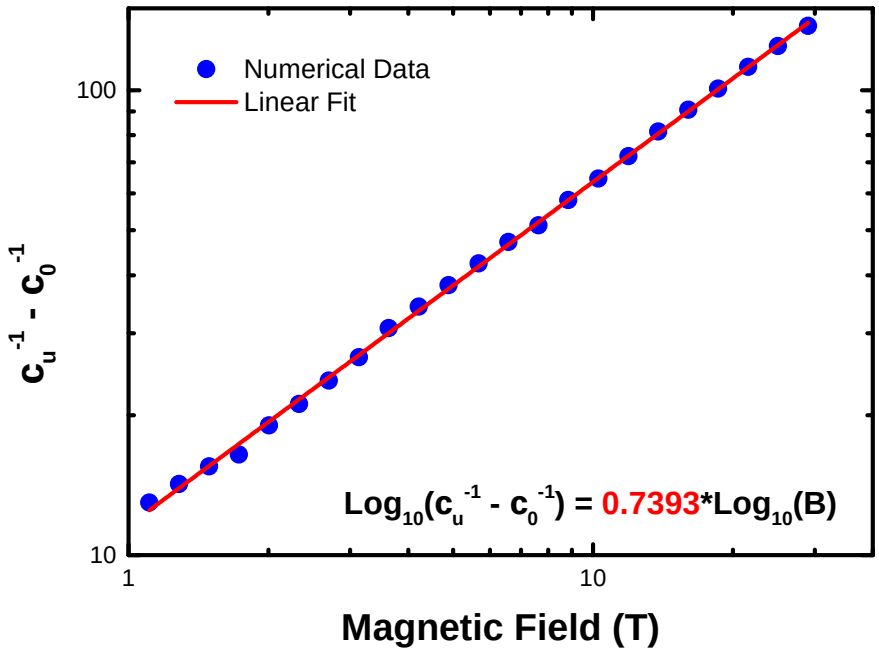

Figure 6.7: *Uniform susceptibility χ_u as a function of magnetic field at zero temperature and $x^* = 31.56\%$. Because uniform magnetic field is not the conjugate field of the AFM order parameter, the uniform susceptibility does not follow scaling laws in general. Here power law for zero temperature χ_u is used: $\frac{1}{\chi_u^{-1} - \chi_0^{-1}} \sim B^{\frac{1}{\delta^*} - 1}$ [18]. Linear regression gives critical exponent $\delta^* = 3.8358 \pm 0.1280$.*

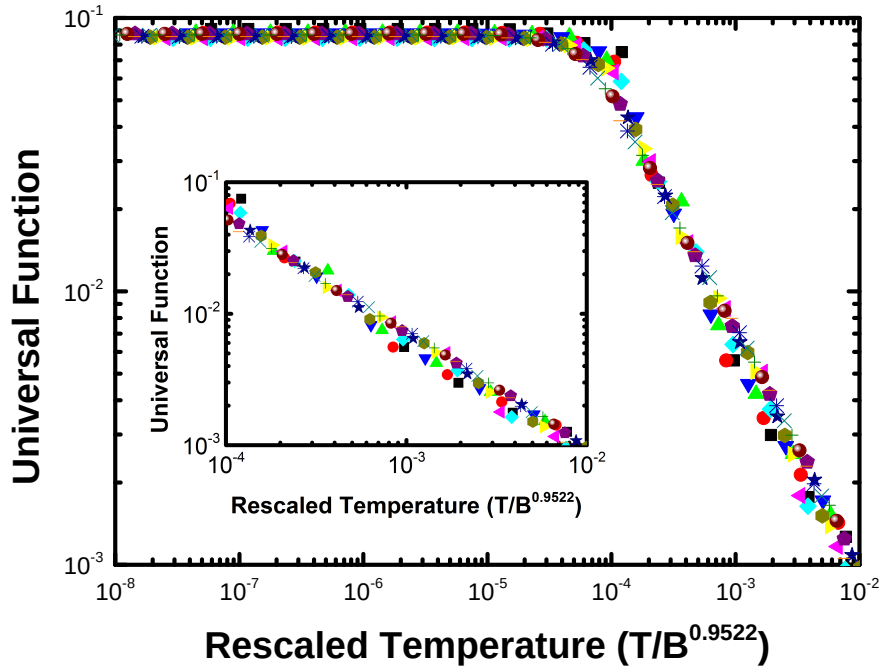

Figure 6.8: *Universal function* Φ_u *as a function of properly rescaled temperature* T/B^{κ^*} *with uniform magnetic field* B *ranging from 1.73T to 16T.* Φ_u *can be successfully obtained by rescaling* $\chi_u\left(T,B\right)$ *by* $B^{1-\frac{1}{\delta^*}}\left(\chi_u^{-1}\left(\frac{T}{B^{\kappa}}\right)-\chi_0^{-1}\right)^{-1}$ *with* $\delta^*=3.8358$ *and* $\kappa^*=0.9522$. *This result implies a modified Curie-Weiss law* $\chi_u\left(T\right)\sim T^{-00.7764}$ *at high temperature.*

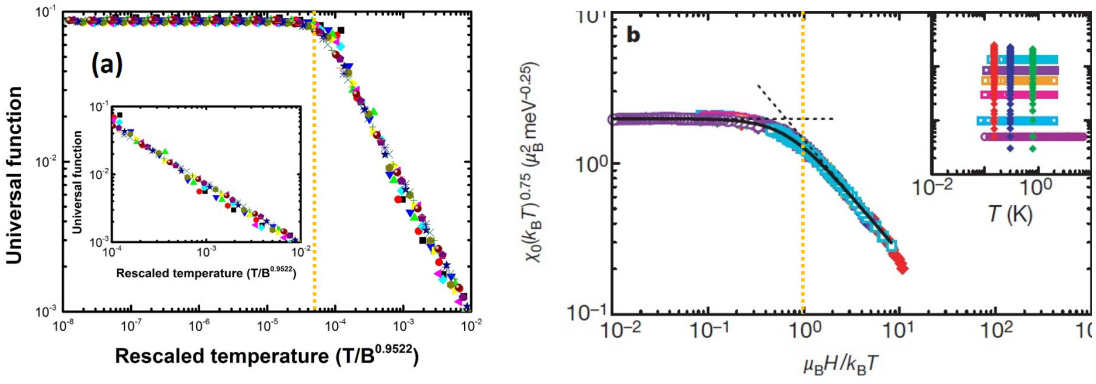

Figure 6.9: *From these two pictures, we see that susceptibility from the calculation is much more temperature sensitive compared with that of $CeCu_{6-x}Au_x$ (Fig.(b)) [18]. There are fundamental differences between $Ce_{1-x}La_xCu_2Ge_2$ and $CeCu_{6-x}Au_x$. In $Ce_{1-x}La_xCu_2Ge_2$, cerium spins are removed by impurities. While in the $CeCu_{6-x}Au_x$ the spins remain intact.*

Here we see that the differences between our critical exponents at two different antiferromagnetic wave vectors are very small. As a result, it can be assumed that critical exponents are wave vector independent and the obtained quantum critical point is a local quantum critical point (LQCP). Hence, our result suggests that heavy femion AFM LQCP can be described by PAM.

We would like to investigate the dimensionality z of temporal dimension in both cases of staggered and uniform magnetic field. Because this is a mean field calculation, it is assumed that $\nu = \nu_{MF} = \frac{1}{2}$. From Eq.(6.8), it follows that

$$\begin{aligned} z &= \frac{\kappa\delta\beta}{\nu} \\ &= \begin{cases} 3.1717 \pm 0.2029 & \mathbf{q} = \mathbf{Q} \\ 3.5867 \pm 0.2497 & \mathbf{q} = \mathbf{0}. \end{cases} \end{aligned} \tag{6.29}$$

Next we give our predictions for the exponents of specific heat C by assuming spatial dimensionality $d = 3$:

$$C \sim T^{\frac{d}{z}} \equiv T^{\gamma} \tag{6.30}$$

and

$$\lim_{T\to 0} \frac{C}{T} \sim |x - x_c|^{\nu(d-z)} \equiv |x - x_c|^{-\alpha} \tag{6.31}$$

Spatial dimensionality d is assumed to be three for $Ce_{1-x}La_xCu_2Ge_2$ and it follows that

$$\gamma = \begin{cases} 0.9459 \pm 0.0605 & \mathbf{q} = \mathbf{Q} \\ 0.8364 \pm 0.0583 & \mathbf{q} = 0 \end{cases} \tag{6.32}$$

Definition		$\mathbf{q}=\mathbf{Q}$	$\mathbf{q}=\mathbf{0}$
$\lim_{T\to 0}\frac{C}{T}\sim\lvert x-x_c\rvert^{\nu(d-z)}\equiv\lvert x-x_c\rvert^{-\alpha}$	α	0.0859 ± 0.1015	0.2934 ± 0.1249
$M=(x_c-x)^{\beta}$	β	0.4910 ± 0.0300	0.4910 ± 0.0300
$\frac{1}{\chi^{-1}-Q}\sim B^{\frac{1}{\delta}-1}$	δ	3.7994 ± 0.0722	3.8358 ± 0.1280
$C\sim T^{\frac{d}{z}}\equiv T^{\theta}$	θ	0.9459 ± 0.0605	0.8364 ± 0.0583
Temporal Dimensionality	z	3.1717 ± 0.2029	3.5867 ± 0.2497
$\frac{1}{\chi^{-1}-\chi_0^{-1}}=B^{\frac{1}{\delta}-1}\Phi\left(\frac{T}{B^{\kappa}}\right)$	κ	0.8501	0.9522

Table 6.1: *Critical exponents obtained from NRG + DMFT self-consistent calculation. Here we assume that the spatial dimensionality $d=3$ and the critical exponent ν of the correlation length is $\frac{1}{2}$. χ_0^{-1} is zero for staggered susceptibility and a finite number for uniform susceptibility.*

$$\alpha=\begin{cases}0.0859\pm 0.1015 & \mathbf{q}=\mathbf{Q}\\ 0.2934\pm 0.1249 & \mathbf{q}=0.\end{cases} \tag{6.33}$$

Is choosing $d=3$ compatible with mean field theory for $Ce_{1-x}La_xCu_2Ge_2$? The lattice structure of $CeCu_2Ge_2$ is a tetragonal body centered cube with lattice constant $a=b=4.17$ and $c=10.21$ [101]. For each unit cell, cerium atoms sit at the center and eight corners and are connected by gemanium and copper atoms. Assuming that all Ce couple to Ge and Cu with equal strength, the coordination number is 16 which is sufficiently good for applying DMFT. Furthermore, high dimensionality and anisotropy of the lattice also strengthen the validity of mean field framework.

In $YbRh_2Si_2$, experimental measurement shows that $\alpha=0.3\pm 0.01$ [26] and scaling analysis suggests $\gamma=0.75$ [24, 26]. Exponents are summarized in Table (6.1).

In this theoretical work on the dilute itinerant antiferromagnet, we successfully recover the phase diagram and we see the crossover from a lattice system to a single impurity system. It is interesting to see that susceptibilities follow the local scaling and critical exponents are in good agreement with those obtained from experiments despite it is a mean field calculation and Fermi quasiparticle is well defined. One possible explaination is that order parameter fluctuations grow along the direction of time but not in space [40, 102]. We hope this theoretical work will provide more insights into the metallic antiferromagnetic quantum critical point and make some contributions (if any) in building the theory for quantum critical materials.

Bibliography

[1] H. Hodovanets, S. L. Bud'ko, W. E. Straszheim, V. Taufour, E. D. Mun, H. Kim, R. Flint, and P. C. Canfield. Remarkably robust and correlated coherence and antiferromagnetism in $(Ce_{1-x}La_x)Cu_2Ge_2$. *Phys. Rev. Lett.*, 114:236601, Jun 2015. doi: 10.1103/PhysRevLett.114.236601. URL `http://link.aps.org/doi/10.1103/PhysRevLett.114.236601`.
(Cited on pages ix, xii, 2, 3, 7, 11, 23, 43, 45, and 49.)

[2] W. A. C. Erkelens, L. P. Regnault, J. Rossat-Mignod, J. E. Moore, R. A. Butera, and L. J. de Jongh. Observation of crossover to 4-dimensional critical behaviour. *EPL (Europhysics Letters)*, 1(1):37, 1986. URL `http://stacks.iop.org/0295-5075/1/i=1/a=006`.
(Cited on pages ix and 7.)

[3] Martin Klanjšek. Viewpoint: A critical test of quantum criticality. *Physics*, 7(0):74, 2014. URL `https://physics.aps.org/articles/v7/74`.
(Cited on pages ix and 8.)

[4] A. W. Kinross, M. Fu, T. J. Munsie, H. A. Dabkowska, G. M. Luke, Subir Sachdev, and T. Imai. Evolution of quantum fluctuations near the quantum critical point of the transverse field ising chain system $CoNb_2O_6$. *Phys. Rev. X*, 4:031008, Jul 2014. doi: 10.1103/PhysRevX.4.031008. URL `http://link.aps.org/doi/10.1103/PhysRevX.4.031008`.
(Cited on pages ix, 9, and 10.)

[5] Y. Kurosaki, Y. Shimizu, K. Miyagawa, K. Kanoda, and G. Saito. Mott transition from a spin liquid to a Fermi liquid in the spin-frustrated organic conductor κ-$(ET)_2cu_2(CN)_3$. *Phys. Rev. Lett.*, 95:177001, Oct 2005. doi: 10.1103/PhysRevLett.95.177001. URL `http://link.aps.org/doi/10.1103/PhysRevLett.95.177001`.
(Cited on pages ix, 9, and 10.)

[6] Hilbert von Löhneysen. Non-Fermi-liquid behaviour in the heavy-fermion system $CeCu_{6-x}Au_x$. *Journal of Physics: Condensed Matter*, 8(48):9689, 1996. URL `http://stacks.iop.org/0953-8984/8/i=48/a=003`.
(Cited on pages ix and 11.)

[7] H. von Löhneysen, A. Neubert, T. Pietrus, A. Schröder, O. Stockert, U. Tutsch, M. Loewenhaupt, A. Rosch, and P. Wölfle. Magnetic order and transport in the heavy-fermion system CeCuAu. *The European Physical Journal B - Condensed Matter and Complex Systems*, 5(3):447–455, 1998. ISSN 1434-6036. doi: 10.1007/s100510050465. URL `http://dx.doi.org/10.1007/s100510050465`.
(Cited on pages ix and 11.)

[8] P. Coleman. Heavy fermions: electrons at the edge of magnetism. Handbook of Magnetism and Advanced Magnetic Materials. Edited by Helmut Kronmuller and Stuart Parkin. Vol 1:

Fundamentals and Theory. John Wiley and Sons, 95-148 (2007)., 2006.
(Cited on pages x and 13.)

[9] S. Doniach. The Kondo lattice and weak antiferromagnetism. *Physica B+C*, 91:231 – 234, 1977. ISSN 0378-4363. doi: http://dx.doi.org/10.1016/0378-4363(77)90190-5. URL http://www.sciencedirect.com/science/article/pii/0378436377901905.
(Cited on pages x and 13.)

[10] R. Bulla, T. A. Costi, and D. Vollhardt. Finite-temperature numerical renormalization group study of the Mott transition. *Phys. Rev. B*, 64:045103, Jun 2001. doi: 10.1103/PhysRevB.64.045103. URL http://link.aps.org/doi/10.1103/PhysRevB.64.045103.
(Cited on pages x and 17.)

[11] Daniel Antonio. *High Pressure X-Ray Absorption Spectroscopy Studies of Heavy-Fermion Cerium and Uranium Compounds*. PhD thesis, University of Nevada, Las Vegas, 2015.
(Cited on pages x, 23, and 24.)

[12] M. Y. Kimura, K. Fukushima, H. Takeuchi, S. Ikeda, H. Sugiyama, Y. Tomida, G. Kuwahara, H. Fujiwara, T. Kiss, A. Yasui, I. Kawasaki, H. Yamagami, Y. Saitoh, T. Muro, T. Ebihara, and A. Sekiyama. Soft x-ray angle-resolved and resonance photoemission study of $CeCu_2Ge_2$ and $LaCu_2Ge_2$. *Journal of Physics: Conference Series*, 592(1):012003, 2015. URL http://stacks.iop.org/1742-6596/592/i=1/a=012003.
(Cited on pages x, 23, and 24.)

[13] H. O. Frota and L. N. Oliveira. Photoemission spectroscopy for the spin-degenerate Anderson model. *Phys. Rev. B*, 33:7871–7874, Jun 1986. doi: 10.1103/PhysRevB.33.7871. URL http://link.aps.org/doi/10.1103/PhysRevB.33.7871.
(Cited on pages x and 37.)

[14] Wanda C. Oliveira and Luiz N. Oliveira. Generalized numerical renormalization-group method to calculate the thermodynamical properties of impurities in metals. *Phys. Rev. B*, 49:11986–11994, May 1994. doi: 10.1103/PhysRevB.49.11986. URL http://link.aps.org/doi/10.1103/PhysRevB.49.11986.
(Cited on pages x, 36, and 37.)

[15] Ralf Bulla, Theo A. Costi, and Thomas Pruschke. Numerical renormalization group method for quantum impurity systems. *Rev. Mod. Phys.*, 80:395–450, Apr 2008. doi: 10.1103/RevModPhys.80.395. URL http://link.aps.org/doi/10.1103/RevModPhys.80.395.
(Cited on pages x, 36, 37, 38, and 39.)

[16] N. E. Hussey, K. Takenaka, and H. Takagi. Universality of the Mott–Ioffe–Regel limit in metals. *Philosophical Magazine*, 84(27):2847–2864, sep 2004. doi: 10.1080/14786430410001716944. URL http://dx.doi.org/10.1080/14786430410001716944.
(Cited on pages xii, 44, and 48.)

[17] S. Kimura, J. Sichelschmidt, J. Ferstl, C. Krellner, C. Geibel, and F. Steglich. Optical observation of non-Fermi-liquid behavior in the heavy fermion state of $YbRh_2Si_2$. *Phys. Rev. B*, 74:132408, Oct 2006. doi: 10.1103/PhysRevB.74.132408. URL http://link.aps.org/doi/10.1103/PhysRevB.74.132408.
(Cited on pages xv, 64, 65, and 80.)

[18] A. Schroder, G. Aeppli, R. Coldea, M. Adams, O. Stockert, H.v. Löhneysen, R. Ramazashvili, and P. Coleman. Onset of antiferromagnetism in heavy-fermion metals. *Nature*, 407(21):351–355, 2000. URL `http://dx.doi.org/10.1038/35030039`.
(Cited on pages xvi, 1, 43, 81, 88, 90, and 92.)

[19] Subir Sachdev. Where is the quantum critical point in the cuprate superconductors? *physica status solidi (b)*, 247(3):537–543, mar 2010. doi: 10.1002/pssb.200983037. URL `http://dx.doi.org/10.1002/pssb.200983037`.
(Cited on page 1.)

[20] Subir Sachdev and Bernhard Keimer. Quantum criticality. *Phys. Today*, 64(2):29, 2011. doi: 10.1063/1.3554314. URL `http://dx.doi.org/10.1063/1.3554314`.
(Cited on page 1.)

[21] John A. Hertz. Quantum critical phenomena. *Phys. Rev. B*, 14:1165–1184, Aug 1976. doi: 10.1103/PhysRevB.14.1165. URL `http://link.aps.org/doi/10.1103/PhysRevB.14.1165`.
(Cited on pages 1, 7, and 43.)

[22] A. J. Millis. Effect of a nonzero temperature on quantum critical points in itinerant fermion systems. *Phys. Rev. B*, 48:7183–7196, Sep 1993. doi: 10.1103/PhysRevB.48.7183. URL `http://link.aps.org/doi/10.1103/PhysRevB.48.7183`.
(Not cited.)

[23] Tôru Moriya and Tetsuya Takimoto. Anomalous properties around magnetic instability in heavy electron systems. *Journal of the Physical Society of Japan*, 64(3):960–969, 1995. doi: 10.1143/JPSJ.64.960. URL `http://dx.doi.org/10.1143/JPSJ.64.960`.
(Cited on pages 1, 7, and 43.)

[24] Elihu Abrahams and Peter Wolfle. Critical quasiparticle theory applied to heavy fermion metals near an antiferromagnetic quantum phase transition. *Proceedings of the National Academy of Sciences*, 109(9):3238–3242, 2012. doi: 10.1073/pnas.1200346109.
(Cited on pages 1, 89, and 93.)

[25] D. R. Grempel and Qimiao Si. Locally critical point in an anisotropic Kondo lattice. *Phys. Rev. Lett.*, 91:026401, Jul 2003. doi: 10.1103/PhysRevLett.91.026401. URL `http://link.aps.org/doi/10.1103/PhysRevLett.91.026401`.
(Cited on pages 1 and 88.)

[26] Y. Tokiwa, T. Radu, C. Geibel, F. Steglich, and P. Gegenwart. Divergence of the magnetic Grüneisen ratio at the field-induced quantum critical point in $YbRh_2Si_2$. *Phys. Rev. Lett.*, 102:066401, Feb 2009. doi: 10.1103/PhysRevLett.102.066401. URL `http://link.aps.org/doi/10.1103/PhysRevLett.102.066401`.
(Cited on pages 89 and 93.)

[27] R. Küchler, N. Oeschler, P. Gegenwart, T. Cichorek, K. Neumaier, O. Tegus, C. Geibel, J. A. Mydosh, F. Steglich, L. Zhu, and Q. Si. Divergence of the Grüneisen ratio at quantum critical points in heavy fermion metals. *Phys. Rev. Lett.*, 91:066405, Aug 2003. doi: 10.1103/PhysRevLett.91.066405. URL `http://link.aps.org/doi/10.1103/PhysRevLett.91.066405`.
(Cited on pages 1 and 89.)

[28] J. H. Shim, K. Haule, and G. Kotliar. Modeling the localized-to-itinerant electronic transition in the heavy fermion system $CeCuIn_5$. *Science*, 318(5856):1615–1617, 2007. ISSN 0036-8075. doi: 10.1126/science.1149064. URL http://science.sciencemag.org/content/318/5856/1615.
(Cited on page 2.)

[29] Haiyan Lu and Li Huang. Pressure-driven $4f$ localized-itinerant transition in heavy fermion compound $CeIn_3$: A first-principles many-body perspective, 2016.
(Cited on page 2.)

[30] W.J. de Haas, J. de Boer, and G.J. van den Berg. The electrical resistance of gold, copper and lead at low temperatures. *Physica*, 1(7):1115 – 1124, 1934. ISSN 0031-8914. doi: http://dx.doi.org/10.1016/S0031-8914(34)80310-2. URL http://www.sciencedirect.com/science/article/pii/S0031891434803102.
(Cited on page 4.)

[31] Jun Kondo. Resistance minimum in dilute magnetic alloys. *Progress of Theoretical Physics*, 32 (1):37–49, 1964. doi: 10.1143/PTP.32.37. URL http://ptp.oxfordjournals.org/content/32/1/37.abstract.
(Cited on page 4.)

[32] Yosuke Nagaoka. Self-consistent treatment of Kondo's effect in dilute alloys. *Phys. Rev.*, 138: A1112–A1120, May 1965. doi: 10.1103/PhysRev.138.A1112. URL http://link.aps.org/doi/10.1103/PhysRev.138.A1112.
(Cited on page 4.)

[33] P W Anderson. A poor man's derivation of scaling laws for the Kondo problem. *Journal of Physics C: Solid State Physics*, 3(12):2436, 1970. URL http://stacks.iop.org/0022-3719/3/i=12/a=008.
(Cited on pages 4 and 12.)

[34] B.B. Triplett and N.E. Phillips. Low-temperature heat capacity of $Ni_{0.62}Rh_{0.38}$. *Physics Letters A*, 37(5):443 – 444, 1971. ISSN 0375-9601. doi: http://dx.doi.org/10.1016/0375-9601(71)90626-8. URL http://www.sciencedirect.com/science/article/pii/0375960171906268.
(Cited on page 4.)

[35] J. R. Schrieffer and P. A. Wolff. Relation between the Anderson and Kondo hamiltonians. *Phys. Rev.*, 149:491–492, Sep 1966. doi: 10.1103/PhysRev.149.491. URL http://link.aps.org/doi/10.1103/PhysRev.149.491.
(Cited on page 4.)

[36] H. R. Krishna-murthy, J. W. Wilkins, and K. G. Wilson. Renormalization-group approach to the Anderson model of dilute magnetic alloys. i. static properties for the symmetric case. *Phys. Rev. B*, 21:1003–1043, Feb 1980. doi: 10.1103/PhysRevB.21.1003. URL http://link.aps.org/doi/10.1103/PhysRevB.21.1003.
(Cited on pages 5, 16, 31, 35, and 37.)

[37] H. R. Krishna-murthy, J. W. Wilkins, and K. G. Wilson. Renormalization-group approach to the Anderson model of dilute magnetic alloys. ii. static properties for the asymmetric case. *Phys. Rev. B*, 21:1044–1083, Feb 1980. doi: 10.1103/PhysRevB.21.1044. URL http://link.aps.org/

doi/10.1103/PhysRevB.21.1044.
(Cited on pages 5 and 16.)

[38] Subir Sachdev. *Quantum Phase Transitions*. Cambridge University Press, second edition, 2011. ISBN 9780511973765. URL http://dx.doi.org/10.1017/CBO9780511973765. Cambridge Books Online.
(Cited on pages 7 and 9.)

[39] C. L. Huang, D. Fuchs, M. Wissinger, R. Schneider, M. C. Ling, M. S. Scheurer, J. Schmalian, and H. v. Löhneysen. Anomalous quantum criticality in an itinerant ferromagnet. *Nature Communications*, 6:8188, Sep 2015. doi: 10.1038/ncomms9188. URL http://dx.doi.org/10.1038/ncomms9188.
(Cited on page 7.)

[40] Piers Coleman and Andrew J Schofield. Quantum criticality. *Nature*, 433:226–229, Jan 2005. doi: 10.1038/nature03279. URL http://dx.doi.org/10.1038/nature03279.
(Cited on page 93.)

[41] Frank Steglich. Twenty-five years of heavy-fermion superconductivity. *Physica B: Condensed Matter*, 359-361:326–332, apr 2005. doi: 10.1016/j.physb.2005.01.054. URL http://dx.doi.org/10.1016/j.physb.2005.01.054.
(Not cited.)

[42] M. Matusiak, E. M. Tunnicliffe, J. R. Cooper, Y. Matsushita, and I. R. Fisher. Evidence for a charge Kondo effect in $Pb_{1-x}Tl_xTe$ from measurements of thermoelectric power. *Phys. Rev. B*, 80:220403, Dec 2009. doi: 10.1103/PhysRevB.80.220403. URL http://link.aps.org/doi/10.1103/PhysRevB.80.220403.
(Not cited.)

[43] Louis Taillefer. Superconductivity and quantum criticality. *La Physique Au Canada*, 67(2):109–112, 2011.
(Not cited.)

[44] Thomas Vojta. Quantum phase transitions and novel phases in condensed matter, 2015.
(Not cited.)

[45] Hilbert v. Löhneysen, Achim Rosch, Matthias Vojta, and Peter Wölfle. Fermi-liquid instabilities at magnetic quantum phase transitions. *Rev. Mod. Phys.*, 79:1015–1075, Aug 2007. doi: 10.1103/RevModPhys.79.1015. URL http://link.aps.org/doi/10.1103/RevModPhys.79.1015.
(Cited on page 7.)

[46] Charles Kittel. *Introduction to Solid State Physics*. John Wiley & Sons, Inc., New York, 8th edition, 2005.
(Cited on pages 11 and 12.)

[47] Oliver Bodensiek, Rok Žitko, Matthias Vojta, Mark Jarrell, and Thomas Pruschke. Unconventional superconductivity from local spin fluctuations in the Kondo lattice. *Phys. Rev. Lett.*, 110:146406, Apr 2013. doi: 10.1103/PhysRevLett.110.146406. URL http://link.aps.org/doi/10.1103/PhysRevLett.110.146406.
(Cited on page 12.)

[48] Oliver Bodensiek. *Superconductivity and Antiferromagnetism in the Kondo-Lattice Model*. PhD thesis, Georg-August-Universität Göttingen, 2013.
(Cited on page 12.)

[49] Fumiko Yonezawa and Kazuo Morigaki. Coherent potential approximation. basic concepts and applications. *Progress of Theoretical Physics Supplement*, 53:1–76, 1973. doi: 10.1143/PTPS.53.1. URL http://ptps.oxfordjournals.org/content/53/1.abstract.
(Cited on page 14.)

[50] B. Velický. Theory of electronic transport in disordered binary alloys: Coherent-potential approximation. *Phys. Rev.*, 184:614–627, Aug 1969. doi: 10.1103/PhysRev.184.614. URL http://link.aps.org/doi/10.1103/PhysRev.184.614.
(Cited on page 14.)

[51] Subhradip Ghosh, P. L. Leath, and Morrel H. Cohen. Phonons in random alloys: The itinerant coherent-potential approximation. *Phys. Rev. B*, 66:214206, Dec 2002. doi: 10.1103/PhysRevB.66.214206. URL http://link.aps.org/doi/10.1103/PhysRevB.66.214206.
(Cited on page 15.)

[52] D. W. Taylor. Vibrational properties of imperfect crystals with large defect concentrations. *Phys. Rev.*, 156:1017–1029, Apr 1967. doi: 10.1103/PhysRev.156.1017. URL http://link.aps.org/doi/10.1103/PhysRev.156.1017.
(Cited on page 15.)

[53] D. B. Balagurov, G. C. La Rocca, and V. M. Agranovich. Coherent-potential-approximation study of excitonic absorption in orientationally disordered molecular aggregates. *Phys. Rev. B*, 68:045418, Jul 2003. doi: 10.1103/PhysRevB.68.045418. URL http://link.aps.org/doi/10.1103/PhysRevB.68.045418.
(Cited on page 15.)

[54] Hitoshi Sumi. Exciton-phonon interaction in the coherent potential approximation with application to optical spectra. *Journal of the Physical Society of Japan*, 32(3):616–628, 1972. doi: 10.1143/JPSJ.32.616. URL http://dx.doi.org/10.1143/JPSJ.32.616.
(Cited on page 15.)

[55] Masao Takahashi and Kazuhiro Mitsui. Single-site approximation for the s - f model in ferromagnetic semiconductors. *Phys. Rev. B*, 54:11298–11304, Oct 1996. doi: 10.1103/PhysRevB.54.11298. URL http://link.aps.org/doi/10.1103/PhysRevB.54.11298.
(Cited on page 15.)

[56] Sze-Shiang Feng and Mogus Mochena. Ground-state properties and the molecular theory of the Curie temperature in the coherent potential approximation of diluted magnetic semiconductors. *Journal of Physics: Condensed Matter*, 18(4):1441, 2006. URL http://stacks.iop.org/0953-8984/18/i=4/a=027.
(Cited on page 15.)

[57] Duc Anh Le. Mott transition in the half-filled Hubbard model on the honeycomb lattice within coherent potential approximation. *Modern Physics Letters B*, 27(07):1350046, 2013. doi: 10.1142/S0217984913500462. URL http://www.worldscientific.com/doi/abs/10.1142/

S0217984913500462.
(Cited on page 15.)

[58] K. Levin and H. Ehrenreich. Model Hamiltonian description of Ag-Au alloys in the coherent-potential approximation. *Phys. Rev. B*, 3:4172–4188, Jun 1971. doi: 10.1103/PhysRevB.3.4172. URL http://link.aps.org/doi/10.1103/PhysRevB.3.4172.
(Cited on page 15.)

[59] J. H. de Boer and E. J. W. Verwey. Semi-conductors with partially and with completely filled 3 d -lattice bands. *Proceedings of the Physical Society*, 49(4S):59, 1937. URL http://stacks.iop.org/0959-5309/49/i=4S/a=307.
(Cited on page 16.)

[60] N F Mott and R Peierls. Discussion of the paper by de Boer and Verwey. *Proceedings of the Physical Society*, 49(4S):72, 1937. URL http://stacks.iop.org/0959-5309/49/i=4S/a=308.
(Cited on page 16.)

[61] Martin C. Gutzwiller. Effect of correlation on the ferromagnetism of transition metals. *Phys. Rev. Lett.*, 10:159–162, Mar 1963. doi: 10.1103/PhysRevLett.10.159. URL http://link.aps.org/doi/10.1103/PhysRevLett.10.159.
(Cited on page 16.)

[62] J. Hubbard. Electron correlations in narrow energy bands. *Proceedings of the Royal Society of London A: Mathematical, Physical and Engineering Sciences*, 276(1365):238–257, 1963. ISSN 0080-4630. doi: 10.1098/rspa.1963.0204. URL http://rspa.royalsocietypublishing.org/content/276/1365/238.
(Not cited.)

[63] Junjiro Kanamori. Electron correlation and ferromagnetism of transition metals. *Progress of Theoretical Physics*, 30(3):275–289, 1963. doi: 10.1143/PTP.30.275. URL http://ptp.oxfordjournals.org/content/30/3/275.abstract.
(Cited on page 16.)

[64] Elliott H. Lieb and F. Y. Wu. Absence of Mott transition in an exact solution of the short-range, one-band model in one dimension. *Phys. Rev. Lett.*, 20:1445–1448, Jun 1968. doi: 10.1103/PhysRevLett.20.1445. URL http://link.aps.org/doi/10.1103/PhysRevLett.20.1445.
(Cited on page 16.)

[65] Kenneth G. Wilson. The renormalization group: Critical phenomena and the Kondo problem. *Rev. Mod. Phys.*, 47:773–840, Oct 1975. doi: 10.1103/RevModPhys.47.773. URL http://link.aps.org/doi/10.1103/RevModPhys.47.773.
(Cited on page 16.)

[66] J. E. Hirsch and R. M. Fye. Monte Carlo method for magnetic impurities in metals. *Phys. Rev. Lett.*, 56:2521–2524, Jun 1986. doi: 10.1103/PhysRevLett.56.2521. URL http://link.aps.org/doi/10.1103/PhysRevLett.56.2521.
(Cited on page 16.)

[67] J.W. Negele and H. Orland. *Quantum many-particle systems*. Frontiers in physics. Addison-Wesley Pub. Co., 1988. ISBN 9780201125931. URL https://books.google.de/books?id=EV8sAAAAYAAJ.
(Cited on pages 16, 20, and 28.)

[68] Antoine Georges, Gabriel Kotliar, Werner Krauth, and Marcelo J. Rozenberg. Dynamical mean-field theory of strongly correlated fermion systems and the limit of infinite dimensions. *Rev. Mod. Phys.*, 68:13–125, Jan 1996. doi: 10.1103/RevModPhys.68.13. URL http://link.aps.org/doi/10.1103/RevModPhys.68.13.
(Cited on pages 16, 17, 20, and 27.)

[69] Walter Metzner and Dieter Vollhardt. Correlated lattice fermions in $d = \infty$ dimensions. *Phys. Rev. Lett.*, 62:324–327, Jan 1989. doi: 10.1103/PhysRevLett.62.324. URL http://link.aps.org/doi/10.1103/PhysRevLett.62.324.
(Cited on pages 17, 18, and 27.)

[70] Ralf Bulla. Dynamical mean-field theory - from quantum impurity physics to lattice problems. Phil. Mag. 86, 1877 (2006), 2004.
(Cited on page 17.)

[71] Krzysztof Byczuk and Dieter Vollhardt. Correlated bosons on a lattice: Dynamical mean-field theory for Bose-Einstein condensed and normal phases. *Phys. Rev. B*, 77:235106, Jun 2008. doi: 10.1103/PhysRevB.77.235106. URL http://link.aps.org/doi/10.1103/PhysRevB.77.235106.
(Cited on page 17.)

[72] Peter Anders, Emanuel Gull, Lode Pollet, Matthias Troyer, and Philipp Werner. Dynamical mean-field theory for bosons. *New Journal of Physics*, 13(7):075013, 2011. URL http://stacks.iop.org/1367-2630/13/i=7/a=075013.
(Cited on page 17.)

[73] Krzysztof Byczuk and Dieter Vollhardt. Mixtures of correlated bosons and fermions: Dynamical mean-field theory for normal and condensed phases. Ann. Phys. (Berlin) 18, 622 (2009), 2009.
(Cited on page 17.)

[74] Dieter Vollhardt, Krzysztof Byczuk, and Marcus Kollar. *Strongly Correlated Systems: Theoretical Methods*, chapter Dynamical Mean-Field Theory, pages 203–236. Springer Berlin Heidelberg, Berlin, Heidelberg, 2012. ISBN 978-3-642-21831-6. doi: 10.1007/978-3-642-21831-6_7. URL http://dx.doi.org/10.1007/978-3-642-21831-6_7.
(Cited on page 17.)

[75] D. Vollhardt, K. Byczuk, and M. Kollar. Dynamical Mean-Field Theory, arxiv:1109.4833, 2011.
(Cited on page 18.)

[76] Dieter Vollhardt. Dynamical Mean-Field Theory (DMFT), Summer School: Bandstructure Meets Many-Body Theory, Sep 2012.
(Cited on page 18.)

[77] A. A. Abrikosov, L. P. Gorkov, and I. E. Dzyaloshinski. *Methods of Quantum Field Theory in Statistical Physics*. Dover Publicationm, INC. New York, dover edition, 1975.
(Cited on pages 19 and 27.)

[78] Kristjan Haule. Dynamical Mean-Field Theory, Lecture note, 2010.
(Cited on page 19.)

[79] Pierre Villars. Localized magnetic states in metals.
(Cited on page 23.)

[80] P. W. Anderson. Localized magnetic states in metals. *Phys. Rev.*, 124:41–53, Oct 1961. doi: 10.1103/PhysRev.124.41. URL http://link.aps.org/doi/10.1103/PhysRev.124.41.
(Cited on pages 25 and 35.)

[81] R. Bulla, A. C. Hewson, and Th. Pruschke. Numerical renormalization group calculations for the self-energy of the impurity anderson model. *Journal of Physics: Condensed Matter*, 10(37): 8365, 1998. URL http://stacks.iop.org/0953-8984/10/i=37/a=021.
(Cited on pages 26 and 32.)

[82] Rok Žitko. Adaptive logarithmic discretization for numerical renormalization group methods. *Computer Physics Communications*, 180(8):1271 – 1276, 2009. ISSN 0010-4655. doi: http://dx.doi.org/10.1016/j.cpc.2009.02.007. URL http://www.sciencedirect.com/science/article/pii/S0010465509000630.
(Cited on page 36.)

[83] Rok Žitko and Thomas Pruschke. Energy resolution and discretization artifacts in the numerical renormalization group. *Phys. Rev. B*, 79:085106, Feb 2009. doi: 10.1103/PhysRevB.79.085106. URL http://link.aps.org/doi/10.1103/PhysRevB.79.085106.
(Cited on page 36.)

[84] Robert Peters, Thomas Pruschke, and Frithjof B. Anders. Numerical renormalization group approach to Green's functions for quantum impurity models. *Phys. Rev. B*, 74:245114, Dec 2006. doi: 10.1103/PhysRevB.74.245114. URL http://link.aps.org/doi/10.1103/PhysRevB.74.245114.
(Cited on page 38.)

[85] Andreas Weichselbaum and Jan von Delft. Sum-rule conserving spectral functions from the numerical renormalization group. *Phys. Rev. Lett.*, 99:076402, Aug 2007. doi: 10.1103/PhysRevLett.99.076402. URL http://link.aps.org/doi/10.1103/PhysRevLett.99.076402.
(Cited on page 38.)

[86] P. W. Anderson. New approach to the theory of superexchange interactions. *Phys. Rev.*, 115:2–13, Jul 1959. doi: 10.1103/PhysRev.115.2. URL http://link.aps.org/doi/10.1103/PhysRev.115.2.
(Cited on page 43.)

[87] Edmund C. Stoner. Collective electron specific heat and spin paramagnetism in metals. *Proceedings of the Royal Society of London A: Mathematical, Physical and Engineering Sciences*, 154(883):656–678, 1936. ISSN 0080-4630. doi: 10.1098/rspa.1936.0075. URL http:

//rspa.royalsocietypublishing.org/content/154/883/656.
(Cited on page 43.)

[88] A. W. Overhauser. New mechanism of antiferromagnetism. *Phys. Rev. Lett.*, 3:414–416, Nov 1959. doi: 10.1103/PhysRevLett.3.414. URL http://link.aps.org/doi/10.1103/PhysRevLett.3.414.
(Cited on page 43.)

[89] Qimiao Si. Global magnetic phase diagram and local quantum criticality in heavy fermion metals. *Physica B: Condensed Matter*, 378 - 380:23 – 27, 2006. ISSN 0921-4526.
(Cited on page 43.)

[90] Qimiao Si and Frank Steglich. Heavy fermions and quantum phase transitions. *Science*, 329 (5996):1161–1166, 2010. ISSN 0036-8075. doi: 10.1126/science.1191195. URL http://science.sciencemag.org/content/329/5996/1161.
(Cited on page 43.)

[91] A.F. Ioffe and A.R. Regel. Non-crystalline, amorphous and liquid electronic semiconductors. *Prog. Semicond*, 4(237):89, 1960.
(Cited on page 44.)

[92] N.F.Mott. Conduction in non-crystalline systems ix. the minimum metallic conductivity. *Philosophical Magazine*, 26(4):1015–1026, 1972. doi: 10.1080/14786437208226973. URL http://dx.doi.org/10.1080/14786437208226973.
(Cited on page 44.)

[93] Louis-Fran çois Arsenault and A.-M. S. Tremblay. Transport functions for hypercubic and Bethe lattices. *Phys. Rev. B*, 88:205109, Nov 2013. doi: 10.1103/PhysRevB.88.205109. URL http://link.aps.org/doi/10.1103/PhysRevB.88.205109.
(Cited on page 64.)

[94] W. Götze and P. Wölfle. Homogeneous dynamical conductivity of simple metals. *Phys. Rev. B*, 6:1226–1238, Aug 1972. doi: 10.1103/PhysRevB.6.1226. URL http://link.aps.org/doi/10.1103/PhysRevB.6.1226.
(Cited on page 64.)

[95] J. W. Allen and J. C. Mikkelsen. Optical properties of CrSb, MnSb, NiSb, and NiAs. *Phys. Rev. B*, 15:2952–2960, Mar 1977. doi: 10.1103/PhysRevB.15.2952. URL http://link.aps.org/doi/10.1103/PhysRevB.15.2952.
(Cited on page 64.)

[96] M. A. Ordal, L. L. Long, R. J. Bell, S. E. Bell, R. R. Bell, R. W. Alexander, and C. A. Ward. Optical properties of the metals Al, Co, Cu, Au, Fe, Pb, Ni, Pd, Pt, Ag, Ti, and W in the infrared and far infrared. *Appl. Opt.*, 22(7):1099–1119, Apr 1983. doi: 10.1364/AO.22.001099. URL http://ao.osa.org/abstract.cfm?URI=ao-22-7-1099.
(Cited on page 64.)

[97] S. V. Dordevic, D. N. Basov, N. R. Dilley, E. D. Bauer, and M. B. Maple. Hybridization gap in heavy fermion compounds. *Phys. Rev. Lett.*, 86:684–687, Jan 2001. doi: 10.1103/PhysRevLett.

86.684. URL http://link.aps.org/doi/10.1103/PhysRevLett.86.684.
(Cited on page 65.)

[98] Herman Feshbach. Unified theory of nuclear reactions. *Annals of Physics*, 5(4):357 – 390, 1958. ISSN 0003-4916. doi: http://dx.doi.org/10.1016/0003-4916(58)90007-1. URL http://www.sciencedirect.com/science/article/pii/0003491658900071.
(Cited on page 65.)

[99] Bhuvanesh Sundar and Erich J. Müller. Proposal to directly observe the Kondo effect through enhanced photoinduced scattering of cold fermionic and bosonic atoms. *Phys. Rev. A*, 93: 023635, Feb 2016. doi: 10.1103/PhysRevA.93.023635. URL http://link.aps.org/doi/10.1103/PhysRevA.93.023635.
(Cited on page 65.)

[100] Qimiao Si. The local quantum critical point and non-Fermi liquid properties. *Journal of Physics: Condensed Matter*, 15(28):S2207, 2003. URL http://stacks.iop.org/0953-8984/15/i=28/a=353.
(Cited on page 88.)

[101] Yize Stephanie Li, Mao Zheng, Brian Mulcahy, Laura H. Greene, and James N. Eckstein. Growth and properties of heavy fermion $CeCu_2Ge_2$ and $CeFe_2Ge_2$ thin films. *Applied Physics Letters*, 99(4):042507, 2011. doi: http://dx.doi.org/10.1063/1.3610975. URL http://scitation.aip.org/content/aip/journal/apl/99/4/10.1063/1.3610975.
(Cited on page 93.)

[102] Q. Si, S. Rabello, K. Ingersent, and J. L. Smith. Locally critical quantum phase transitions in strongly correlated metals. *Nature*, 413:804–808, 2001. URL http://dx.doi.org/10.1038/35101507.
(Cited on page 93.)